PB84-229707

Seattle Distribution System
Corrosion Control Study. Volume 6
Use of a Rotating Disc Electrode to
Assess Copper Corrosion

Washington Univ., Seattle

Prepared for

Municipal Environmental Research Lab.
Cincinnati, OH

Aug 84

TECHNICAL REPORT DATA
(Please read Instructions on the reverse before completing)

1. REPORT NO. EPA-600/2-84-130	2.	3. RECIPIENT'S ACCESSION NO. PB84 229707
4. TITLE AND SUBTITLE SEATTLE DISTRIBUTION SYSTEM CORROSION CONTROL STUDY VOLUME VI - USE OF A ROTATING DISC ELECTRODE TO ASSESS COPPER CORROSION		5. REPORT DATE August 1984
		6. PERFORMING ORGANIZATION CODE
7. AUTHOR(S) Ronald D. Hilburn		8. PERFORMING ORGANIZATION REPORT NO.
9. PERFORMING ORGANIZATION NAME AND ADDRESS Department of Civil Engineering University of Washington Seattle, Washington 98195		10. PROGRAM ELEMENT NO.
		11. CONTRACT/GRANT NO. R806686010
12. SPONSORING AGENCY NAME AND ADDRESS Municipal Environmental Research Laboratory-Cinti., OH Office of Research and Development U.S. Environmental Protection Agency Cincinnati, OH 45268		13. TYPE OF REPORT AND PERIOD COVERED
		14. SPONSORING AGENCY CODE EPA/600/14

15. SUPPLEMENTARY NOTES

Project Officer: Marvin C. Gardels (513684-7236

16. ABSTRACT

The uniform corrosion of copper tubing used for transport of Tolt River water is characterized in this study as a heterogeneous rate process composed of metal oxidation and oxide film growth, interfacial chemical reactions, and mass transport in the liquid phase. Quantitative rate expressions were developed to characterize each of these rate processes. Experiments designed to measure the temperature and pH dependence of corrosion under rate control by each process were conducted using steady-state electrochemical techniques. The persistent and unexpected influence of solution transport of a reaction produce, presumed to be OH^-, complicated characterization and identification of underlying rate process. Surface pH could be characterized empirically as a function of solution temperature, pH, and diffusion layer thickness.

this empirical correlation for surface pH along with solution mass transport models developed for turbulent and laminar pipe flow were combined to form a steady-state pipe flow model for uniform copper corrosion. Predictions made using the model under stagnant and low flow rate conditions show a stable and low corrosion rate of 0.2 mils per year (MPY) in water of pH > 6.0. At lower pH, predicted rates are substantially increased as the pH is reduced and temperature is increased. At high flow rates, tremendous acceleration of corrosion rate occurs, which again increases with increasing temperature and decreasing pH. Only at pH > 8.0 are the dramatic pH and temperature effects dissipated so that the rate is stabilized at a minium value of approximately 0.2 MPY.

Steady-state electrochemical techniques gave rapid, reliable, and reproducible corrosion rate measurements and provided the versatility necessary to characterize quantitatively a heterogeneous rate process like aqueous copper corrosion.

17. KEY WORDS AND DOCUMENT ANALYSIS

a. DESCRIPTORS	b. IDENTIFIERS/OPEN ENDED TERMS	c. COSATI Field/Group

18. DISTRIBUTION STATEMENT Release to Public	19. SECURITY CLASS (This Report) Unclassified	21. NO. OF PAGES 205
	20. SECURITY CLASS (This page)	22. PRICE

EPA-600/2-84-130
August 1984

SEATTLE DISTRIBUTION SYSTEM CORROSION CONTROL STUDY

Volume VI. Use of a Rotating Disc Electrode to Assess Copper Corrosion

by

Ronald D. Hilburn
Department of Civil Engineering
University of Washington
Seattle, Washington 98195

Cooperative Agreement No. R 806686 010

Project Officer

Marvin C. Gardels
Drinking Water Research Division
Municipal Environmental Research Laboratory
Cincinnati, Ohio 45268

MUNICIPAL ENVIRONMENTAL RESEARCH LABORATORY
OFFICE OF RESEARCH AND DEVELOPMENT
U.S. ENVIRONMENTAL PROJECTION AGENCY
CINCINNATI, OHIO 45268

DISCLAIMER

Although the information described in this article has been funded wholly or in part by the United States Environmental Protection Agency through assistance agreement number R 806686 010 to Seattle Water Department, it has not been subjected to the Agency's required peer and administrative review and therefore does not necessarily reflect the views of the Agency and no official endorsement should be inferred.

FOREWORD

The U.S. Environmental Protection Agency was created because of increasing public and government concern about the dangers of pollution to the health and welfare of the American people. Noxious air, foul water, and spoiled land are tragic testimonies to the deterioration of our natural environment. The complexity of that environment and the interplay of its components require a concentrated and integrated attack on the problem.

Research and development is that necessary first step in problem solution, and it involves defining the problem, measuring its impact, and searching for solutions. The Municipal Environmental Research Laboratory develops new and improved technology and systems to prevent, treat, and manage wastewater and solid and hazardous waste pollutant discharges from municipal and community sources, to preserve and treat public drinking water supplies, and to minimize the adverse economic, social, health, and aesthetic effects of pollution. This publication is one of the products of that research and is a most vital communications link between the researcher and the user community.

This report presents the results and conclusions from studies dealing with the effects of flow, temperature, and chemical composition of Tolt River water on copper corrosion. The data support the conclusion that substantial corrosion reduction can be achieved by raising the pH to a value above 8.0.

ABSTRACT

The uniform corrosion of copper tubing used for cold water transport has been characterized as a heterogeneous rate process composed of metal oxidation and oxide film growth, interfacial chemical reactions, and mass transport in the liquid phase. Quantitative rate expressions were developed to characterize each of these rate processes. Experiments designed to measure the temperature and pH-dependence of corrosion under rate control by each process were conducted using steady-state electrochemical techniques. The persistent and unexpected influence of solution mass transport of a reaction product (presumed to be OH^-) complicated characterization and identification of underlying rate processes. Surface pH could be empirically characterized as a function of solution temperature, pH, and diffusion-layer thickness.

This empirical correlation for surface pH along with solution mass transport models developed for turbulent and laminar pipe flow were combined to form a steady-state pipe flow model for uniform copper corrosion. Predictions made using the model under stagnant and low-flowrate conditions show a stable and low corrosion rate of 0.2 mils per year in water of pH > 6.0. At lower pH, predicted rates are substantially increased as pH is reduced and temperature is increased. At high flowrates, tremendous acceleration of corrosion rate occurs which again increases with increasing temperature and decreasing pH. Only at pH > 8.0 are the dramatic pH and temperature effects dissipated so that the rate is stabilized at a minimum value of approximately 0.2 mils per year.

Steady-state electrochemical techniques have been shown to give rapid, reliable, and reproducible corrosion rate measurements and to provide the versatility necessary for quantitative characterization of a heterogeneous rate process such as aqueous copper corrosion.

This report was submited in the fulfillment of Contract No. R 806686 010 by the Seattle Water Department under the sponsorship of the U.S. Environmental Protection Agency. This report covers the period June, 1979 to March, 1983, and work was completed as of March, 1983.

CONTENTS

	Page
Foreword	iii
Abstract	iv
Figures	vi
Tables	x
Abbreviations and Symbols	xii
1. Introduction	1
2. Conclusions	5
3. Recommendations	7
4. Uniform Copper Corrosion: A Heterogeneous Rate Process	8
5. Experimental Procedures	61
6. Experimental Results and Analysis	100
7. Proposed Steady-State Pipe Flow Model for Uniform Copper Corrosion	168
References	184

FIGURES

Number		Page
1	Duplex Oxide Film Formed in Aqueous Copper Corrosion	10
2	Simplified Copper/Oxide/Water System	14
3	Chemical Reactions Involved in Aqueous Copper Corrosion	14
4	Temperature and Film Thickness Dependence of Electron Transport Mechanism	29
5	Cylindrical Coordinate System	56
6	Parabolic Velocity Distribution Characteristic of Laminar Pipe Flow	56
7	Levich Model for Turbulent Pipe Flow	47
8	Surface Roughness, Velocity, and Concentration Profiles in Turbulent Flow	53
9	Copper Corrosion Rate Versus Pipe Flow Reynolds Number from Cornet et al. (37)	55
10	Mass Transport Dependence of Copper Corrosion in Nitric Acid from Frank-Kamenetskeii et al. (38)	56
11	Mass Transport Dependence of Copper Corrosion in Neutral Solutions from Roberts and Schemilt (39)	57
12	Corrosion Rate of Copper in H_2SO_4 Versus Hydrogen Ion Concentration Under Varied Conditions of Rate Control from Zembura (40)	57
13	Metal/Solution System for Experiments Designed to be Under Kinetic Rate Control	63
14	Metal/Oxide/Solution System for Experiments Designed to Be Under Solution Transport Rate Control	64
15	Metal/Solution System for Experiments Designed to Be Under Solution Transport Rate Control	65

FIGURES - Continued

16 Polarization Curve 69

17 Diffusion Controlled Cathodic Half-Cell 70

18 Diffusion Controlled Anodic Half-Cell 71

19 Three-Point Method for Calculating Corrosion Rate Under Kinetic Rate Control 74

20 Three-Point Method for Calculating Corrosion Rate Under Transport Control by Anodic Reaction 76

21 Three-Point Method for Calculating Corrosion Rate Under Transport Control by Cathodic Reaction 79

22 Basic Electrochemical Cell for Corrosion Rate Measurements ... 80

23 Experimental Apparatus Used in this Study 81

24 Electrochemical Cell Used in this Study 82

25 Rotator for Rotating Disc Electrode 84

26 Rotating Copper Disc Electrode 84

27 Solution IR Drop 87

28 Variability in Three-Point Method 94

29 Test Tube Containing Weight Loss Coupon 97

30 Weight Loss Test Apparatus 97

31 Weight Loss Test Results 99

32 Frank-Kamenetskii Plot for Data Taken in Heterogeneous Systems 103

33 Frank-Kamenetskii Plot of Kinetic Data at 25°C 113

34 Frank-Kamenetskii Plot of Kinetic Data at 15°C 115

35 Frank-Kamenetskii Plot of Kinetic Data at 5°C 119

36 Kinetic Data of Region I at 25°C 120

37 Comparison of Region I Results with All Kinetic Data at 25°C 124

FIGURES - Continued

38 Kinetic Data of Region II at 25° C 126

39 Kinetic Data of Region III at 25° C 128

40 Kinetic Data of Region III at 15°C and 5° C 129

41 Electrode/solution Interface in Experiments Designed for Oxide Film Growth Rate Control 133

42 Frank-Kamenetskii Plot of Oxide Film Growth Data at 25°C 42

43 Frank-Kamenetskii Plot of Oxide Film Growth Data at 15°C 138

44 Frank-Kamenetskii Plot of Oxide Film Growth Data at 5°C 139

45 Oxide Film Growth Data at 25°C 141

46 Oxide Film Growth Data at 15°C 142

47 Oxide Film Growth Data at 5°C 143

48 Electrode/solution Interface in Experiments Designed for Stagnant Diffusion Rate Control 144

49 Frank-Kamenetskii Plot of Stagnant Diffusion Data at 25°C 151

50 Frank-Kamenetskii Plot of Stagnant Diffusion Data at 15°C 152

51 Frank-Kamenetskii Plot of Stagnant Diffusion Data at 5°C 153

52 Stagnant Diffusion Data at 25°C 156

53 Stagnant Diffusion Data at 15°C 157

54 Stagnant Diffusion Data at 5°C 158

55 Comparison of Corrosion Rates Measured with and Without Oxide Film at 25°C 160

56 Comparison of Corrosion Rates Measured with and Without Solution Mass Transport Effects at 25°C 161

57 Comparison of Surface pH Values Calculated from Data with Those Predicted by Empirical Expression for Surface pH at 25°C 164

58 Comparison of Surface pH Values Calculated from Data with Those Predicted by Empirical Expression for Surface pH at 15°C 165

FIGURES - Continued

59 Comparison of Surface pH Values Calculated from Data with Those Predicted by Empirical Expression for Surface pH at 5°C 166

60 Corrosion Rate Estimates for 1/2 inch Copper Tubing at Varied Flowrate and 25°C 175

61 Corrosion Rate Estimates for 1/2 inch Copper Tubing at Varied Flowrate and 15°C 176

62 Corrosion Rate Estimates for 1/2 inch Copper Tubing at Varied Flowrate and 5°C 177

63 pH Dependence of Corrosion Rates Estimated for Laminar Flow Conditions 178

64 pH Dependence of Corrosion Rates Estimated for Turbulent Flow Conditions 179

65 Comparison of Copper Corrosion Rates Predicted by Pipe Flow Model with Rates Measured by Independent Sources 183

TABLES

Number		Page
1	Summary of Interfacial Reactions and Equilibria	16
2	Summary of Rate Expressions for Interfacial Reaction Rate Control	25
3	Summary of Rate Expressions for Oxide Film Growth and Transport Rate Control	36
4	Mass Transfer to Stationary Electrodes in Quiescent Solutions	49
5	Summary of Rate Expressions for Solution Mass Transport Rate Control	60
6	Synthetic Tolt Composition	89
7	Corrosion Rate of Copper in Synthetic Tolt River Water, Electrochemical Measurements	95
8	Summary of Data Analysis Methodology	109
9	Kinetic Rate Control Data: 25°C	111
10	Kinetic Rate Control Data: 15°C	116
11	Kinetic Rate Control Data: 5°C	117
12	Region I Data: 25°C	121
13	Region II Data: 25°C	123
14	Region III Data: 25°C, 15°C, and 5°C	127
15	Oxide Film Growth Rate Control Data: 25°C	134
16	Oxide Film Growth Rate Control Data: 15°C	135
17	Oxide Film Growth Rate Control Data: 5°C	136
18	Regression Results for Oxide Film Growth Data	140

TABLES - Continued

19	Parameter Estimates Calculated for Oxide Film Growth Data ...	140
20	Stagnant Diffusion Data: 25°C	146
21	Stagnant Diffusion Data: 15°C	147
22	Stagnant Diffusion Data: 5°C	148
23	Regression Results for Stagnant Diffusion Data	149
24	Calculated Diagnostic Parameters for Diffusion Rate Control	149
25	Null Hypothesis Testing Results	154
26	Parameter Estimates Calculated for StagnantDiffusion Data ...	155
27	Pipe Flow Model Parameter Values	171
28	Data for Verification of Pipe Flow Model Regression Results	181

SYMBOLS

a	Lattice parameter (approx. 2Å for Cu_2O)
ba, bc	Anodic and cathodic Tafel slopes (mv)
c	Concentration of point defects in oxide (cm^{-3}), or of a chemical species in solution ($mole/cm^3$)
$Cu^+[]$	Copper cation vacancy within oxide (ionic vacancy defect)
Cu(M)	Metallic copper
D	Diffusion coefficient (cm^2/sec)
d	Pipe diameter (cm)
E	Electrode potential (mv vs. SCE)
E_{cor}	Corrosion potential (mv vs. SCE)
E_o	Electrostatic field strength in oxide film
e^-	Electron
e	Rough surface protrusion height (cm)
e	Elementary electronic charge (1.60219×10^{-10} conc.)
F	Faraday constant (96, 485 conc.)
h	Plank constant (6.62618×10^{-34} J-sec)
$\hbar$	Plank constant divided by 2π
$\mathring{h}$	Electron hole in oxide (electronic vacancy defect)
i	Current density ($\mu A/cm^2$)
J^i	Ionic defect particle current within oxide film
J^e	Electronic defect particle current within oxide film
K	Equilibrium constant
k_w	Ion product of water
k(E)	Potential dependent rate constant for electron transfer reaction
k_f	Rate constant for forward reaction
k_r	Rate constant for reverse reaction
k	Boltzmann constant (1.38066×10^{-23} J/°k)
L	Thickness of oxide film (Å)
L	Distance down axial length of pipe from inlet (cm)

SYMBOLS - Continued

M^x_{Cu}	Completely charged balanced copper atom within oxide
m	Effective electron mass
N	Molar flux (moles cm^2sec)
P	Partial pressure of dissolved O_2 in liquid phase
q_i	Ionic defect charge ($Z_i e$)
q_e	Electronic defect charge (e)
R	Rate of reaction, in bulk (moles/cm_3 sec), on surface (moles/cm^2 sec)
R	Molar gas constant (8.31441 J/mole °K)
r	Radial distance variable in cylindrical coordinates
R	Pipe radius (cm)
Re	Reynolds number
Sc	Schmidt number
T	Absolute temperature (°K)
t	Transport number
u	Ionic mobility in electrostatic field
v	Field velocity (cm/sec)
ψ	Zero field energy barrier within oxide (ev).
X_o	Work function at metal/oxide interface (ev)
X_L	Work function at oxide/solution interface (ev.)
X	Distance variable cartesian coordinates
Y	Axial distance variable in cylindrical coordinates
Z	Integer charge on charged defects and solution species
λ	Ionic equivalent conductance
δ_H	hydrodynamic boundary layer thickness (cm)
δ_D	Diffusion layer thickness (cm)
ν	Kinematic viscosity of solution (cm_2/sec)
ν'	Ionic defect jump frequency (sec^{-1})
μ	Viscosity (c_p)
ϕ	Electrostatic potential (v)
ϕ	Angular distance variable cylindrical coordinates
	Rotation speed of rotating disc electrode (rad./sec)

Many of the symbols used contain subscripts for descriptive purposes or to refer to location. The following descriptive subscripts are used:

i	chemical species
cor	corrosion
re	reduction
ox	oxidation

The following location subscripts are used:

S	oxide/solution interfacial region
B	bulk solution

Other symbols used are defined in the text.

ACKNOWLEDGMENTS

I wish to thank and acknowledge the efforts of my supervisory committee: Professor John F. Ferguson, Chairman; Professor Brian Mar; Associate Professor Dimitris Spyridakis; Assistant Professor Mark Benjamin; and Professor James Murray, Graduate Faculty Representative, who read and provided helpful comments on the manuscript.

Special thanks to Karen Nakhjiri for her careful assistance in performing many laboratory experiments. I gratefully acknowledge Marvin Gardels of the U.S. Environmental Protection Agency, and Carlos Herrera and Brian Hoyt of the Seattle Water Department Water Quality Lab for their continued interest and support throughout the study. Thanks also to Jane Lybecker for her help in the typing of this manuscript.

This research was partly funded by a grant from the U.S. Environmental Protection Agency and supplemented by support from the Department of Civil Engineering of the University of Washington for purchase of some needed equipment.

SECTION I

INTRODUCTION

Corrosion of materials used to transport drinking water is both a public health concern and an enormous economic problem. For decades, water utilities, homeowners, and commercial building users have observed and responded to its adverse effects. Identifying the effects more clearly has led to increased understanding of the adverse impacts and a greater appreciation of the enormity of the problem.

A recent national survey conducted for the U.S. Congress by the National Bureau of Standards (1) and Battelle Columbus Laboratories (2) attempted to quantify the total economic impact of metallic corrosion in the United States. The estimated total cost in 1975 for industrial, commercial, and public establishments was $82 billion. This figure included monies spent to replace deteriorated parts and equipment, to maintain and repair, and to control corrosion directly. In the drinking water field, costs as high as $375 million/year have been estimated (3) for replacement parts and repair of distribution systems transmitting corrosive water, with an additional cost of $27 million/year to treat water (3) for corrosion control. Current costs are likely to be even higher. Furthermore, the Seattle Water Department has estimated that repair costs for consumer plumbing systems are 10 to 20 times higher than those associated with the distribution system. Annual expenditures of 500,000 for corrosion control are estimated to reduce consumer costs by $2 million.

The drinking water cycle (which includes the raw water source, treatment processes, and water distribution system) is subject to contamination and water quality degradation in any of its phases. The impact of corrosion is especially important because it occurs in the distribution system -- the part of the cycle closest to the point of customer use. Water quality degradation

and contamination occur because of the release of metal cations and other corrosion products into the water.

Public health concerns include ingestion and bodily accumulation of metal cations from drinking water. Maximum contaminant levels for many potentially toxic chemical species have been set according to National Interim Primary Drinking Water Regulations. Dissolved lead and cadmium are the two most likely contaminants to be present in excess of standards because of aqueous corrosion (3,5,7) in plumbing systems using galvanized steel or copper tubing with lead/tin solder.

The aesthetic impacts (4,6,8) often occur because of the leaching of copper, iron, zinc, and manganese from corroding pipelines. Their effect is to render the water undesirable for drinking because of unpleasant taste and visual characteristics, and to promote staining of porcelain bathroom and kitchen fixtures. The current National Secondary Drinking Water Regulations suggest maximum concentration limits on chemical species that cause adverse aesthetic effects.

All of these effects arise from a chemical reaction between the material and a chemical component of the transported natural water. In this reaction, the structural material (a metal) is oxidized and dissolved while some component in solution is reduced. So the overall process is an oxidation-reduction reaction between the metal and a component of the solution. As the reaction proceeds, the metal is thinned, yielding a shortened useful lifetime, the length of which depends on the rate of the overall reaction. Chemical species produced by this reaction are principally dissolved metal cations, some of which have maximum concentration limits for aesthetic and health reasons. Reaction products may also promote precipitation of solids, which accumulate on the metal surface and in some cases reduce water pressure and pipeline carrying capacity (8). Corrosion control efforts are then aimed at slowing down the reaction to an acceptable rate or stopping it completely without creating further ecological or water quality problems.

Aqueous copper corrosion is a complex system of coupled chemical and physical processes that involve reactions between a solid and aqueous-phase components producing reaction products that are both solid and aqueous species. For the reaction to proceed, aqueous phase reactants must move through solution to the solid/liquid interface, which is the reaction site.

Here surface interactions occur involving adsorption of aqueous species, electron transfer, and formation of reaction products. Solid phase reaction products accumulate on the surface, and aqueous phase products are transported to bulk solution.

The overall corrosion process involves the transport of reacting species in solution, chemical reaction at the solid/solution interface, and transport of aqueous phase reaction products away from the interface to bulk solution. The rate at which each of these processes proceeds affects the overall corrosion rate.

Rigorous study of a process as complex as aqueous copper corrosion is indeed a multidisciplinary effort. Principles taken from solid-state, electrochemical, and corrosion sciences must be combined with those of water chemistry and environmental engineering to describe and understand adequately the overall process as a composite of fundamental rate processes. Though coupled together, each component rate process is influenced by a distinct set of environmental variables that affects the rate at which it proceeds. The overall corrosion rate depends at least partially on the rates of these component processes. The main thrust of this work, then, is to present an overview of copper corrosion in drinking water as a composite of several fundamental rate processes and through laboratory experiments to determine which rate processes exert the greatest rate controlling influence on the overall process. The environmental variables most important in influencing the rate-controlling processes are also evaluated.

Standard steady-state electrochemical techniques, augumented with special instrumentation necessary for measurement in natural waters of low conductivity, were used to measure corrosion rate. Measurements were made under differing conditions of rate control to evaluate the dependence of component processes on temperature, fluid motion, and chemical composition of the system.

Specifically, the goals of this study were as follows:

1. To characterize as comprehensively as possible aqueous copper corrosion as a heterogeneous rate process by bringing together principles from various disciplines to develop quantitative rate expressions for each of the component rate processes involved.

2. To demonstrate the utility of steady-state electrochemical techniques as a laboratory tool for the study of corrosion in drinking water systems.
3. To determine experimentally which rate processes are most important in controlling the overall rate of uniform copper corrosion.
4. To determine which environmental variables exert the greatest influence on the corrosion rate in natural waters of composition similar to that of the Tolt River.
5. To demonstrate the applicability of experimental results in the development of a steady-state model for copper corrosion in pipe flow.

SECTION II

CONCLUSIONS

INTRODUCTION

The results and major conclusions of the research are summarized and reviewed in this chapter in light of the objectives listed in Section I. Suggestions are presented for future studies to resolve some of the questions raised by this work.

SUMMARY

Aqueous copper corrosion has been characterized as a heterogeneous rate process composed of metal oxidation, oxide film growth, interfacial chemical reactions, and mass transport in the liquid phase. Quantitative rate expressions were developed in Section 4 to characterize each of these rate processes. The experiments conducted were designed to measure the temperature and pH dependence of corrosion under rate control by each of these processes. The persistent and unexpected influence of solution mass transport of a reaction product, presumed to be OH^-, complicated characterization and identification of underlying rate processes. It was possible to empirically characterize surface pH, pH_s, as a function of solution temperature, pH, and diffusion-layer thickness.

This empirical correlation for pH_s, along with solution mass transport models developed for turbulent and laminar pipe flow were combined to form a steady-state pipe flow model for uniform copper corrosion. Predictions made using the model under stagnant or low flowrate conditions show a stable and low (0.20 MPY) corrosion rate in water of $pH_B > 6.0$. For $pH \leq 6.0$, predicted rates are substantially increased as pH_B is reduced and temperature is increased. At high flowrates, tremendous acceleration of corrosion rate occurs, which again increases with increasing temperature and decreasing pH_B. Only above a pH_B of about 8.0 are the dramatic pH_B and temperature effects

dissipated so that the rate is stabilized at a minimum value of approximately 0.2 MPY.

CONCLUSIONS

Based on this work, the following conclusions were drawn:

1. Over the pH range 6.0 to 8.5, the rate of copper corrosion is reduced as pH is increased.
2. Over the temperature range of 5°C to 25°C, the rate of copper corrosion is reduced as temperature is reduced.
3. The presence of a Cu_2O film on the copper surface reduces the corrosion rate at all pH and temperature values studied.
4. The transport of a reaction product (presumed to be OH^-) away from the oxide/solution interface is the principal process controlling the overall corrosion rate. At low pH (6.0), rate control by mass transport is nearly complete. At higher pH values (>8.0), the influence of the underlying rate process exerts a greater influence on the overall rate.
5. In pipe flow under stagnant or low flowrate (laminar flow) conditions, the corrosion rate of copper is stabilized, for pH_B > 6.0, at a value of 0.2 MPY. Only when the pH is reduced below 6.0 do the accelerating effects of low pH and high temperature manifest themselves.
6. At high (turbulent) flowrates in pipe flow, corrosion rates are accelerated dramatically with reduced pH and increased temperature. Under these conditions, only at pH_B > 8.0 is the corrosion rate stabilized to an acceptably low value of 0.2 MPY.
7. The use of steady-state electrochemical techniques have been shown to give reliable and reproducible corrosion rate measurements even in water of low conductivity. In addition, they provide the versatility needed for experimental design of adequate sophistication to produce data that can be used in mechanism determination and model development. These qualities greatly enhance the research capabilities of the experimentor.

SECTION III

RECOMMENDATIONS

Based on the results of this study, recommendations regarding additional research are presented in the areas of aqueous corrosion science, aqueous copper corrosion, and expanded use of electrochemical techniques.

The ability to characterize complex metal/oxide/solution systems as heterogeneous rate processes seems to be an important step in determining the dependence of the corrosion rate on system variables. Bringing together appropriate multidisciplinary information to develop quantitative rate expressions for processes involved in the general corrosion of metals other than copper used in the transport of drinking water is suggested as crucial to the development of aqueous corrosion science.

Extension and refinement of the model presented for aqueous copper corrosion is also suggested. Extension to a broader range of aqueous species and concentrations to include species involved in water treatment processes such as chlorination seems advisable. Further sophistication in mathematically modeling the oxide/solution interfacial interactions controlling the solution pH just next to the interface is also in order, along with precipitation studies involving the injection of Cu^{2+} and OH^- into a volume of water of known chemical composition simulating the effect of the corrosion process in the solution adjacent to the oxide/solution interface. The effect of precipitated hydroxide and carbonate solids in altering the corrosion rate by depositing on the metal surface could then be evaluated.

We recommend that the steady-state methods used here be further applied to the study of other metal/oxide/solution systems. Testing and development is recommended for transient electrochemical techniques such as the A.C. Impedance method, which because of its possibility for instantaneous measurement can provide invaluable insight into understanding of the coupled rate processes involved in aqueous corrosion.

SECTION IV

UNIFORM COPPER CORROSION: A HETEROGENEOUS RATE PROCESS

INTRODUCTION

To quantitatively model a chemically reacting system as complex as copper corrosion in drinking water it is necessary to: 1) break down the overall system into its fundamental component processes; 2) identify, evaluate, and quantify mechanisms for each component process; and 3) combine the rate expressions derived for each component process to formulate a rate expression for the overall process. The result is an ability to show to what extent variables affecting each of the component processes influence the rate of the overall process. Of interest in this study are the effects of chemical composition of the water as well as physical variables involved in pipe flow on the overall rate of uniform copper corrosion. Component rate processes are identified for uniform copper corrosion and quantitative rate expressions are developed in this chapter. These rate expressions are then evaluated and fit to data in Section 6, and combined to form an overall system model in Section 7.

The section begins by outlining the Duplex Film theory of copper corrosion, a qualitative approach which provides a picture of the overall process along with a listing of appropriate chemical reactions. This is followed by a presentation of quantitative models of each of the individual rate processes that compose the corrosion process. Interfacial reaction kinetics is presented first, followed by oxide film growth and transport, and solution mass transport models. When these rate process models are integrated into the qualitative picture given by the Duplex Film model, the desired quantitative overview of aqueous copper corrosion is obtained.

AQUEOUS COPPER CORROSION: A QUALITATIVE OVERVIEW

In aqueous systems corrosion involves an oxidation-reduction reaction between the metal and an oxidizing agent in solution. In the oxidation half-cell the metal is oxidized from the zero to the +1, +2, or +3 oxidation state. At near neutral pH values the reduction half-cell generally involves molecular oxygen reduction from the zero to the -2 oxidation state. Reaction products often form a solid film on the metal surface separating the metal from the aqueous phase. The presence of such a film can greatly increase the complexity of the process over that of a simple chemical reaction between the metal and a component in solution. This is the case for copper corroding in aqueous media of near neutral pH.

Perhaps the most comprehensive study of copper corrosion in drinking water was done by Ives and Rawson (1, 2, 3, 4) 20 years ago. Their study involved characterization of the physical make-up of a corroding copper system as well as an outline of the chemical reactions involved. The effects of all anions usually present in natural waters were studied over a range of concentrations typical for drinking water. It was established that at pH $\geq$ 3.5 the oxidation of copper in aqueous media involved growth of an oxide film on the metal surface which substantially effects the corrosion rate. This led to formulation of the Duplex Film Model of general copper corrosion in aqueous media.

The Duplex Film Model, developed by Ives and Rawson, is principally a qualitative model containing considerable detail on the chemistry of the copper corrosion reaction. The proposed mechanism includes formation of a cuprous oxide (Cu_2O) film which is estimated to grow to a thickness of roughly 20 Å before stresses in the film cause it to break up. An outer layer of porous film composed of Cu_2O, $Cu(OH)_2$ and CuO then forms on top of the continuous layer. The Cu_2O comes from break up of the underlying film, $Cu(OH)_2$ precipitates in neutral and alkaline solution, and CuO is produced as the broken up Cu_2O equilibrates with the solution. The name Duplex Film comes from recognition of the two layers of oxide film formed. The metal/oxide/solution system represented by this model is shown in Figure 1.

The overall mechanism proposed by Ives and Rawson is essentially composed of the following reactions:

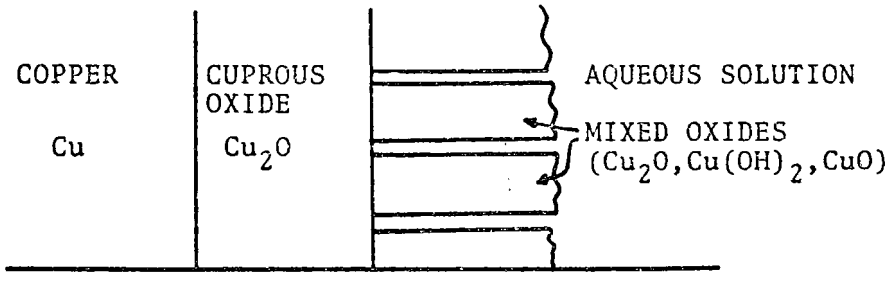

Figure 1. Metal/Oxide/Solution System for General Copper Corrosion in Aqueous Media.

a) copper dissolution
b) cuprous oxide film growth
c) cuprous oxide dissolution
d) molecular oxygen reduction

The oxidation half-cell involves several steps, not all of which are electron transfer reactions. In the first step, copper is oxidized at the metal/oxide interface forming copper cations in the film and producing electrons:

$$Cu \longrightarrow Cu^{+1} + e^- \quad \text{(Copper Dissolution)} \tag{1}$$

Cations, Cu^{+1}, created in this step are transported to the oxide/solution interface where they react with water to form new cuprous oxide.

$$Cu^{+1} + 1/2\ H_2O \longrightarrow 1/2\ Cu_2O + H^+ \quad \text{(Film Growth)} \tag{2}$$

The oxide film grows from its outer edge into solution until a steady state thickness is reached. Oxide then begins to spawl and break up into solution, and an outer porous layer of mixed oxides is formed. Cuprous oxide dissolves by reacting with hydrogen ion in solution as follows:

$$1/2\ Cu_2O + H^+ \longrightarrow Cu^{2+} + 1/2\ H_2O + e^- \quad \text{(Film Dissolution)} \tag{3}$$

Corrosion proceeds via a film growth mechanism since the underlying layer of film is being continuously regenerated and maintained at roughly a constant thickness despite dissolution and break up of its outer regions due to mechanical strains and chemical oxidation.

Molecular oxygen reduction is the principal reduction half-cell for copper corrosion at near neutral pH values. This reaction has been widely studied and comprehensive works by Hoare (5), Damjanovic (6, 7), and Yeager (8) show that the reaction proceeds through intermediate formation of hydrogen peroxide in acidic solutions.

$$O_2 + 2\ H^+ + 2\ e^- \longrightarrow H_2O_2 \tag{4}$$

$$H_2O_2 + 2\ H^+ + 2\ e^- \longrightarrow 2\ H_2O \tag{5}$$

O_2 is adsorbed from solution onto the oxide surface, followed by dissociation and acceptance of electrons forming two O^-_{ads} species for each O_2 adsorbed. O^-_{ads} sites are then protonated, forming surface bound H_2O_2. At this point the H_2O_2 may either desorb and go into solution as an aqueous species, or be reduced by further reaction with H^+ to form water. Both of these pathways have been reported, although a recent treatment by Smyrl (9) suggests that only reaction (4) is involved, and virtually all H_2O_2 enters solution as an aqueous species. There it may react with other solution components, but it no longer participates in the reduction half-cell for copper corrosion.

In alkaline solution, a slightly different reaction occurs. It has been characterized by the following stoichiometry:

$$O_2 + 2\ H_2O + 4\ e^- \longrightarrow 4\ OH^- \tag{6}$$

Here O_2 still adsorbs to the oxide surface, accepts electrons, dissociates forming two O^-_{ads} species. But due to the high pH or low H^+ availability in solution, protons are acquired from water molecules with the formation of hydroxyl ions.

Regardless of the mechanism, O_2 reduction requires acceptance of electrons donated by the oxide film. The source of available electrons are the reactions composing the oxidation half-cell. At least half of these electrons are generated at the metal/oxide interface by the copper dissolution reaction. Since molecular oxygen is reduced at the oxide/solution interface

electron transport across the film is required to keep the overall corrosion process going.

In addition to providing a physical picture of the overall corrosion process and an accounting of the principal chemical reactions involved, the Ives/Rawson study included an evaluation of the effects of several solution species common to natural waters that do not participate explicitly in the reaction mechanism of copper corrosion. The effects of chloride, sulfate, nitrate, and bicarbonate ion on corrosion rate were evaluated experimentally. While a complete explanation as to how each of these anions affects the corrosion process is lacking, they all are reported by Ives and Rawson (4) to influence the corrosion process by adsorbing at the oxide/solution interface.

Chloride ion was found to have the most significant effect on copper corrosion of all the anions evaluated. It was found to penetrate the porous oxide layer and absorb strongly at the underlying Cu_2O solution interface increasing the rates of the copper dissolution, Cu_2O film growth, and Cu_2O dissolution reactions. The effect at 100 ppm chloride was to double the corrosion rate over that measured in chloride free water. The presence of chloride was also found to initiate a change from general corrosion to localized corrosion by becoming incorporated into the Cu_2O film and altering its transport properties. Unlike chloride, the other anions tested (sulfate, nitrate, and bicarbonate) all showed minimal influence on the corrosion rate. Calcium bicarbonate was reported to induce a slight passivating effect, reducing the corrosion rate.

The Duplex Film Model gives a complex picture of a corroding copper system, that in appearance might be difficult to quantify. A physical picture of the overall system that is easier to work with quantitatively is accessible by making several reasonable assumptions:

1. The continuous film, underlying the broken up or porous outer film, is composed solely of Cu_2O and is of constant thickness.
2. The outermost, broken up and porous, film provides essentially no corrosion protection since water flows into the pores and cracks making direct contact with the underlying continuous film.
3. The pores and cracks in the outer film are large enough that diffusing species in the liquid do not have a longer diffusional path due to the presence of the outer portion of the film.

With these assumptions one can view the corrosion process in terms of the simplified model shown in Figure 2.

When each of the chemical reactions participating in the aqueous corrosion of copper is placed in its spatial context, as shown in Figure 3 below, the rate processes required for corrosion to occur become apparent:

1) Kinetics of the interfacial reactions is one process involved.
2) Transport of O_2 and H^+ through solution to react at the oxide/solution interface and of OH^-, Cu^{2+}, and other Cu^{2+} complexes away from the interface are other participating rate process.
3) The transport of copper cations and electrons across the oxide film is also a necessity for the overall reaction to continue.

Quantification of these rate processes requires knowledge of some of the properties of the oxide film separating the metal and the aqueous phase. Cuprous oxide exists in nonstoichiometric ionic crystalline form as a p-type semiconductor. It is nonstoichiometric in that it contains a deficit of both copper cations and electrons. These deficits are manifested as point defects in the oxide. So cuprous oxide contains ionic defects (cation vacancies) and electronic defects (electron holes). These defects are involved in the interfacial reactions as well as in the transport of charge across the film.

Interfacial reactions involving transfer of copper cations are more precisely written as either producing or destroying cation vacancies. When copper dissolves, the oxidation reaction occurring at the metal/oxide interface involves a singly charged copper cation leaving the metal lattice and entering the oxide. This reaction is normally written as:

$$Cu \longrightarrow Cu^{+1} + e^- \qquad (1)$$

The creation of a copper cation shown by equation (1) above can also be written in the following form as a defect reaction in which a cation vacancy within the oxide is destroyed:

$$Cu + Cu^{+}[] \longrightarrow e^- \qquad (7)$$

Here $Cu^{+}[]$ symbolizes a singly charged copper cation vacancy within the oxide, which is written as a reactant since it is consumed in the reaction.

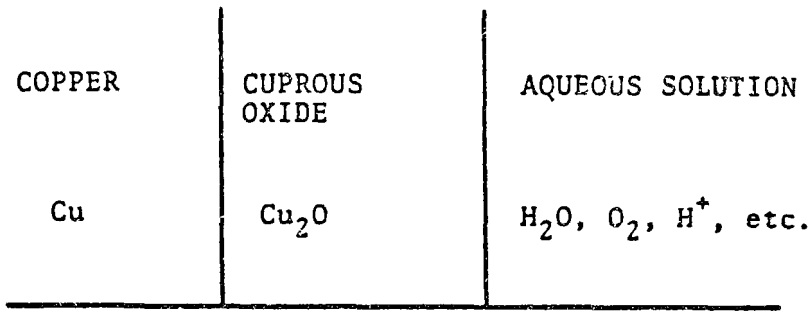

Figure 2. Simplified Copper/Oxide/Water System.

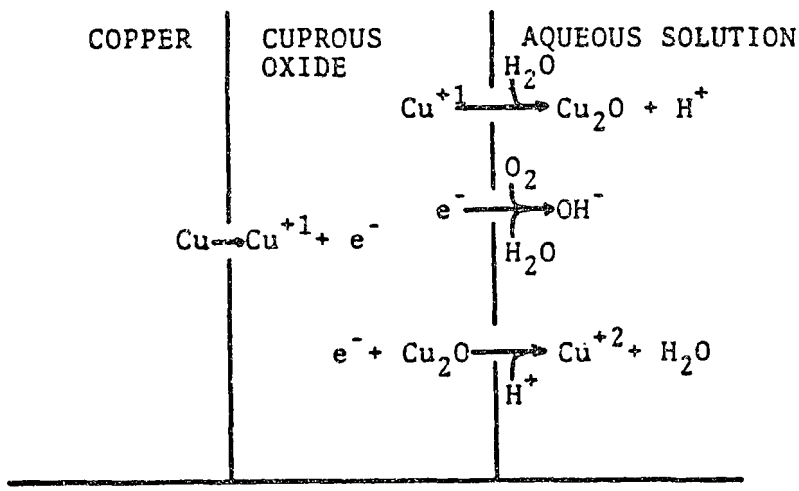

Figure 3. Chemical Reactions Involved in Aqueous Copper Corrosion.

The electron transfer in equation (7) above can be written in terms of its electronic defect:

$$Cu + Cu^{+}[] + \overset{\circ}{h} \longrightarrow 0 \qquad (8)$$

Here $\overset{\circ}{h}$ is an electron hole (electron vacancy) in the oxide. It is also written as a reactant since it is consumed in the reaction. The symbol 0 stands for a completely occupied and charge balanced lattice site within the oxide. The electron produced, as the copper cation leaves the metal lattice, enters the oxide by consuming an electron hole in the oxide. In this manner cation vacancies and electron holes are consumed at the metal/oxide interface.

The three remaining reactions occur at the oxide/solution interface. Each ones involves creation of cation vacancies or electron holes, or both within the oxide. The general picture then is that point defects, cation vacancies and electron holes, are created at the oxide/solution interface by reactions between the oxide and solution, and are consumed at the metal/oxide interface by the reaction occurring there. A net migration of cation vacancies and electron holes from the oxide/solution interface to the metal/ oxide interface is then required for the overall corrosion process to continue. The details of defect formation and consumption will be discussed in the upcoming section on interfacial reaction kinetics, while the mode of defect transport across the film will be discussed in the section on oxide film growth and transport.

INTERFACIAL REACTION KINETICS

Three of the four principal reactions involved in the corrosion process could limit its overall rate. In this section rate expressions are developed that show how the chemical composition of the solution affects the corrosion rate when controlled by the kinetics of a particular reaction. A summary of the reactions and equilibrium expressions necessary for development of appropriate rate expressions is provided in Table 1. Rate control by one particular reaction occurs when the velocity at which it proceeds is so much slower than other rate processes that they are virtually at equilibrium. Since detailed mechanisms for each of these reactions have not been developed, it is not possible to derive rate expressions in as rigorous a manner as one would like. Rather, a more simplistic approach is taken here which

Table 1

Summary of Interfacial Reactions and Equilibria

I. Metal/Oxide Interface:

a

$$Cu \longrightarrow Cu^{+1} + e^- \text{ (metal dissolution)}$$

$$Cu + Cu^+ + \dot{h} \longrightarrow 0 \text{ (defect form)}$$

$$K_1 = \frac{1}{[Cu^+\square][\dot{h}]}$$

II. Oxide/Solution Interface:

a

$$Cu^{+1} + \frac{1}{2}H_2O \rightleftharpoons \frac{1}{2}Cu_2O + H^+ \text{ (film growth)}$$

$$M^x_{Cu} + \frac{1}{2}H_2O \rightleftharpoons Cu_2O + Cu^+[\,] + H^+$$

$$K_2 = [Cu^+\square][H^+]$$

b

$$\frac{1}{2}Cu_2O + H^+ \rightleftharpoons Cu^{2+} + \frac{1}{2}H_2O + e^- \text{ (film dissolution)}$$

$$\frac{1}{2}Cu_2O + \dot{h} + H^+ \rightleftharpoons Cu^+[\,] + Cu^{2+} + \frac{1}{2}H_2O$$

$$K_3 = \frac{[Cu^+\square][Cu^{2+}]}{[\dot{h}][H^+]}$$

c

$$\frac{1}{2}O_2 + H^+ + e^- \rightleftharpoons \frac{1}{2}H_2O_2 \quad (O_2 \text{ Reduction})$$

$$\frac{1}{2}O_2 + H^+ \rightleftharpoons \frac{1}{2}H_2O_2 + \dot{h} \quad pH < 7.0$$

$$K_4 = \frac{[H_2O_2]^{1/2}[\dot{h}]}{P^{1/2}[H^+]}$$

d

$$\frac{1}{4}O_2 + \frac{1}{2}H_2O + e^- \rightleftharpoons OH^- \quad (O_2 \text{ Reduction})$$

$$\frac{1}{2}O_2 + \frac{1}{2}H_2O \rightleftharpoons OH^- + \dot{h} \quad pH \geq 7.0$$

$$K_5 = \frac{[\dot{h}]k_w}{P^{1/4}[H^+]}$$

Notation:

M^x_{Cu} = copper atom filling a lattice site within the oxide, Cu_2O.

$\dot{h}$ = an electron vacancy (hole) in the oxide.

$Cu^+\square$ = a cation vacancy in the oxide

P = partial pressure of oxygen in liquid phase

Assumptions: $[M^x_{Cu}] = 1.0$, $[H_2O] = 1.0$, and $[Cu_2O] = 1.0$.

sometimes assumes that a reaction occurs in one step when in fact it may occur in several. With this in mind, rate expressions are derived for three of the four principal reactions.

Rate Control by Metal Dissolution

The metal dissolution reaction involves metal atoms leaving the metallic solid to fill cation and electron vacancies in the cuprous oxide. It occurs at the metal/oxide interface and can be written as follows:

$$Cu(m) \longrightarrow Cu^{+1} + e^{-} \qquad (1)$$

or in defect form as:

$$Cu(m) + Cu^{+}[] + \overset{\circ}{h} \longrightarrow 0 \qquad (8)$$

The corrosion rate is the rate at which copper metal dissolves:

$$R = -\frac{d[Cu(m)]}{dt} = k_f(E)[Cu^{+}[]]_{m/o}\,[\overset{\circ}{h}]_{m/o} \qquad (9)$$

The metallic copper activity is presumed to be one in this derivation and cation vacancies and electron hole concentrations are presumed to be small enough that their concentrations approximately equal their activities. The corrosion rate then depends on the magnitude of the rate constant, $k_f(E)$, which is potential dependent as well as the metal/oxide interfacial concentration of cation vacancies and electron holes. Imposing the condition of virtual equilibrium of other rate processes allows development of a rate expression which connects the corrosion rate with the chemical composition of the solution. Virtual equilibrum of all reactions occurring at the oxide/solution interface fixes the concentration of cation vacancies $[Cu^{+}[]]$ at the oxide surface. Chemical equilibrium at the oxide/solution interface requires that reactions IIa, IIb, and IIc of Table 1 be at equilibrium when the solution pH is less than 7.0, and that reactions IIa, IIb, and IId be at equilibrium when the solution pH is greater than 7.0. Expressions for interfacial equilibrium are derived as follows:

a) at pH $\leq$ 7.0:

$$M^x_{Cu} + 1/2\ H_2O \longrightarrow 1/2\ Cu_2O + Cu^+[] + H^+ \quad \text{(film growth)}$$

$$1/2\ O_2 + H^+ \longrightarrow 1/2\ H_2O_2 + \overset{\circ}{h} \quad \text{(oxygen reduction)}$$

$$1/2\ Cu_2O + H^+ + \overset{\circ}{h} \longrightarrow Cu^+[] + Cu^{2+} + 1/2\ H_2O \quad \text{(film dissolution)}$$

$$M^x_{Cu} + 1/2\ O_2 + H^+ \longrightarrow 2Cu^+[] + 1/2\ H_2O_2 + Cu^{2+}$$

$$K_I = \frac{[Cu^+[]]^2\ [H_2O_2]^{1/2}\ [Cu^{2+}]}{p^{1/2}\ [H^+]} = K_2 \cdot K_3 \cdot K_4$$

$$[Cu^+[]] = \left[\frac{K_I p^{1/2}}{[H_2O_2]^{1/2}[Cu^{2+}]}\right]^{1/2} [H^+]^{1/2} \qquad (10)$$

b) at pH $\geq$ 7.0:

$$M^x_{Cu} + 1/2\ H_2O \longrightarrow 1/2\ Cu_2O + Cu^+[] + H^+$$

$$1/4\ O_2 + 1/2\ H_2O \longrightarrow OH^- + \overset{\circ}{h}$$

$$1/2\ Cu_2O + H^+ + \overset{\circ}{h} \longrightarrow Cu^+[] + Cu^{2+} + 1/2\ H_2O$$

$$M^x_{Cu} + 1/2\ H_2O + 1/4\ O_2 \longrightarrow 2Cu^+[] + OH^- + Cu^{2+}$$

$$K_{II} = \frac{[Cu^+[]]^2\ [OH^-]\ [Cu^{2+}]}{p^{1/4}} = K_2 \cdot K_3 \cdot K_4$$

$$[Cu^+[]] = \left[\frac{K_{II} p^{1/4}}{[Cu^{2+}][OH^-]}\right]^{1/2} = \left[\frac{K_{II} p^{1/4}}{[Cu^{2+}]\ K_w}\right]^{1/2} [H^+]^{1/2} \qquad (11)$$

The equilibrium expressions derived in (10) and (11) above establish the necessary link between cation vacancy concentration at the oxide/solution interface and certain chemical components of the solution. They show explicitly, that the interfacial concentration of cation vacancies depends upon the partial pressure of dissolved oxygen, the concentration of cupric ion in solution, and the hydrogen ion concentration as well as a temperature dependence imbedded in the equilibrium constants.

At this point it is necessary to establish a relationship between the cation vacancy concentration at the metal/oxide interface, which is directly proportional to the rate of copper dissolution, and the cation vacancy concentration at the oxide/solution interface, which is in equilibrium with several chemical species in solution. For rate control by interfacial reaction kinetics, transport of cation vacancies and electron holes across the oxide film must occur at a much more rapid rate than the reaction controlling the overall rate. This situation is likely to occur during the initial stages of formation of the film, that is, when the metal surface is covered with oxide but the film is of insufficient thickness to allow a concentration gradient of cation vacancies to build up. Under these conditions:

$$[Cu^{+}[]]_{m/0} = [Cu^{+}[]]_{0/s} \tag{12}$$

When the oxide film grows to a greater thickness a gradient of cation vacancies across the film is established even at virtual transport equilibrium due to the presence of an electrostatic field within the oxide film. Under these conditions:

$$[Cu^{+}[]]_{m/0} = \alpha\, [Cu^{+}[]]_{0/s} \tag{13}$$

where α is a constant, with a value less than 1.0, that depends on the magnitude of the electric field in the oxide. When the absolute value of the charge on copper cation vacancies is given as ze, Fromhold (10) has shown that:

$$\alpha = e^{-(zeLE/kT)} \tag{14}$$

Thus, at a given temperature, T, film thickness, L, and electrostatic field strength, E, the ratio of cation vacancy concentrations at the two interfaces is fixed. As variations in the solution composition occur, which cause changes in cation vacancy concentration at the oxide/solution interface, the

cation vacancy concentration at the metal/oxide interface must adjust to maintain α. As it changes the rate of copper dissolution changes proportionately. This sequence of events is expressed in the following functional form:

a) at pH < 7.0:

$$R = k(E) \left[\frac{K_I P^{1/2}}{[H_2O_2]^{1/2} \, [Cu^{2+}]} \right]^{1/2} [H^+]^{1/2} \tag{15}$$

and b) at pH $\geq$ 7.0:

$$R = k(E) \left[\frac{K_{II} P^{1/4}}{[Cu^{2+}] \, K_w} \right]^{1/2} [H^+]^{1/2} \tag{16}$$

Equations (15) and (16) are derived for the initial film growth situation, where $\alpha = 1.0$. Analogous expressions, for conditions in which a fully developed oxide film is present, can be derived by multiplying the right hand side of equations (15) and (16) by α. These expressions can be simplified into a form quite suitable for comparison with measured data. Equation (15) can be rewritten as a function of solution pH as follows:

$$\log_{10} R = \log_{10} a_1 - 0.5 \text{ pH} \tag{17}$$

where: $$a_1 = k(E) \left[\frac{K_I P^{1/2}}{[H_2O_2]^{1/2} \, [Cu^{2+}]} \right]^{1/2}$$

Note that all temperature dependence is consolidated into the a_1 term and that $[Cu^{2+}]$ and $[H_2O_2]$ are assumed constant with respect to solution pH, which is at best an approximation. Equation (16) can be rewritten in a similar fashion (for pH $\geq$ 7.0):

$$\log_{10} R = \log_{10} a_2 - 0.5 \text{ pH} \tag{18}$$

$$a_2 = k(E)\left[\frac{K_{II}P^{1/4}}{[Cu^{2+}]K_w}\right]^{1/2}$$

Again all temperature dependence resides in the a_2 term. The slope of log R with respect to pH should be independent of temperature at pH < 7.0 and pH $\geq$ 7.0. The corrosion rate under conditions of rate control by copper dissolution is therefore shown to depend upon cupric ion concentration in solution, oxygen partial pressure, solution pH, and temperature.

Rate Control by Cu_2O Formation

The Cu_2O formation reaction involves a copper atom within the oxide, M^x_{Cu}, reacting with water to form more oxide and produce cation vacancies in the film. It occurs at the oxide/solution interface and can be written as follows:

$$M^x_{Cu} + 1/2\ H_2O \longrightarrow 1/2\ Cu_2O + Cu^+[] + H^+ \tag{19}$$

When this reaction controls the rate of the overall corrosion process the following rate expression pertains:

$$R = -\frac{d[M^x_{Cu}]}{dt} = k_f\ [M^x_{Cu}][H_2O]^{1/2} - k_r\ [Cu_2O]^{1/2}[Cu^+[]][H^+] \tag{20}$$

When the activities of M^x_{Cu}, H_2O, and Cu_2O are presumed to be unity the rate expression becomes:

$$R = k_f - k_r[Cu^+[]]\ [H^+] \tag{21}$$

Note that this rate expression presumes the reaction to occur as a one step process, which is at best an approximation. The cation vacancy concentration at the oxide/solution interface is fixed by the virtual equilibrium of other reactions occurring there. Separate rate expressions are necessary to describe the corrosion rate at pH values below and above 7.0. At pH $\leq$ 7.0 the concentration of cation vacancies at the oxide/solution interface is derived as follows:

$$1/2\ Cu_2O + \overset{\circ}{h} + H^+ \longrightarrow Cu^+[\,] + Cu^{2+} + 1/2\ H_2O \qquad k_3$$

$$1/2\ O_2 + H^+ \longrightarrow 1/2\ H_2O_2 + \overset{\circ}{h} \qquad k_4$$

$$1/2\ Cu_2O + 1/2\ O_2 + 2H^+ \longrightarrow Cu^+[\,] + Cu^{2+} + 1/2H_2O_2 + 1/2H_2O \qquad K_{III} = k_3 \cdot k_4$$

$$K_{III} = \frac{[Cu^+[\,]]\ [Cu^{2+}]\ [H_2O_2]^{1/2}}{p^{1/2}\ [H^+]^2}$$

therefore: $$[Cu^+[\,]] = \left(\frac{p^{1/2}\ K_{III}}{[Cu^{2+}]\ [H_2O_2]^{1/2}}\right) [H^+]^2 \qquad (pH \leq 7.0) \qquad (22)$$

Solving equations (21) and (22) simultaneously produces the following rate expression:

$$R = k_f - k_r \left[\frac{p^{1/2} K_{III}}{[Cu^{2+}][H_2O_2]^{1/2}}\right] [H^+]^3 \qquad (23)$$

This relationship can be rewritten in a general form suitable for comparison with measured data when $[Cu^{2+}]$ and $[H_2O_2]$ are presumed not a function of pH:

$$R = a - b\ 10^{-3pH} \qquad (24)$$

Here both a and b are temperature dependent.

At pH $\geq$ 7.0 the concentration of cation vacancies at the oxide/solution interface is derived as follows:

$$1/2\ Cu_2O + \overset{\circ}{h} + H^+ \longrightarrow Cu^+[\,] + Cu^{2+} + 1/2\ H_2O \qquad k_3$$

$$1/4\ O_2 + 1/2\ H_2O \longrightarrow OH^- + \overset{\circ}{h} \qquad k_5$$

$$1/2\ Cu_2O + H^+ + 1/4\ O_2 \longrightarrow Cu^+[\,] + Cu^{2+} + OH^- \qquad K_{IV} = k_3 \cdot k_5$$

$$K_{IV} = \frac{[Cu^+[\,]][Cu^{2+}][OH^-]}{[H^+]\ p^{1/4}}$$

$$\text{therefore: } [Cu^{+}[]] = \frac{P^{1/4}K_{IV}[H^{+}]}{[Cu^{2+}][OH^{-}]} = \frac{P^{1/4}K_{IV}[H^{+}]^{2}}{[Cu^{2+}]K_{w}} \quad (pH > 7.0) \tag{25}$$

Solving equations (21) and (25) simultaneously produces the following rate expression appropriate at pH $\geq$ 7.0:

$$R = k_{f} - k_{r}\left[\frac{K_{IV}P^{1/4}}{[Cu^{2+}]K_{w}}\right][H^{+}]^{3} \tag{26}$$

When rewritten in a general form suitable for comparison with data the following relationship is obtained:

$$R = a - b_{1}\ 10^{-3pH} \tag{27}$$

where both a and b_1 are temperature dependent. Here a has the same value below and above pH = 7.0, while b takes on different values in the two pH ranges. The general form of the rate expression for rate control by Cu_2O formation is thus established as a function of cupric ion concentration, oxygen partial pressure, solution pH, and temperature.

Rate Control by O_2 Reduction

The molecular oxygen reduction reaction involves the reaction of aqueous dissolved oxygen at the oxide/solution interface. O_2 adsorbs and accepts electrons (produces electron holes) at the oxide surface providing the reduction half-cell for the overall redox process. This reaction occurs by a sequence of steps which are different at pH values below seven than for pH values above seven.

At pH < 7.0, O_2 is reduced through intermediate formation of H_2O_2. There are differing opinions as to whether the reaction steps at H_2O_2 or proceeds Beyond to H_2O formation. Both reaction possibilities will be presented, with reduction to H_2O_2 presumed to be the favored pathway. The overall reaction can be written in two steps as follows:

$$O_2 + 2H^+ \longrightarrow 2\overset{\circ}{h} + H_2O_2 \qquad \text{(i)}$$

$$H_2O_2 + 2H^+ \longrightarrow 2\overset{\circ}{h} + H_2O \qquad \text{(ii)}$$

$$\overline{O_2 + 4H^+ \longrightarrow 4\overset{\circ}{h} + H_2O}$$

Vetter (11) has reported a composite of experimental evidence from many investigators for O_2 reduction on metal surfaces in acidic solutions and has presented the following rate expression:

$$R = k(E)\ P \tag{28}$$

This expression apparently holds no matter whether the reduction goes just to H_2O_2 or all the way to H_2O. On oxide covered surfaces the reduction rate is reported by Yeager (8) to be slower than on metal surfaces with intermediate formation of H_2O_2 also being the predominant pathway.

When the solution pH is equal to or greater than 7.0 the mechanism is slightly different. The reaction is irreversible and has the following stoichiometry:

$$O_2 + 2H_2O \longrightarrow 4\overset{\circ}{h} + 4OH^-$$

Vetter (11) has proposed the following rate expression for O_2 reduction on metal surfaces which is in accord with the mechanism proposed by Yeager (8) for oxide covered surfaces:

$$R = k_f(E)\ P\ [H^+] \tag{29}$$

It is interesting to note that only above pH = 7.0 does the reaction rate become pH dependent.

Rate expressions have been presented for conditions of rate control by O_2 reduction at pH values below and above 7.0. Unlike rate control by other reactions, there is no dependence on defect concentrations within the oxide; in fact, only the potential drop across the Helmholtz layer at the oxide/solution interface, pH, and P affect the corrosion rate under these conditions.

Mechanisms and rate expressions have been presented here for the principal reactions involved in the corrosion process. By looking at the rate expression one can identify the variables that affect the corrosion rate when

rate limited by a particular reaction. In this way the effect of solution composition on the overall rate becomes apparent provided the Ives/Rawson mechanism is qualitatively accurate in describing the corroding system.

Table 2 contains a summary of appropriate rate expressions.

OXIDE FILM GROWTH AND TRANSPORT

Transport of charge across a continuous oxide film growing on a corroding copper surface is one of the fundamental rate processes composing the corrosion process. As such, it could limit the rate of the overall process. In this section rate expressions are developed that show how the chemical composition of the solution affects the corrosion rate when controlled by oxide film growth and transport. Initially, physical and chemical properties of the oxide that affect the rate and mechanism of charge transport are discussed. This is followed by an explanation of how solid state transport models are put together using the coupled currents approach. The electron tunneling model is then presented to show explicitly the effect of solution composition on the rate of charge transport, as well as the overall corrosion rate when rate limited by oxide film growth and transport.

The rate and mechanism of charge transport through a continuous oxide film depends on several physical properties of the film. First of all, film structure is important, that is, whether the oxide has an amorphous or crystalline form under the environmental conditions present. Crystalline solids tend to have spatially uniform transport rates, while rates in an amorphous solid are spatially irregular containing preferential diffusion paths. Near room temperature cuprous oxide has a crystalline structure that is a body centered cubic lattice. Consequently a film growth and charge transport model is developed for oxide films that are both continuous and crystalline in structure.

The rate and mechanism of charge transport across the film are affected by temperature, film thickness, nature of defect species being transported, and nature of the electrostatic field developed within the film. For oxides like cuprous oxide which grow by transport of charged vacancy defects a variety of growth mechanisms are available and a growing film may switch from one mechanism to another depending principally on film thickness, but also on temperature. For a given mechanism the rate at which charged defects are

Table 2

Summary of Rate Expressions for Interfacial Reaction Rate Control

I. Rate Control By Metal Dissolution

$$R = a[H^+]^{1/2}$$

$$\text{where: } a = \begin{cases} k(E)\left[\dfrac{K_I P^{1/2}}{[H_2O_2]^{1/2}\,[Cu^{2+}]}\right]^{1/2} & @\ pH < 7.0 \\ k(E)\left[\dfrac{K_{II} P^{1/4}}{[Cu^{2+}]\,K_w}\right]^{1/2} & @\ pH \geq 7.0 \end{cases}$$

II. Rate Control by Oxide Formation

$$R = a - b[H^+]^3$$

where: $a = k_f$ @ all pH

$$\text{and } b = \begin{cases} k_r\left[\dfrac{K_{III} P^{1/2}}{[Cu^{2+}][H_2O_2]^{1/2}}\right] & @\ pH < 7.0 \\ k_r\left[\dfrac{K_{IV} P^{1/4}}{[Cu^{2+}]K_w}\right] & @\ pH \geq 7.0 \end{cases}$$

III. Rate Control by O_2 Reduction

$R = a$ @ $pH < 7.0$

$R = a[H^+]$ @ $pH \geq 7.0$

where: $a = k_f(E)P$

transported across the film depends in some way on the magnitude of the electrostatic field. Some mechanisms are more rate sensitive to field strength and temperature than others.

Charge transport is presented here from the point of view of the coupled currents approach, a conceptual framework developed by Fromhold (10) in his treatise entitled "Theory of Metal Oxidation" to codify and provide a unified basis for the variety of oxide film growth models that developed independently during the years 1940 to 1975. Most of these models were developed for a specific set of growth conditions, so no general overview of metal oxidation and film growth existed. It took Fromhold's insight to characterize with such clarity and rigor the common threads running through the different models.

For oxides growing by transport of charged elecronic and ionic defects different mechanisms are generally used to transport each type of defect. Each type of defect then has its own flux across the film called a particle current. Overall charge transport and oxide film growth rate depend on the coupling of the electronic defect particle current with the ionic defect paticle current. The magnitude of the electrostatic field within the oxide and steady state film thickness adjust to balance the two defect particle currents within the oxide. This is the coupled currents approach. Transport models based on this approach are composed of:

a. ionic defect transport rate expression
b. electronic defect transport rate expression
c. expression for electrostatic field in oxide

When one defect particle current is sufficiently larger than the other, at steady-state film thickness and electric field strength, the overall transport or film growth rate may be completely controlled by the smaller particle current, but the magnitude of electrostatic potential developed depends on the faster defect particle. This is the case for the electron tunneling model presented next. At early stages of film growth, ionic defect transport limits film growth, but for film thicknesses over 20 Å to 30 Å, electronic defect transport begins to limit overall rate of film growth (10).

Electron Tunneling Model

The electron tunneling model was developed by Fromhold and Cook (12) by bringing together the pioneering work of Mott (13) and Cabrera and Mott (14) on low temperature growth kinetics of thin oxide films with later quantitative developments by Simmons (15) on electron tunneling through potential barriers. The result is a quantitative model which predicts the rate of growth and steady-state transport rate of charge through the very thin oxide films growing on metal surfaces at temperatures near 25°C. The electronic defect transport mechanisms for this model involves quantum mechanical tunneling of electrons from the metal through the potential barrier of the oxide film to ultimately fill vacant energy levels in molecular oxygen adsorbed at the oxide/solution interface. It is a mechanism that is appropriate only at low temperature and for very thin films. As temperature and film thickness are increased the likelihood of other electron transport mechanisms, such as thermal emissions of electrons or electron holes over the potential barrier in the oxide is increased. Figure 4 shows how the film growth mechanism is affected by film thickness, temperature, and metal-oxide work function. The $Cu-Cu_2O$ work function has the value X_0 = 1.024 ev at 300°K (12) so the limiting thickness for electron tunneling is about 39 Å for a Cu_2O film. Above this thickness, thermal emission of electrons or holes should predominate as the electronic defect transport mechanism.

The electron tunneling particle current is presented by Fromhold to be:

$$J^e = (8\pi^2\hbar L)^{-1}[(2X_0 + eE_0L)\exp\left[\frac{-2m^{1/2}}{\hbar}(2X_0 + eE_0L)^{1/2}\right] -$$

$$(2X_L - eE_0L)\exp\left[\frac{-2m^{1/2}}{\hbar}(2X_L - eE_0L)^{1/2}\right] \qquad (30)$$

The rate of electronic tunneling across the film is seen to depend upon the film thickness, L, electric field strength, E_0, metal-oxide work function, X_0, oxide-oxygen work function, X_L, and effective electron mass, m, and h which is Plank's constant ($\hbar$) divided by 2π. For the electron tunneling mechanism to be complete, relationships for the ionic defect particle current and the electrostatic field strength must also be presented.

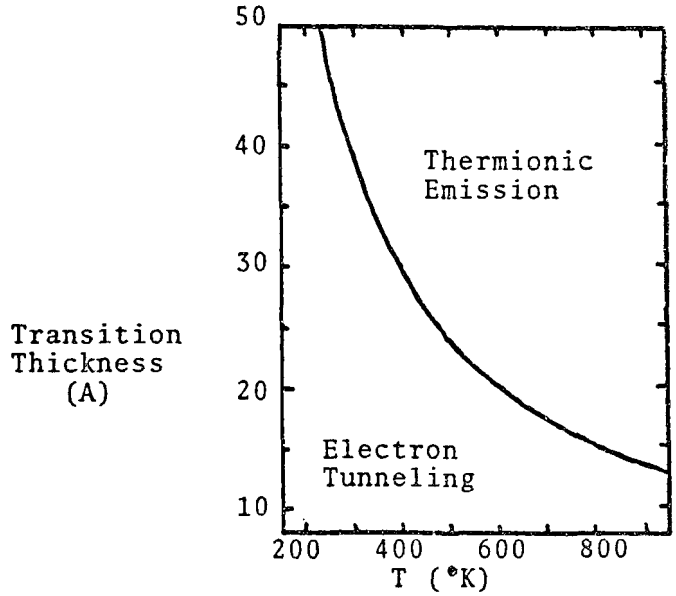

Figure 4. Temperature and Film Thickness Dependence of Electron Transport Mechanism.

Ionic defect transport through the Cu_2O film is by diffusion due to a concentration gradient of cation vacancies across the film and a large presumably homogeneous electric field within the oxide. The cation vacancy diffusion particle current as developed by Frombold for steady-state conditions is as follows:

$$J^i = 4a\nu \exp(-W/kT)\sinh(Z_i eE_0 a/kT)\left[\frac{C_i(L) - C_i(0)\exp(Z_i eE_0 L/kT)}{1 - \exp(Z_i eE_0 L/kT)}\right] \qquad (31)$$

Here a is the lattice parameter which equals approximately 2Å for Cu_2O. ν is the jump frequency (sec^{-1}) for ionic defects attempting to exceed a zero field energy barrier of height, W in ev. kT represents the thermal energy of ionic defects in ev. $Z_i e$ is the charge per cation vacancy. E_0 is the electrostatic field strength (V/cm) in the oxide. $C_i(L)$ is the concentration of ionic defects at the oxide-solution interface (no. of defects/cm^3) while

$C_i(0)$ is the concentration of ionic defects in the oxide near the metal/oxide interface (no. of defects/cm^3). L is the thickness of the film in Å.

When the two defect particle currents are subjected to the coupled currents condition, a relationship for the electric field strength, E_o, can be developed. The coupled currents condition is:

$$q_i J^i + q_e J^e = 0 \tag{32}$$

Where q_i is the charge on each ionic defect, $Z_i e$, and q_e is the charge on each electronic defect, e. By substituting the relationships for each particle current into equation (32) one may in principle solve for E_o. For this model and others analytically solving for E_o is not possible so the model is evaluated under special limiting conditions. There are two limiting conditions amenable to solution for the electron tunneling model. The first condition arises when the film is just thick enough for rate control by defect transport. This is called the early growth stage, and for the electron tunneling model the growth rate is limited during this stage by ionic defect diffusion and the electric field strength is dictated by the virtual equilibrium of electronic defects. The early growth stage model can be represented as follows:

$$J^i = 4a\nu \exp(-w/kT) \sinh(Z_i e E_o\, a/kT) \left[\frac{C_i(L) - C_i(0) \exp(Z_i e E_o L/kT)}{1 - \exp(Z_i e E_o L/kT)} \right] \tag{31}$$

$$E_o = -(X_o - X_L)/Le \tag{33}$$

Equation (31) can be simplified by noting that for L = 5Å, T = 298°K, and $E_o = 10^5$ v/cm the value of the exponential term is much smaller than one:

$$\exp(Z_i e E_o L/kT) \cong 10^{-8}$$

so the term: $$\frac{C_i(L) - C_i(0) \exp(Z_i e\, E_o L/kT)}{1 - \exp(Z_i e\, E_o\, L/kT)} \cong C_i(L)$$

Substituting this back into equation (31) above yields the following expression for the ionic defect particle current:

$$J^i = 4\ a\nu \exp(-w/kT)\ \sinh(Z_i e E_o\ a/kT)\ C_i(L) \tag{34}$$

Since the field strength, E_o, is not affected by defect concentrations the only place solution composition can affect the rate of early stage growth is through the oxide/solution interfacial concentration of cation vacancies, $C_i(L)$. For virtual equilibrium of interfacial reactions at the oxide/solution interface two relationships derived earlier in evaluating interfacial reaction kinetic rate control are appropriate. At pH < 7.0, recognizing that $[Cu^{+}[]]_{\text{oxide surface}} = C_i(L)$, the interfacial cation vacancy concentration is related to species concentrations in solution by the following relationship.

$$C_i(L) = \left[\frac{K_I\ P_2^{1/2}}{[H_2O_2]^{1/2}[Cu^{2+}]}\right]^{1/2} [H^+]^{1/2} \tag{10}$$

or:

$$C_i(L) = \left[\frac{K_I\ P^{1/2}}{[H_2O_2]^{1/2}[Cu^{2+}]}\right]^{1/2} 10^{-0.5\ pH} \tag{35}$$

At pH < 7.0, a similar relationship exists. It was derived earlier to be:

$$C_i(L) = \left[\frac{K_{II}P^{1/4}}{[Cu^{2+}]K_w}\right]^{1/2} [H^+]^{1/2} \tag{11}$$

or:

$$C_i(L) = \left[\frac{K_{II}P^{1/4}}{[Cu^{2+}]K_w}\right]^{1/2} 10^{-0.5\ pH} \tag{36}$$

So the relationship between pH, P, $[Cu^{+2}]$, and J^i is explicitly shown for pH < 7 as well as for pH $\geq$ 7 for early stage growth. The pH dependence of the rate of film growth can be summarized as follows:

a) At pH < 7.0: $J = d\ 10^{-0.5\ pH}$ (37)

where $d = 4\ a\nu \exp(-w/kT)\sinh(Z_i e_o Ea/kT)\ \left[\frac{K_I P^{1/2}}{[H_2O_2]^{1/2}[Cu^{2+}]}\right]^{1/2}$

and: $\log J = \log d - 0.5\ pH$ (38)

b) at pH > 7.0: $J = d\ 10^{-0.5\ pH}$ (39)

where: $d = 4a\ \exp(-w/kT)\sinh(Z_i eE_o a/kT) \left[\frac{K_{II} P^{1/4}}{[Cu^{2+}]\ K_w}\right]^{1/2}$

and: $\log J = \log d - 0.5\ pH$ (40)

The temperature dependence is contained in the values of the constant b for both equations. Log J versus pH then plots as a straight line with a slope of -0.5.

When the oxide film gets thicker, approximately 20 to 30Å, the electron tunnel particle current becomes rate limiting with the field strength determined by the virtual ionic defect equilibrium. When this situation arises the transport rate is:

$$J = (8\pi^2 \hbar L^2)^{-1}[(2X_o + eE_oL)\ \exp[-2m^{1/2}\hbar^{-1}L(2X_o + E_oeL)^{1/2}] -$$

$$(2X_L - eE_oL)\ \exp[-2m^{1/2}\hbar^{-1}L(2X_L - eE_oL)^{1/2}]] \quad (30)$$

with: $$E_o = \frac{kT}{Z_i\ e\ L} \ln\left[\frac{C_i(L)}{C_i(0)}\right] \quad (41)$$

Here the electric field strength, E_o, is dependent upon the cation vacancy concentration at the oxide/solution interface, but is the only term in the transport rate expression with such a defect concentration dependence. E_o is therefore the only term that responds to solution composition through $C_i(L)$. The relationships, equations (35) and (36), shown before which connect $C_i(L)$ with solution pH, P, and $[Cu^{+2}]$ still apply under later growth stage conditions.

Equation (30) can be simplified by evaluating the magnitude of the two exponential terms for T = 298°K, L = 30 Å, and $E_o = 10^5$ v/cm. The first term inside the brackets of equation (30) is found to be much larger than the second:

$$\frac{(2X_o + eE_oL)\ \exp[-2m^{1/2}\hbar^{-1}\ L(2X_o + eE_oL)^{1/2}]}{(2X_L - eE_oL)\ \exp[-2m^{1/2}\hbar^{-1}\ L(2X_L - eE_oL)^{1/2}]} \quad 500$$

The second term may then be omitted from equation (30) as being negligible when subtracted from the first. The simplified rate expression becomes:

$$J = [8\pi^2\hbar\, L^2]^{-1}(2X_0 + eE_0L)\, \exp[-2m^{1/2}\hbar^{-1}L(2X_0 + eE_0L)^{1/2}] \qquad (42)$$

As pointed out by Gibbs (16), a further simplification of equation (42) is possible for cuprous oxide films in aqueous electrolytes, provided the potential drop across the film is small. When the potential drop across the film is on the order of tens of millivolts, the electron tunneling rate expression has been reduced by Simmons (17) to the following ohmic form:

$$J = bV \qquad (43)$$

where: $$V = E_0L = \frac{kT}{Z_i e} \ln \left[\frac{C_i(L)}{C_i(0)}\right] \qquad (44)$$

b = a positive constant (temp. independent)

Solving equations (43) and (44) simultaneously the following expression is obtained:

$$J = \left(\frac{b\ kT}{Z_i\ e}\right) \mathrm{Ln} \left[\frac{C_i(L)}{C_i(0)}\right] \qquad (45)$$

Since $C_i(L)$ is related to solution composition by equilibrium expressions derived earlier:

a) At pH < 7.0:

$$C_i(L) = \left[\frac{K_I P^{1/2}}{[H_2O_2]^{1/2}\ [Cu^{2+}]}\right]^{1/2} 10^{-0.5\ pH} \qquad (35)$$

and b) At pH $\geq$ 7.0:

$$C_i(L) = \left[\left(\frac{K_{II}\ P^{1/4}}{[Cu^{2+}]\ K_W}\right)\right]^{1/2} 10^{-0.5\ pH} \qquad (36)$$

Equation (45) may be rewritten as follows for pH < 7.0:

$$J = \left(\frac{b\ k\ T}{Z_i e}\right) \ln \left[\frac{\left[\frac{K_I P^{1/2}}{[H_2O_2]^{1/2}\ [Cu^{2+}]} \right]^{1/2}}{C_i(0)} \right] 10^{-0.5\ pH} \tag{46}$$

Rearranging and separating out the pH dependence the following form evolves:

$$J = kT(C_1 + C_2\ pH) \tag{47}$$

where: $$C_1 = \frac{b}{Z_i e} \ln \left[\frac{\left[\frac{K_I P^{1/2}}{[H_2O_2]^{1/2}\ [Cu^{2+}]} \right]^{1/2}}{C_i(0)} \right]$$

and $$C_2 = \frac{-1.15b}{Z_i e}$$

At pH < 7.0 tne rate is shown to be a linear function of solution pH, with the slope, kTC_2, of the J versus pH plot a linear function of temperature. The intercept, kTC_1, is a nonlinear function of temperature since both K_I and P are temperature dependent components of C_1. Its temperature dependence then should be slightly greater than linear.

For pH $\geq$ 7.0, equation (45) may be rearranged in a similar fashion with the following result:

$$J = kT(C_1 + C_2\ pH) \tag{48}$$

where: $$C_1 = \frac{b}{Z_i e} \ln \left[\frac{\left[\frac{K_{II}\ P^{1/4}}{[Cu^{2+}]\ K_w} \right]^{1/2}}{C_i(0)} \right]$$

and $$C_2 = \frac{-1.15b}{Z_i e}$$

Note that both parameters C_1 and C_2 have the same temperature dependencies as those derived earlier at pH $\leq$ 7.0, with C_2 having identically the same magnitude at pH < 7.0, that it does at pH < 7.0.

Rate expressions have been derived in this section that show explicitly the manner in which P, cupric ion concentration, hydrogen peroxide concentration, solution pH, and temperature affect the rate of copper corrosion

when under rate control by oxide film growth and transport. A summary of these relationships is provided in Table 3.

SOLUTION MASS TRANSPORT

Mass transport in aqueous solution refers to the individual movement of ions and molecules through solution due to the presence of some driving force. This driving force may be a concentration gradient in the case of diffusion, a potential gradient in the case of migration, or a component of solution velocity in the case of convection. The rate of mass transport is measured as a flux (moles/cm^2 sec) and is normally the phenomenon of interest in chemically reacting systems. This could be the flux of a reactant from bulk solution moving toward the interface or the flux of a reaction product moving away from the interface into bulk solution. In aqueous corrosion, molecular oxygen and hydrogen ion are solution species that act as reactants in the reduction half-cell, while hydroxyl ion is a product of the reduction half-cell. If the reaction rate is fast enough, the transport of molecular oxygen, hydroxyl ion, or hydrogen ion through solution may be the rate controlling step in the reduction half-cell or even the entire corrosion process. The possibility of rate control makes solution transport phenomena an important subject of consideration. In this section the basic equations of solution transport will be presented along with some development of their chemical and hydrodynamic aspects. Existing models for mass transport in pipe flow will be presented which can be used as a basis for estimating limiting fluxes of hydrogen ion, hydroxyl ion and molecular oxygen at varied temperature, pipe size, pH, and flow velocity.

Principal Transport Equations

Two principal equations (18) that characterize the mass transport of a species in solution to and from the solid/solution interface are the overall mass flux equation and the material balance equation. Each of these can be uniquely derived for a particular species in solution. The overall mass flux of species it may be represented as follows:

$$\underline{N}_i = -D_i \nabla C_i - Z_i U_i F C_i \nabla \phi + \underline{V} C_i \qquad (49)$$

Equation (49) is written here in vector form appropriate for a variety of

Table 3

Summary of Rate Expressions for Oxide Film Growth and Transport Control

I. Early Stage Film Growth (2Å < L < 15 Å)

$$R = d\,10^{-0.5\,pH}$$

where:

$$d = \begin{cases} 4\,a\sqrt{\exp(-w/kT)\sinh(Z_1 eEa/kT)}\left[\dfrac{K_I\,P^{1/2}}{[H_2O_2]^{1/2}\,[Cu^{+2}]}\right]^{1/2} & @\ pH < 7.0 \\ 4\,a\sqrt{\exp(-w/kT)\sinh(Z_1 eEa/kT)}\left[\dfrac{K_{II}\,P}{[Cu^{2+}]\,K_w}\right]^{1/2} & @\ pH > 7.0 \end{cases}$$

II. Later Stage Film Growth (15 Å < L < 39 Å)

$$R = kT(C_1 + C_2\,pH)$$

where:

$$C_1 = \begin{cases} \dfrac{b}{Z_1 e}\ln\left\{\left[\dfrac{K_I\,P}{[H_2O_2]^{1/2}\,[Cu^{2+}]}\right]^{1/2} \Big/ C_i(o)\right\} & @\ pH \le 7.0 \\ \dfrac{b}{Z_1 e}\ln\left\{\left[\dfrac{K_{II}\,P^{1/4}}{[Cu^{2+}]\,K_w}\right]^{1/2} \Big/ C_i(o)\right\} & @\ pH > 7.0 \end{cases}$$

$$C_2 = -1.15b/Z_1 e \qquad \text{(all pH)}$$

and b = a positive constant (temp. independent). See (17)

flow geometries. The mass flux, $\underline{N}_i$, of species i is the rate of movement of species i across an area perpendicular to its path (moles/sec cm^2). This rate depends on the magnitude of the concentration gradient, ∇C_i, in the direction of movement and the diffusion coefficient, D_i. They compose the diffusional component of flux. An electrostatic potential gradient, $\nabla \phi$, in the direction of movement may also contribute to the mass flux provided species i has a net charge. This effect is called the migrational component of flux. The component of fluid velocity, $\underline{V}$, directed normal to the mass flux can exert an enormous influence on the rate of mass transport. This is the convective component of mass flux. The combined effects of diffusion, migration, and convection then determine the magnitude of mass flux in any particular direction.

The second principal equation characterizing mass transport of species in solutions is the material balance (18). It can be formulated for each solution species as follows:

$$\frac{\partial C_i}{\partial t} = - \nabla \cdot \underline{N}_i + R_i \tag{50}$$

As a statement of the conservation of mass it describes the change in concentration of species i with respect to time at a fixed point in space resulting from the movement of i and chemical reactions producing or consuming i. The general approach in solving solution mass transport problems is to solve equations (49) and (50) simultaneously to get an expression for concentration as a function of time and distance from the solid/solution interface. Differentiating that expression for $C(X,t)_i$ with respect to distance, X, and evaluating the derivative at the solid/solution interface, X = 0, gives the desired flux of species i to or from the interface. To carry out the details of this operation several simplifications are commonly made. The most noteworthy efforts made along these lines are in solving the convective-diffusion problem.

The Convective Diffusion Equation

To formulate a mass transport problem in terms of convective-diffusion it is necessary to eliminate the migrational flux term from equation (49), the mass flux equation then becomes:

$$\underline{N}_i = -D_i \nabla C_i + \underline{V} C_i \tag{51}$$

This form of the mass flux equation is appropriate for situations where potential gradients do not exist within the solution and migrational effects are negligible. It may be used where migrational effects are present by replacing the ionic diffusion coefficient for species i, D_i, with an effective diffusion coefficient, D_{ef}, given by Pickett (19) to be:

$$D_{ef} = D_i \left[\frac{1}{1 - \frac{(n/S_i)}{Z_i} t_i} \right] \tag{52}$$

Here (n/S_i) is the number of electrons consumed per mole of species i reacted or produced, Z_i is the charge on species i, and t_i is the transport number of i:

$$t_i = \frac{D_i C_i Z_i^2}{\sum_{j=1}^{m} D_j C_j Z_j^2} \tag{53}$$

for a solution containing m ionic species. Equation (51) then becomes:

$$\underline{N}_i = -D_{ef_i} \nabla C_i + \underline{V} C_i \tag{54}$$

When species i reacts only at the solid/solution interface and not in the bulk solution, the bulk reaction term, R_i, in the material balance equation is zero. So the material balance can be written as:

$$\frac{\partial C_i}{\partial t} = -\nabla \cdot \underline{N}_i \tag{55}$$

Solving equations (51) and (55) simultaneously the following relationship results:

$$\frac{\partial C_i}{\partial t} = D_i \nabla^2 C_i - \underline{V} \cdot \nabla C_i \tag{56}$$

This relationship describes the concentration of species i as a function of time and location as influenced by molecular or ionic diffusion and bulk fluid motion, and is called the convective diffusion equation. Analytical

solutions to this equation for various hydrodynamic flow regimes comprise the theoretical approach to solution transport problems (21).

Most analytical solutions are to the steady-state problem where:

$$\frac{\partial C_i}{\partial t} = 0$$

Equation (56) then becomes:

$$\underline{V} \cdot \nabla C_i = D_i \nabla^2 C_i \tag{57}$$

At low concentrations, where D_i is not a function of C_i, equation (57) is analogous to the Fourier-Poisson equation for steady-state heat conduction, a problem that has been worked on for nearly one-hundred and fifty years. Analytical solutions exist for a variety of flow regimes (see Crank (20)) and many solutions to the steady-state convective diffusion equation were originally derived for heat conduction.

The principal convective diffusion problem important in corroding drinking water systems involves the transport of species in solution (hydroxyl ion, molecular oxygen, and hydrogen ion) to and from the inner wall of a circular tube under conditions of laminar and turbulent flow. Also, the transport of solution species to the surface of a rotating disc electrode is an important convective diffusion problem, since a rotating disc electrode was used in the laboratory phase of this research.

The point in solving this problem is ultimately to be able to:

a. Estimate an upper bound on corrosion rates due to solution mass transfer limitations.
b. Evaluate the effects of principal variables such as flow velocity, pipe size, and solution pH on the limiting flux.

Pipe Flow

The reynolds number, Re, is the appropriate dimensionless parameter to characterize pipe flow (22,23). Its value depends on several system properties:

$$R_e = \frac{d \langle v_y \rangle}{\nu} \tag{58}$$

where d is the inside pipe diameter (cm), $\langle v_y \rangle$ is the mean solution velocity down the axial length of the pipe (cm/sec), and ν is the kinematic viscosity of the solution (cm^2/sec). Pipe flow at Re $\leq$ 2100 is generally laminar, for 2100 $\leq$ RE $\leq$ 4000 a transition region occurs, and at Re > 4000 flow is turbulent. Due to the physical differences in the flow patterns and the differences in velocity profile, separate solutions to the convective diffusion equation exist for turbulent and laminar flow (24). Solutions under both conditions will be discussed for pipe flow.

Solutions of the steady state convective diffusion equation for pipe Flow, involves first a transformation of the vector form of the equation:

$$\underline{V} \cdot \nabla C_i = D_i \nabla^2 C_i \tag{59}$$

into cylindrical coordinates, a geometry more appropriate for pipe flow. Figure 5 shows the cylindrical coordinates r, y and ω to be the radial, longitudinal, and angular directions respectively.

Written in these coordinates there is angular symmetry, so the ω dependence drops out. Making other appropriate assumptions, the form of the steady state convective diffusion equation becomes:

$$v_y \frac{\partial C_i}{\partial y} = D_i \left[\frac{1}{r} \frac{\partial}{\partial r} \left(r \frac{\partial C_i}{\partial r} \right) + \frac{\partial^2 C_i}{\partial y^2} \right] \tag{60}$$

Determination of v_y as a function of radial distance, r, reduces the problem to only three variables C_i, r, and y. Then with appropriate boundary values for C_i, this problem can be solved for the radial component of flux, N_i, at the surface of the pipe.

Laminar Flow

Several noteworthy solutions to the steady state convective diffusion equation have been developed for laminar pipe flow. Solutions by Graetz (25), Leveque (26), and Levich (21) are presented here. All presume fully developed Poiseuille flow, which means the longitudinal component of velocity, v_y, is distributed parabolicly over the diameter as shown in the figure below.

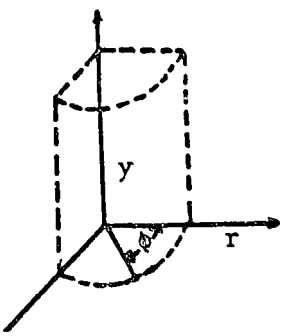

Figure 5. Cylindrical Coordinate System.

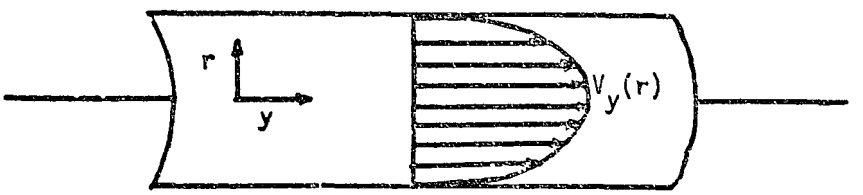

Figure 6. Parabolic Velocity Distribution Characteristic of Laminar Pipe Flow.

This velocity distribution is described as:

$$v_y = 2\langle v_y\rangle(1 - r^2/R^2) \tag{61}$$

All other components of velocity are presumed zero and the pipe surface is presumed smooth. Let's look now at specific solutions.

Graetz Solution

This solution was originally developed by Graetz (25) for heat conduction as a solution to the Fourier-Poisson problem. It was later applied to analogous mass transfer problems. Graetz used the method of separation of variables to derive the following series solution:

$$N_i = \frac{D_i(C_B - C_o)}{2R} \sum_{k=1}^{\alpha} \frac{1}{2} \lambda_k^2 M_k \exp\left(\frac{y\, D_i}{2\, \langle v_y\rangle\, R^2}\right) \tag{62}$$

The eigenvalues, λ_k, and coefficients, M_k, have numerical values worked out in the literature for k=1, ..., 10. All other parameters are physical and geometric properties of the system. With this solution one can predict the mass flux of species i to or from the inside wall of a pipe of radius, R, when i is traveling in a fluid moving down the pipe with mean velocity, $\langle v_y\rangle$. Note that the radial flux, N_i, changes with distance down the pipe from the inlet (at y=0) and the solution is applicable for all values of y.

Leveque Solution

The Leveque (26) solution treats the region where y values are small, close to the pipe inlet, and where r values are large, very near the wall of the pipe. The velocity distribution in this region was approximated by Leveque to be:

$$V_y = 4\langle V_y\rangle(1 - r/R) \tag{51}$$

Like Graetz solution, Leveque's work was initially presented as a steady-state solution of the Fourier-Poisson equation of heat conduction then later extended to the analogous mass transfer situation. The solution is as follows:

$$N_i = \frac{D_i(C_B - C_o)}{2R}[1.3566(\frac{yD_i}{2\langle v_y\rangle R^2})^{-1/3} - 1.2 - 0.296919(\frac{yD_i}{2\langle v_y\rangle R^2})^{1/3}$$

$$+ 0(\frac{yD_i}{2\langle v_y\rangle R^2})^{2/3}] \tag{64}$$

It is considered appropriate only for short distances down the tube:

$$y < \frac{0.02\langle V_y\rangle R^2}{D_i} \tag{65}$$

Note that this solution depends on the same physical and geometric parameters as the Graetz solution.

Levich Solution

This solution (21) parallels that of Leveque in that it considers only the region very close to the pipe wall where the parabolic velocity profile can be approximated as a linear function of radial distance, r. Unlike the Leveque case this solution is not derived solely for the inlet region, small values of y, so its applicability is similar to that of the Graetz solution. The solution is as follows:

$$N_i = 0.6884\ D_i(C_B - C_o)\ \left[\frac{\langle V_y\rangle}{yD_iR}\right]^{1/3} \tag{66}$$

Once again the same physical and geometric parameters determine the magnitude of the mass flux.

Each of these solutions has been corroborated experimentally and extensive literature exists on the subject. While these solutions are useful in predicting transport limited mass fluxes under conditions of laminar flow, oftentimes fluid flow in pipes is not laminar. These models alone are not adequate to predict limiting fluxes in water supply and household plumbing systems over the entire range of flow velocities normally encountered. Mass transport in turbulent pipe flow must also be considered.

Turbulent Flow

Turbulent flow is characterized by rapid and random velocity fluctuations about some time-averaged value at a fixed point in space. In addition to the longitudinal component of velocity, eddies continually form and mix the water, so transport takes place by both molecular motion (diffusion) and by turbulent mixing. The notion of a diffusion layer across which molecular or ionic species must diffuse is maintained in turbulent flow although its thickness is greatly reduced from that of laminar flow due to the turbulent mixing of forming and dissipating eddies. At present there is no single conceptual picture of turbulent flow that is universally accepted, although many models are presently being evaluated. Because of the ill-defined fluid dynamics, first principles approaches to turbulent transport have not been completely successful in explaining experimental results. Several empirical models that correlate measured mass flux with flow properties have been developed and will be presented along with solutions to the turbulent convective diffusion equation.

The convective-diffusion equation for turbulent pipe flow can be developed from its original vector form:

$$\frac{\partial C_i}{\partial t} = D_i \nabla^2 C_i - \underline{V} \cdot \nabla C_i \tag{56}$$

by replacing the concentration terms, C_i, with instantaneous turbulent concentration:

$$C_i = \bar{C}_i + C_i' \tag{67}$$

where $\bar{C}_i$ is the time averaged concentration at a point and C_i' is the instantaneous fluctuation in concentration from its time averaged value, $\bar{C}_i$. The velocity vector, $\underline{V}$, must also be replaced with an instantaneous velocity vector:

$$\underline{V} = \underline{\bar{V}} + \underline{V}' \tag{68}$$

where $\underline{\bar{V}}$ is the time averaged fluid velocity vector at a point and $\underline{V}'$ is the instantaneous fluctuation velocity vector from the time averaged value, $\underline{\bar{V}}$. When these time averaged values are inserted into equation (56) above, the turbulent convective-diffusion equation can be written as follows:

$$\frac{\partial \bar{C}_i}{\partial t} = D_{tot} \nabla^2 \bar{C}_i - \underline{\bar{v}} \cdot \nabla C_i \tag{69}$$

where D_{tot} is the total diffusion coefficient incorporating ionic (molecular) and eddy diffusion.

$$D_{tot} = D_i + D_e \tag{70}$$

Here D_e is the eddy diffusion coefficient, which may be considerably larger than the ionic (molecular) diffusion coefficient of species i.

Equation (69) above can now be converted into cylindrical coordinators:

$$\frac{\partial \bar{C}_i}{\partial t} + \bar{v}_y \frac{\partial \bar{C}_i}{\partial y} = D_{tot}\left[\frac{1}{r}\frac{\partial}{\partial r}\left(r\frac{\partial \bar{C}_i}{\partial r}\right) + \frac{\partial^2 \bar{C}_i}{\partial y^2}\right] \tag{71}$$

and solved in a manner similar to that for laminar flow, provided the time averaged longitudinal velocity component, $\bar{v}_y$, is known as a function of radial distance, r. Several empirical correlations exist relating v_y and r for pipe flow. Commonly used correlations are v_y = const., v_y is a linear function of r or v_y is a logarithmic function of r. The value of the eddy diffusivity, D_e, is also a function of r close to the wall. Empirical correlations relating D_e and r exist, so at least in principle the convective diffusion equation is solvable for turbulent pipe flow. Solutions developed by Linton and Sherwood (27) and by Van Shaw et al. (28) are representative of the deterministic approach, which is still evolving, and will be presented. Stochastic methods (29) are also being developed but will not be discussed here. Another theoretical approach developed by Levich and extended by Davies (30), that does not make use of the convective diffusion equation will also be presented.

Solutions of Linton and Sherwood and Van Shaw et al.

Van Shaw et al. solved the turbulent convective diffusion problem in a manner identical to an earlier solution by Linton and Sherwood (27). By use of cartesian coordinates (neglecting curvature) and assuming a linear velocity profile:

$$\bar{v}_y = \frac{f\langle\bar{v}_y\rangle}{2\nu} x \tag{72}$$

Here x is the distance variable normal to the, presumed flat, pipe surface and takes the place of cylindrical coordinate, r. y is still the direction down the longitudinal axis of the tube. Disregarding the dependence of D_e on x the following solution was developed:

$$\bar{N}_i = 0.276 \langle\bar{v}_y\rangle(C_B - C_o)Re^{-0.42} Sc^{-2/3} (L/d)^{-1/3} \tag{73}$$

The time averaged mass flux in the x direction, $\bar{N}_i$ is given as a function of the radial mean of the instantaneous time averaged velocities, $\langle\bar{v}_y\rangle$, the Reynolds number, Re, the Schmidt number, Sc, and the distance down the pipe from the inlet, L. The Schmidt number is defined here as:

$$Sc = \nu/D_i \tag{74}$$

where ν is the kinematic viscosity of the bulk solution (cm^2/sec) and D_i is the molecular (ionic) diffusion coefficient. This solution differs only slightly from the earlier solution of Linton and Sherwood:

$$\bar{N}_i = 0.232\langle\bar{v}_y\rangle(C_B - C_o)Re^{-0.4} Sc^{-2/3} (L/d)^{-1/3} \tag{75}$$

Data presented by Van Shaw et al. and Linton and Sherwood both show an increasing tendency for the data to follow their theoretical predictions as pipe diameters are reduced to one inch or less and at Reynolds numbers between 10^4 and 10^5.

Levich Solution

The Levich model for mass transfer in turbulent pipe flow was not derived as a solution to the turbulent convective diffusion equation. Rather, it presumes the conceptual model of the liquid/solid interface as shown in Figure 7 below. The turbulent boundary layer, of thickness y_b, is divided up into three sections with differing resistances to mass transfer. Mass transfer across each of the three sections occurs by a different mechanism and is evaluated separately. At steady state the mass flux across each of the three zones is equal. The steady-state flux is then derived by

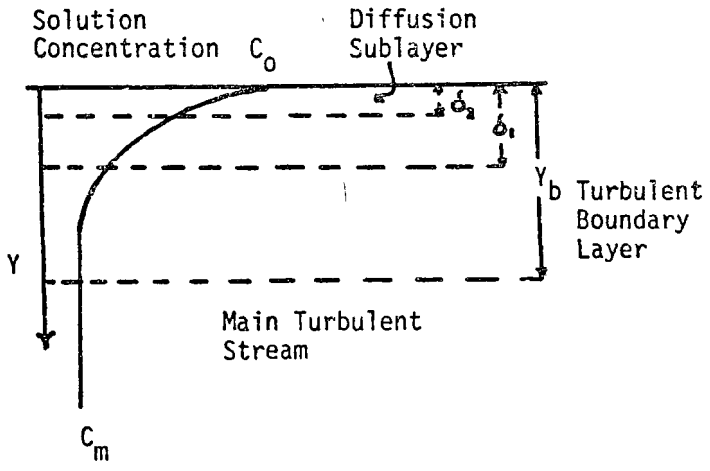

Figure 7. Levich Model for Turbulent Pipe Flow.

equating the fluxes and supplying appropriate boundary conditions. In the outermost zone, $\delta_1 \leq y \leq y_b$, transport takes place by turbulent mixing, a convective action. In the middle zone, $\delta_2 \leq y \leq \delta_1$, the eddy diffusion coefficient, D_e is presumed much larger than D_i so that transport occurs by eddy diffusion at a flux equal to D_e times the concentration gradient across the zone. In the inner zone, $0 \leq y \leq \delta_2$, transport is based solely on molecular diffusion at a flux equal to D_i times the concentration gradient across the zone. Based on this analysis by Levich which was extended by Davies (30) the following relationship for the mass flux developed.

$$\overline{N}_i = \frac{.0075 D_i (C_B - C_o)}{R} Re^{+0.88} Sc^{+1/3} \tag{76}$$

This solution appears to be more closely in line with published data. Empirical correlations based solely on experimental data will be presented next.

Empirical Correlations

Two empirical correlations are commonly used to characterize mass transport in turbulent pipe flow. The Chilton-Colburn (31) correlation arose in 1934 out of an effort to correlate heat transfer data in turbulent pipe flow with available mass transfer data. It remains a useful correlation and is given as follows:

$$N_{i(avg)} = \frac{.0115\ D_i(C_B - C_o)}{R} Re^{0.8}\ Sc^{1/3} \tag{77}$$

Another commonly cited correlation is that of Harriott and Hamilton (32):

$$N_{i(avg)} = \frac{.0048\ D_i(C_B - C_o)}{R} Re^{0.913}\ Sc^{0.346} \tag{78}$$

Both relationships express the mass flux in terms of a value that is averaged over distance down the pipe in a region of fully developed turbulent flow. Note that the functional form of these correlations is similar to the solutions of the convective diffusion equation. While similar in form, the two approaches, theoretical and empirical, represent different points of view. The theoretical approach has its roots in some conceptual model of the phenomenon which may be a highly idealized (or naive) representation of what is actually going on. Empirical correlations, on the other hand, make no pretenses at phenomenological explanations, they simply reflect the actual tendencies that exist in measured data. Clearly both have merit as well as limitations.

Mass transport through a stagnant liquid can be viewed as a special case of the convective-diffusion problem where all components of solution velocity are zero. In this case the velocity term of equation (56) vanishes and the following relationship results:

$$\frac{\partial C_i}{\partial t} = D_i \nabla^2 C_i \tag{79}$$

For the one-dimensional case in cartesian coordinates, the relation is a statement of Fick's Second Law:

$$\frac{\partial C_i}{\partial t} = D_i \frac{\partial^2 C_i}{\partial x^2} \tag{80}$$

with the following boundary conditions:

at: $t = 0$: $C_S = C_{B_{bulk}}$ -- conc. at electrode equals that of the

$t > 0$: $C_S = 0$ -- completely diffusion controlled

and as $x \longrightarrow \infty$, $C(x,t) \longrightarrow C_B$

the standard solution, $C(x,t)$, to this differential equation is given (33) as:

$$C(x,t) = C_B \text{ erf} \left[\frac{x}{2D^{1/2} t^{1/2}} \right] \tag{81}$$

where erf (z) is short for the error function of Z, a standard function with values given in Table 4 below.

Table 4
Mass Transfer to Stationary Electrodes in Quiet Solutions
from Adams p. 48

Z	erf Z
0	0.0000
0.2	0.2227
0.4	0.4284
0.8	0.7421
1.0	0.8427
1.2	0.9103
1.6	0.9764
2.0	0.9955
2.5	0.9996
3.0	0.999
∞	1.000

Of interest, in corroding systems is not so much the concentration profile but the rate of mass transport through solution to the solid/solution interface where the reaction occurs.

This rate is given as a flux, N, in (moles/cm^2 sec) to the surface as follows:

$$N_{at\ x=0} = D(\partial C/\partial X)_{x=0} = \frac{D^{1/2}\ C_B}{\pi^{1/2}\ t^{1/2}} \tag{82}$$

So, the surface flux is a function of both time and bulk concentration for a species being transported from the bulk to the surface to participate as a reactant in a reaction at the solid/solution interface. Adams (33) reports that conditions required for semi-infinite linear diffusion are difficult to maintain for periods longer than about 30 to 45 seconds. Natural convection due to thermal gradients and environmental vibrations tend to mix the solution and limit the time of stagnation.

The flux given above is an instantaneous value which changes with time. A more appropriate value for a corroding system with stagnant water would be a time-averaged value of the mass flux. Such a value can be determined by integrating the instantaneous flux, N_i, over a stagnation time period, t, and then dividing by t (34):

$$N_{(avg)} = \frac{1}{t} \int_0^t N_{i(at\ x=0)}\ dt \tag{83}$$

which turns out to be the following:

$$N_{avg} = 2\left[\frac{D_i}{\pi t}\right]^{1/2} C_B \tag{84}$$

This relationship is applicable only when the solid surface is acting like a shielded electrode (35, 36), that is, when the solid surface completely surrounds the liquid in the directions normal to that of mass transport. So the actual surface of a corroding pipe does act as a shielded electrode, but a rotating disc electrode inserted into solution for corrosion rate measurement does not.

The correction factor for conditions where the electrode is not shielded has been derived by Soos and Lingane (35) and Lingane (36) to be:

$$[1 + a(Dt/r^2)^{1/2}]$$

where: a = 2.12 (a constant)

r = electrode radius (cm) for disc electrode

The average flux to an unshielded electrode over time period t is then:

$$N_{avg} = \frac{2D^{1/2}C_B}{\pi^{1/2}\ t^{1/2}} [1 + a(\frac{Dt}{r^2})^{1/2}] \tag{85}$$

For solution species that are products of the corrosion reaction which must diffuse away from the electrode surface to the bulk the average flux over time period t is given (34) as:

$$N_{avg} = 2(C_S - C_B)(D/\pi t)^{1/2} \tag{86}$$

where C_S is the surface concentration of the diffusing species and C_B is its concentration in bulk solution. Applying the correction factor for an unshielded electrode, the average flux becomes:

$$N_{avg} = 2(C_S - C_B)(D/\pi t)^{1/2}[1 + a(Dt/r^2)^{1/2}] \tag{87}$$

Equations (85) and (87) describe the flux to and from a reacting interface under conditions of stagnant fluid. It could be noted that the temperature dependence of the mass flux is hidden in the values of the diffusion coefficients, D, which are temperature dependent.

Secondary Effects

Solution mass transport models presented so far account only for the effects of flow velocity, geometry, and species concentration. These are perhaps the most influential parameters in determining the rate of mass transport. Other parameters, such as temperature, surface roughness, and pipe diameter exert influences on mass transport rates as well, but to a lesser extent.

Temperature effects are manifested through the magnitude of the diffusion coefficient, D_i. The value of D_i at temperatures other than 25°C can be calculated from the following relationship (24):

$$\frac{D_1\mu_1}{T_1} = \frac{D_2\mu_2}{T_2} \tag{88}$$

where μ is the viscosity of water in centipoises and T_1 and T_2 are temperatures in °K. The diffusivity of H^+ is calculated below for a temperature of 5°C:

$$D_{5°C} = (9.32 \times 10^{-5} \frac{cm^2}{sec})(\frac{278°K}{298°K})(\frac{0.8937\ cp}{1.5188\ cp}) = 5.12 \times 10^{-5} \frac{cm^2}{sec}$$

μ Viscosity of Water	
5°C	1.5188 cp
15°C	1.1404 cp
25°C	0.8937 cp

A reduction of nearly 50% for a temperature change of only 20°C. From the Levich equation for turbulent transport one can see that:

$$\frac{N_i(T)}{N_i(25°C)} = \left[\frac{D_i(T)}{D_i(25°C)}\right]^{2/3}$$

Using this relationship:

$$N_i(5°C) = 0.670\ N_i(25°C)$$

Other factors remaining constant, a change in temperature from 25°C down to 5°C reduces the mass transport rate to roughly two-thirds its former value.

Pipe size effects enter directly through the R term in Levich's equation:

$$\frac{N_i(1/2\ in)}{N_i(1\ in)} = \left[\frac{R(1/2\ in)}{R(1\ in)}\right]^{-1/3}$$

In this case, with other factors being equal:

$$N_i(1/2\ in) = 1.26\ N_i(1\ in)$$

The effect of a reduced pipe diameter from 1 in to 1/2 in is to increase the mass flux by roughly one-fourth when both pipes have the same flow rate. For tubulent flow the ratio of pipe radii shown above is raised to the -0.12 power.

In corroding systems, where oxide films or other corrosion products form on the surface of a metal, initially smooth metal surfaces become quite rough. Figure 8 shows what a corroded metal surface may look like at high magnification. All mass transfer relationships presented so far have been derived for flow through smooth pipes. This is a condition that seldom

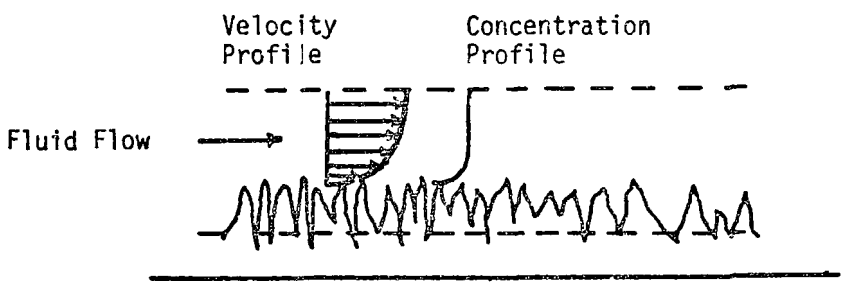

Figure 8. Surface Roughness, Velocity, and concentration Profiles in Turbulent Pipe Flow.

exists for pipes carrying natural waters in the near neutral pH range, since solid phase corrosion products are almost always observed. The presence of corrosion products invariably roughens the solid surface which in turn influences the fluid flow. Close to the solid surface small eddies are created which reduce the thickness of the laminar diffusion layer (δ_2 in Levich's (21) model). The mass flux to the surface is increased as δ_2 is reduced. Davies (30) has presented the following relationship which describes the effect of surface roughness:

$$N_i = \frac{D_i(C_B - C_S)}{\text{const.}} \; Re^{0.1} \; Sc^{0.5} \; (e/d)^{0.15} \qquad (89)$$

Here e is the height of surface protrusions and d is the diameter of the pipe. Generally, (e/d) values range from 0.0001 for relatively smooth surfaces to values near 0.05 for relatively rough surfaces. Using the relationship above, one can estimate the impact of surface roughness on the mass flux:

$$\frac{N_{i(rough)}}{N_{i(smooth)}} = \frac{(e/d)_r^{0.15}}{(e/d)_s^{0.15}}$$

Using $(e/d)_r = 0.05$ and $(e/d)_s = 0.0001$, and calculating the ratio of mass fluxes:

$$N_{i(rough)} = 2.54\ N_{i(smooth)}$$

So the mass flux to the surface may be more than doubled as the surface becomes roughened by buildup of corrosion products. This is an important aspect of solution phase mass transport that is not very well characterized at present and makes precise quantitative estimation of mass fluxes in real world corroding systems difficult.

Thus, it is shown that each factor considered:

pipe size
pH
flow velocity
temperature
surface roughness

can significantly influence the rate of mass transport of reacting species to from the pipe surface.

Applications of Mass Transfer Analysis To Aqueous Copper Corrosion

Estimating the effects of solution mass transport on corrosion rates, has received much attention in the literature. Studies have focused principally on transport of molecular oxygen to the reacting surface under conditions of laminar or turbulent flow. Results of a few of these studies will be presented here.

The corrosion of copper tubing under solution mass transport control has been studied by several authors. Cornet et al. (37) have presented experimental results for copper corrosion by 2.1 N H_2SO_4 at 30°C. Experiments were done for 1/2, 3/4, and 1 inch diameter pipes over a range of flow velocities ($300 \leq Re \leq 10^5$) that included laminar and turbulent flow regimes. Under these conditions the rate imiting flux was that of molecular oxygen which was

shown to vary greatly with flow velocity and be virtually independent of pipe diameter. A sharp increase in mass flux was observed as the flow transitioned from laminar to turbulent flow (Re $\geq$ 4000). At Re $\geq 10^4$ the corrosion rate shows the effects of mixed control, that of reaction kinetics and solution mass transport, which greatly reduces the dependence of corrosion rate on fluid velocity, Re. Figure 9 shows these trends:

Frank-Kamenetskeii et al. (38) have studied copper corrosion in nitric acid under conditions of rate control by molecular oxygen transport. Their data, presented in Figure 10 below, covers both laminar and turbulent flow conditions and shows a sharp increase in mass flux as the flow becomes turbulent. Here the Peclet number, Pe, is defined as:

$$Pe = ReSc = \frac{2R\langle v_y \rangle}{D_i} \tag{90}$$

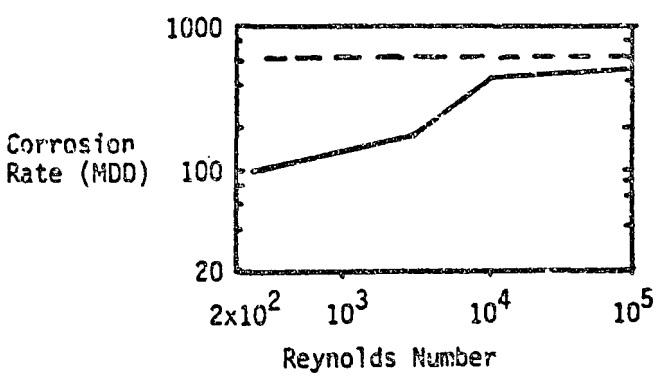

Figure 9. Copper Corrosion Rate Versus Pipe Flow Reynolds Number from Cornet et al. (37)

The Nusselt number, Nu, for mass transport, also called the Sherwood number, Sh, is defined as a dimensionless mass flux:

$$Nu = \frac{2R}{D_i(C_B - C_s)} N_i \tag{91}$$

So, Figure 10 is essentially a plot of mass flux versus flow velocity.

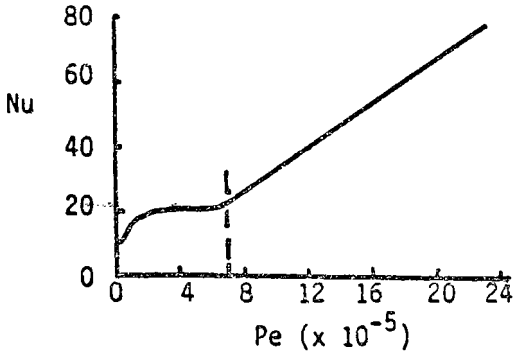

Figure 10. Mass Transport Dependence of Copper Corrosion in Nitric Acid Acid from Frank-Kamenetskeii et al. (38).

Roberts and Shemilt (39) have presented results of mass transport controlled copper corrosion in near neutral pH solution. Their study was aimed at assessing the effects of strain on oxide film rupture and repair under laminar flow conditions. Their results show, at least qualitatively, the expected increase in rate of mass transport with increasing flow velocity. The modified Sherwood number used in Figure 11 is just the Sherwood number multiplied by a constant that relates it to oxide film strain, and as such, it is still a qualitative indicator of mass flux. The effect of oxygen concentration variations on the mass flux is difficult to explain and raises the possibility that molecular oxygen may not be the rate limiting reactant in this system.

Zembura (40) investigated the rate of copper corrosion in a mixed electrolyte of 0.1 M Na_2SO_4 and H_2SO_4 at pH values that were varied roughly from 0.5 to 4.5. Using a rotating disc electrode, he was able to measure both the kinetic rate of copper dissolution and solution mass transfer rates. The experimental results, shown in Figure 12, indicate that the kinetics of copper dissolution were rate controlling from $0.5 \leq pH \leq 3.8$. Above this pH range mass transport of H^+ became rate limiting. At no time was the

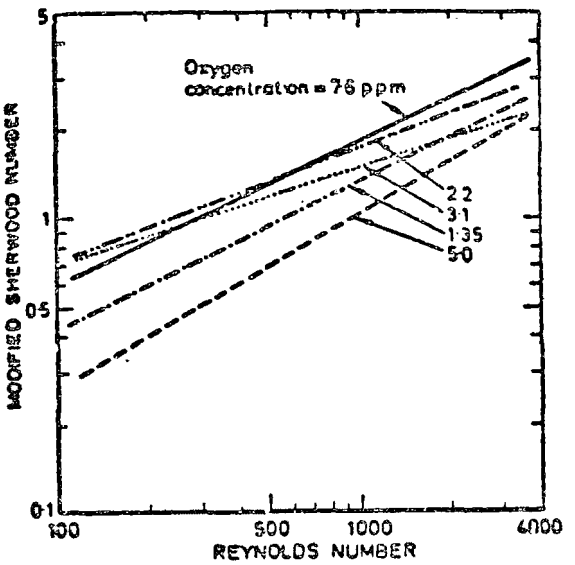

Figure 11. Mass Transport Dependence of Copper Corrosion in Neutral Solutions from Roberts and Schemilt (39).

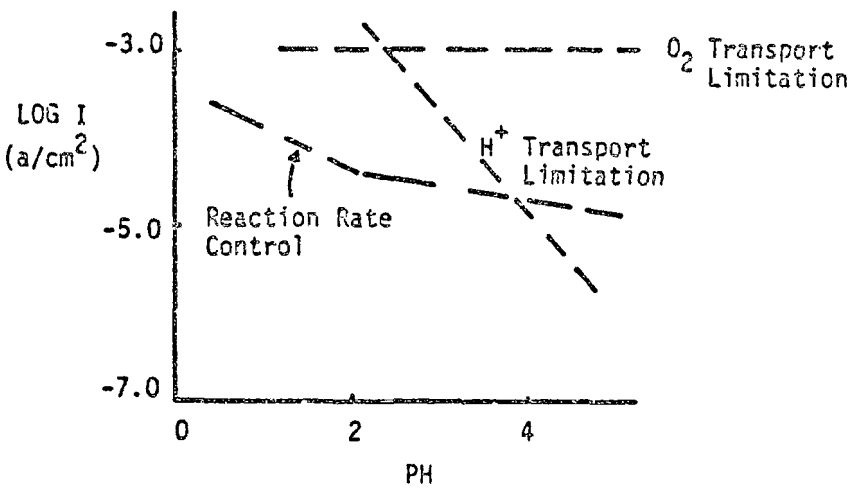

Figure 12. Corrosion Rate of Copper in H_2SO_4 Versus Hydrogen Ion Concentration Under Varied Conditions of Rate Control from Zembura (40).

corrosion rate high enough to be rate limited by O_2 mass transport, even though O_2 reduction was shown to be the reduction half cell reaction. As indicated by Zembura and Fulinski (41) both O_2 and H^+ are involved in the O_2 reduction half-cell reaction. As the solution pH is raised to 4 or above the mass flux of H^+ becomes less than the mass flux of O_2 due to the small molar concentration of H^+ at these higher pH values.

This work has interesting implications for copper corrosion in slightly acidic natural waters. Here hydrogen ion concentrations range from 10^{-6} M to 10^{-7} M indicating that hydrogen ion mass fluxes could be even more limiting than in Zembura's work.

Mass Transport Summary

Rate expressions for convective-diffusion of solution species under conditions of stagnant, laminar, and turbulent flow are all important for modeling real corroding systems. The rate expression for steady-state solution mass transport to or from the solid/solution interface can be formulated in the following general form:

$$i_{mT} = \frac{nFD(C_1 - C_2)}{D} \tag{92}$$

This form is appropriate for species being transported to or from the interface under conditions of stagnant, laminar, and turbulent flow. For the case of a reacting species diffusing toward the interface, such as O_2 and H^+:

C_2 = 0 surface concentration $\longrightarrow$ 0 for complete diffusion control

C_1 - bulk concentration of reacting species

For the case of a reaction product, such as OH^-, diffusing away from the interface:

C_1 = the steady state concentration of the reaction product at the interface

C_2 - concentration of diffusing reaction product in bulk solution

Differing flow conditions are accounted for by defining δ_D differently for stagnant, laminar, and turbulent flow. A concise summary of rate expressions for solution mass transport is contained in Table 5.

SUMMARY OF SECTION 4

Rate expressions have been developed and presented in this section which show explicitly the dependence of each type of rate process on chemical species in solution, solution temperature, and hydrodynamic flow regime. Although presented separately, all three of the fundamental rate processes mentioned in this section act together to compose an actual corroding system. The overall corrosion rate may be controlled by only one rate process or jointly by two or more. After measuring rates of each fundamental process separately and comparing their magnitudes under identical environmental conditions one may determine which rate processes actually control the rate of uniform copper corrosion in drinking water. Based on that determination one may assess the relative influence of environmental parameters such as chemical composition of the solution, solution temperature, and flow regime. These efforts are left for later chapters.

Table 5

Summary of Rate Expressions for Solution Mass Transport Rate Control

$$R = \frac{nFD(C_1 - C_2)}{\delta_D}$$

a) $C_1 = \begin{cases} C_B \text{ (bulk conc.): for diffusion toward interface } (H^+, O_2) \\ C_S \text{ (interfacial conc.): for diffusion away from interface } (OH^-) \end{cases}$

b) $C_2 = \begin{cases} 0\text{: for diffusion toward interface } (H^+, O_2) \\ C_B\text{: for diffusion away from interface } (OH^-) \end{cases}$

c) $\delta_D = \begin{cases} 0.5\ (\pi Dt)^{1/2} & \text{stagnant diffusion} \\ 1.453\left[\frac{\langle v_y \rangle}{y\ D\ R}\right]^{-0.333} & \text{laminar diffusion} \\ 133.3 R\ Re^{-0.88}\ Sc^{-0.333} & \text{turbulent diffusion} \end{cases}$

SECTION 5

EXPERIMENTAL PROCEDURE

INTRODUCTION

The approach taken in this study was to identify physical and chemical properties of the copper/cuprous oxide/Tolt River water system that exert an influence on the overall rate of uniform corrosion of copper tubing used for cold water plumbing. Then by varying the magnitudes of these influential parameters, conditions favorable to a minimized rate of copper corrosion could be determined. This was felt to be an important step in developing a rational and economic control strategy for copper corrosion in Tolt River water. It would also serve as a demonstration of the utility of electrochemical methods for corrosion rate measurements in low conductivity drinking water.

Identification of parameters exerting an influence on the overall process evolved out of the development of rate expressions for each of the component processes, derived in Section 4, which show explicitly the dependence of the rate of that process on the chemical and physical properties of the system.

Solution pH and temperature were found to be two parameters strongly influencing the rate of each process modeled in Section 4 and were therefore pinpointed as useful indicator variables to fit mechanistic models to measured data. Experiments designed to measure corrosion rates under rate control by each of the component rate processes were then performed at varied pH and temperature.

The principal measurement made in this study was the electrochemical determination of corrosion rate. This measurement was repeated many times under varied conditions of solution composition, temperature, and type of rate control. Experimental design consisted of systematic variation of these

conditions in such a way that measured corrosion rates could be compared directly with rate expressions developed in Section 4 for each of the component rate processes. Appropriate mechanisms for each component rate process could then be evaluated and a mathematical model for the overall corrosion process developed. This chapter contains a description of the type of data as well as the manner in which it was measured. The logic and details of the experimental approach used are developed first. A section on electrochemical methods which includes general background information on how the methods work, what they measure, and a brief accounting of the basic equipment necessary to measure corrosion rates electrochemically, is next. This is followed by an explanation of the experimental apparatus actually used in this research along with a complete account of the laboratory setup and procedure used in corrosion rate determinations. The laboratory setup and procedure used to conduct weight loss testing is described in the final section of the chapter.

LABORATORY PHASE OF THE STUDY

As stated earlier, all data taking in this study involved measurement of corrosion rate under varied conditions of rate control, chemical composition of the solution, and temperature. The entire measurement effort can be divided up into the following four distinct sets of corrosion rate measurements:

1) Interfacial Reaction Rate Control, measured electrochemically;
2) Oxide-Film Growth and Transport Rate Control, measured electrochemically;
3) Stagnant Diffusion in Solution Rate Control, measured electrochemically; and
4) Stagnant Diffusion in Solution Rate Control, measured by weight loss.

The first three of these sets of measurements correspond to the component rate processes modeled in Section 4. The final set was used for quantitative comparison of corrosion rate measurement by weight loss and electrochemical tests.

Data under kinetic rate control were taken by designing experiments in which possible rate limitations by oxide film transport was eliminated and the possibility of rate control by solution mass transport reduced. This was done by running polarization curves on freshly polished copper electrodes rotated at 3000 RPM. Any oxide film was effectively removed from the electrode surface by polishing. Rotation of the rotating disc electrode at 3000 RPM reduces the diffusion layer thickness in the solution to such a small value that the concentration gradient increases greatly and solution mass transport for most species is capable of proceeding at rates much greater than those determined experimentally. Figure 13 shows a schematic of the metal/solution system in which corrosion rates under kinetic rate control are measured. These rates correspond to the kinetics of the process at the metal/solution interface that is rate controlling. This could be metal dissolution, early stage oxide film growth, or molecular oxygen reduction. Rate expresions, derived in Section 4, were presented for each of these reactions as a function of pH and temperature. Comparison of the pH and temperature dependence of the rates with that of measured data will provide a basis for selection of a rate controlling process under these experimental conditions.

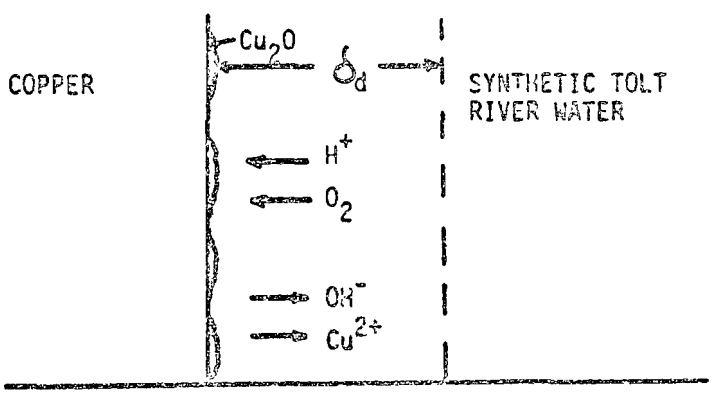

Figure 13. Metal/solution system for Experiments Designed to be Under Kinetic Rate Control.

Data under rate control by oxide film growth and solid state transport were taken by designing experiments in which possible rate limitations by

interfacial reaction kinetics and solution mass transport were eliminated. This was done by running polarization curves on an electrochemically aged copper electrode rotated at 3000 RPM. The electrochemical aging process consisted of passing a 10 μa anodic current across the electrode/solution interface for a period of two hours, promoting oxide film growth. Oxide films were grown at a variety of cell currents and over a range of time periods. Those grown at 10 μA for two hours gave the lowest cell current values, indicating that they most nearly represented complete film transport control. Rotation of the rotating disc electrode at 3000 RPM, as explained earlier, insures that solution mass transport processes are capable of proceeding at high rates and thereby reducing the possibility of rate control by solution mass transport. Figure 14 shows a schematic of the metal/oxide/solution system in which these corrosion rates are measured. Measured rates then correspond to the rate of oxide film growth, which is limited by charge transport across the film. Rate expressions, developed Section 4, for early and late stage growth of oxide films by the electron tunneling mechanism were presented as as function of pH and temperature. A comparison of these rate expressions with measured data provide a basis for determining which film growth model is appropriate. Once the appropriate model is identified the dependence of its rate on chemical species in solution other than pH can be noted in addition to its pH dependence.

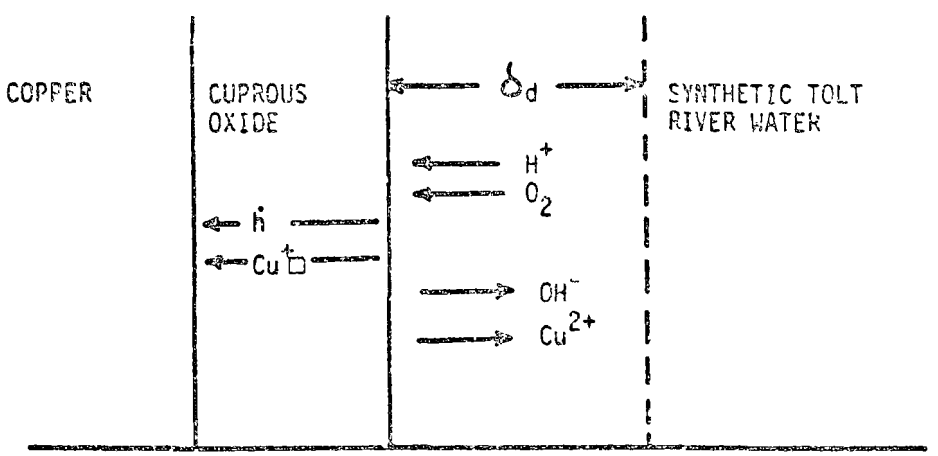

Figure 14. Metal/Oxide/Solution System for Experiments Designed to be Under Film Growth Rate Control.

Data under rate control by solution mass transport were taken by designing experiments in which possible rate limitations by interfacial reaction kinetics and oxide film growth were eliminated. This was done by running polarization curves on freshly polished copper electrodes that were not rotated. Under these experimental conditions mass transport in solution was expected to be the slowest step in the corrosion process. Figure 15 shows a schematic diagram of the metal/solution system from which corrosion rate data presented in this section were measured. Measured rates, then, correspond to the rate of mass transport of H^+ or O_2 to the electrode surface through stagnant media, or the rate of stagnant diffusion of OH^- away from the electrode surface to the bulk solution. Rate expressions developed in Section 4, for H^+, OH^-, and O_2 mass transport in stagnant solution were presented as a function of pH and temperature and can be compared with measured data. On this basis the rate controlling diffusion process is identified. Experiments to measure corrosion rates under rate control by each of the component rate processes composing copper corrosion in drinking water were designed to be carried out at varied pH ($6.0 \leq pH \leq 8.3$) and temperature ($5°C \leq T \leq 25°C$). This data could then be compared with rate expressions developed in Section 4, and an overall process model developed by putting together quantitative models of appropriate rate processes. Those efforts are described in Sections 6 and 7. This chapter continues with an explanation of the electrochemical corrosion rate measurements used.

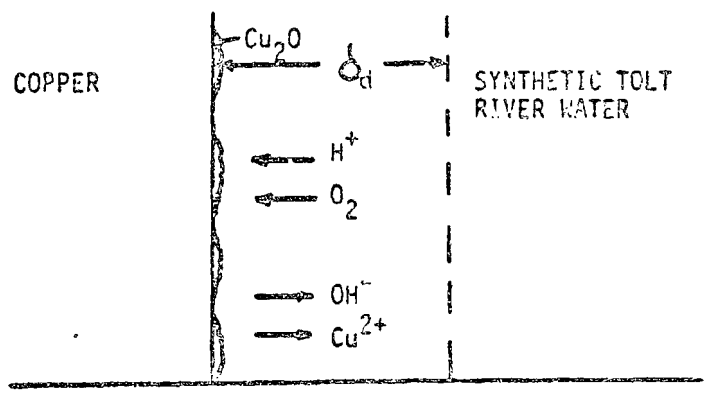

Figure 15. Metal/Solution System for Experiments Designed to be Under Solution Transport Rate Control.

ELECTROCHEMICAL METHODS

Electrochemical methods have been used in corrosion research for some twenty-five years (1), in the past decade these methods have been developed on a quantitative basis (2) for use in drinking water systems, especially for waters of low conductivity (< 150 μmos/cm) (3). The principal advantage of electrochemical methods is that a corrosion rate determination can be made rapidly. This is advantageous from the point of view of error assessment, since replicate runs can be readily made to assess the reproducibility of a measurement. Another advantage is that an instantaneous rate of corrosion is measured, as opposed to a rate averaged over a period of several months as in a weight loss coupon test. Rapid and instantaneous corrosion rate measurements are useful in observing the change in corrosion rate that occurs with slight changes in solution composition, an important consideration in this research. How electrochemical methods work and what they actually measure is described in the upcoming section on fundamentals.

Fundamentals

Electrochemical methods can be used to measure corrosion rates in aqueous systems because oxidation-reduction reactions are involved. Consider the simple pair of redox half-cell reactions shown below:

$$Me \xrightarrow{k_{ox}(E)} Me^{+1} + e^- \tag{1}$$

$$1/4\ O_2 + H^+ + e^- \xrightarrow{k_{re}(E)} 1/2\ H_2O \tag{2}$$

Since each half-cell reaction involves the transfer of electrons, the magnitude of the kinetic rate constants, $k_{ox}(E)$ and $k_{re}(E)$, are functions of electrode potential. They can be written in the following form:

$$k_{ox}(E) = k^o_{ox} \exp\left(\frac{E - E^o_{ox}}{b_a}\right) \tag{3}$$

$$k_{re}(E) = k^o_{re} \exp\left(\frac{-E + E^o_{re}}{b_c}\right) \tag{4}$$

Here, k°_{ox} and k°_{re} are the potential independent portions of the rate constants and can be characterized by an Arrhenius type expression as a function of temperature. The term E in both expressions represents the electrode potential measured with respect to a reference potential, which in this case is that of the Saturated Calomel Reference Electrode. E°_{ox} is the equilibrium potential for the oxidation half-cell and can often be calculated from the Nernst equation. E°_{re} is the equilibrium potential for the reduction half-cell and can be calculated from the appropriate Nernst equation. The constants b_a and b_c are called the anodic and cathodic Tafel slopes respectively and have numerical values characteristic of the particular half-cell reaction they represent.

The velocity of each half-cell reaction can be written in the forms shown below (omitting back reactions) when the corrosion potential is sufficiently far from either half-cell equilibrium potential that its forward reaction term predominates over the back reaction term. This is normally the case. The reaction velocities of the oxidation and reduction half-cells can be expressed as follows:

$$V_{ox} = k_{ox}(E)[Me] = [Me]k^{\circ}_{ox} \exp\left(\frac{E - E^{\circ}_{ox}}{b_a}\right) \tag{5}$$

$$V_{re} = k_{re}(E)[O_2]^{1/4}[H^+] = k^{\circ}_{re}[O_2]^{1/4}\,[H^+] \exp\left(\frac{-E + E^{\circ}_{re}}{b_c}\right) \tag{6}$$

Since these reaction velocities represent the rates at which electrons are transferred, they can be expressed in the units of current (amperes) or current density (amperes/cm^2):

$$i_{ox} = \frac{I_{ox}}{A} = \frac{nFV_{ox}}{A} \tag{7}$$

$$i_{re} = \frac{I_{re}}{A} = \frac{nFV_{re}}{A} \tag{8}$$

Where i_{ox} and i_{re} are the reaction velocities of the oxidation and reduction half-cell reactions respectively expressed as current densities (amps/cm^2). Here A is the surface area of the electrode in cm^2, n is the number of elec-

tron equivalents per mole of reactant consumed (n 1 for each half cell as written), and F is the Faraday Constant (96,485 coul/equiv).

The half-cell current densities can be expressed in the following form:

$$i_{ox} = \frac{nF}{A} [Me]\, k^{\circ}_{ox} \exp \frac{E-E^{\circ}_{ox}}{ba} - i^{\circ}_{ox} \exp \frac{E - E^{\circ}_{ox}}{ba} \tag{9}$$

$$i_{re} = \frac{nF}{A} [O_2]^{1/4} [H^+]\, k^{\circ}_{re} \exp(- \frac{E - E^{\circ}_{re}}{bc}) = i^{\circ}_{re} \exp(- \frac{E - E^{\circ}_{re}}{bc}) \tag{10}$$

This current densities oppose one another in direction so that the net current density flowing in the cell is:

$$i = i_{ox} - i_{re} \tag{11}$$

These current density equals zero when the electrode potential equals the corrosion potential, E_{cor}, and the current densities of each half-cell equal the corrosion current density, i_{cor}:

$$i_{ox}(E = E_{cor}) = i_{re}(E - E_{cor}) = i_{cor}$$

$$i_{cor} = i^{\circ}_{ox} \exp(\frac{E_{cor} - E^{\circ}_{cor}}{ba}) = i^{\circ}_{re} \exp(- \frac{E_{cor} - E^{\circ}_{re}}{bc}) \tag{12}$$

Simultaneous solution of equations (9) through (12) yields the Stern-Geary (4) equation:

$$i = i_{cor}[\exp(\frac{E - E_{cor}}{ba}) - \exp(- \frac{E-E_{cor}}{bc})] \tag{13}$$

This equation relates the net current density, i, flowing in an electrochemical cell with values of electrode potential, E. Both of these parameters, i and E, are measurable, and if an experimental plot of i vs. E can be obtained the values of i_{cor}, E_{cor}, b_a, and b_c can be evaluated. This, of course, is how corrosion rates are determined electrochemically.

As derived here the Stern-Geary equation describes the dependence of cell current on electrode potential in a corroding system where both anodic and cathodic half-cell reactions are proceeding under rate control by chemi-

cal kinetics. Each half-cell current density then exhibits the following exponential form:

$$i_{ox} = i_{cor} \exp\left(\frac{E - E_{cor}}{ba}\right) \tag{14}$$

$$i_{re} = -i_{cor} \exp\left(-\frac{E - E_{cor}}{bc}\right) \tag{15}$$

with the measured cell current density being the algebraic sum of these two half-cell current densities. A plot of cell current density versus electrode potential is called a polarization curve. Figure 16 shows a typical polarization curve for a corroding system in which both half-cell reactions are proceeding under rate control by chemical kinetics. The solid line is a trace of the measured cell current density at corresponding values of electrode potential, E. The broken lines refer to the half-cell current densities. The cathodic (reduction) half-cell current is shown here as negative since it flows in a direction opposite to that of the anodic (oxidation) half-cell which is positive by convention.

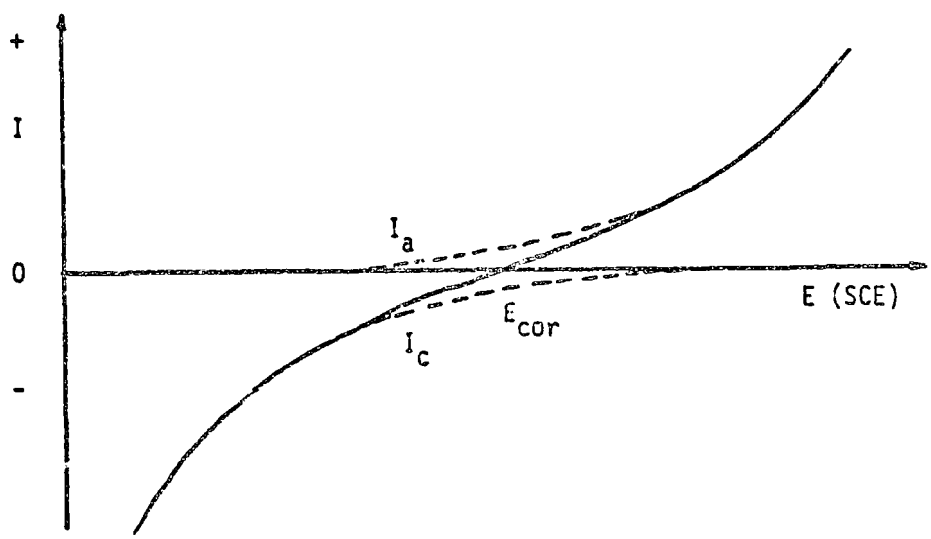

Figure 16. Polarization Curve.

The experimental output of an electrochemical corrosion rate determination is this plot of net cell current density, i ($\mu A/cm^2$), versus electrode potential, E (mv vs. SCE). The corrosion rate is then calculated from this plot called a polarization curve. This curve can then be fit to the Stern-Geary model and I_{cor}, b_a, and b_c calculated. Although derived solely for reactions under kinetic rate control, the Stern-Geary model has practical use in systems where one half-cell reaction is diffusion controlled, as well.

When the cathodic half-cell reaction is diffusion controlled, the second exponential term in the Stern-Geary equation is no longer potential dependent and approaches 1.0 in value ($b_c \longrightarrow -\infty$). The Stern-Geary equation then takes the following form:

$$I = I_{cor}\left[\exp\left(\frac{E - E_{cor}}{b_a}\right) - 1\right] \tag{16}$$

The characteristic shape of a polarization curve measured under these conditions is shown in Figure 17. Once again the solid line refers to the cell current density, and the broken lines to the component half-cell current densities.

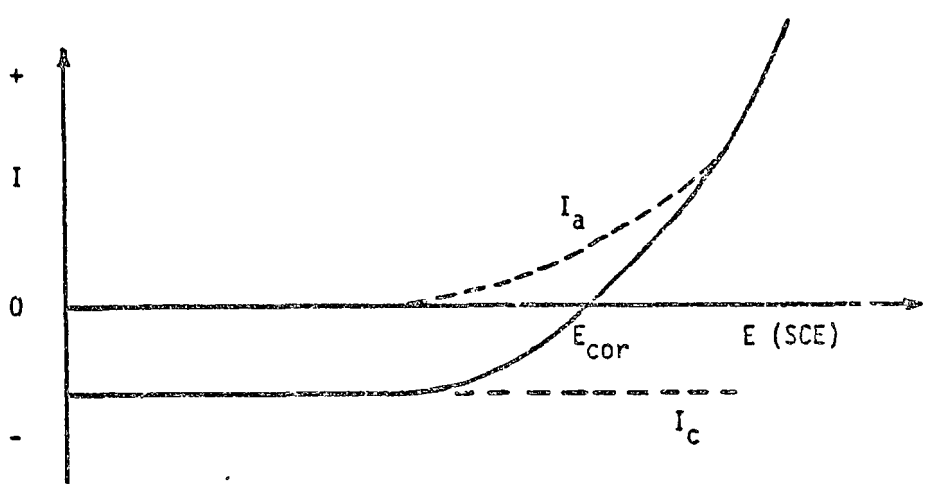

Figure 17. Diffusion Controlled Cathodic Half-Cell.

An analogous situation exists when the anodic reaction is diffusion controlled. The first exponential term in the Stern-Geary equation now is independent of potential and approaches 1.0 ($b_a \longrightarrow \infty$) in value. The Stern-Geary equation then becomes:

$$I = I_{cor}\left[1 - \exp - \left(\frac{E - E_{cor}}{b_c}\right)\right] \tag{17}$$

The characteristic shape of a polarization curve measured under these conditions is shown in Figure 18, with solid and broken lines having the same meaning as above.

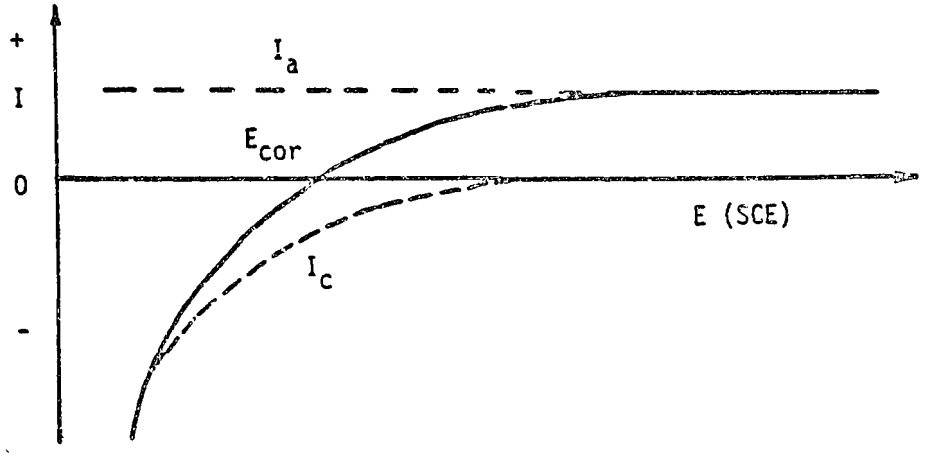

Figure 18. Diffusion Controlled Anodic Half-Cell.

All three of these combinations of rate control were encountered in the laboratory phase of this study, and all three polarization curve shapes are amenable to corrosion rate and tafel slope calculation. Methods for calculating these parameters from measured curves are discussed next.

Calculating Corrosion Rates from Polarization Curves

The most versatile and precise way of calculating corrosion rates from polarization curves was found to be the three-point method, originally

developed by Barnartt (5) for investigation of electrode reaction mechanisms, is directly applicable to corroding systems (6). The method is versatile in that it is applicable to electrode reactions where both half-cell reactions are proceeding under rate control by chemical kinetics or where one half-cell reaction is transport limited. Thus it provides a means of calculating corrosion rates measured under the three conditions of rate control modeled in this study. Algorithms are developed here for use in the calculations of the corrosion rate, anodic tafel slope, and cathodic tafel slope. Derived first for conditions of rate control by chemical kinetics, then for transport control of anodic reaction, and finally transport control of the cathodic reaction they are directly usable for data taken under rate control by interfacial reaction kinetics, oxide film growth and transport, and by solution mass transport respectively.

Kinetic Control

Beginning with the Stern-Geary equation:

$$I = I_{cor}\left[\exp\left(\frac{E-E_{cor}}{b_a}\right) - \exp\left(\frac{E-E_{cor}}{b_c}\right)\right] \qquad (18)$$

Note that in this form b_c is a negative number. The following terms can be defined (see Figure 19):

1) $I = I_1$, when $(E - E_{cor}) = \Delta E$
2) $I = I_2$, when $(E - E_{cor}) = 2\Delta E$
3) $I = I_3$, when $(E - E_{cor}) = -2\Delta E$
4) $u = \exp(\Delta E/ba)$
5) $v = \exp(\Delta E/bc)$
6) $r_1 = |I_2/I_3|$
7) $r_2 = |I_2/I_1|$

Based on these definitions the following relationships for I_1, I_2, and I_3 can be developed:

$$I_1 = I_{cor}(u - v)$$
$$I_2 = I_{cor}(u^2 - v^2)$$
$$I_3 = I_{cor}(u^{-2} - v^{-2})$$

So that:

$$r_1 = \left|\frac{I_2}{I_3}\right| = \left|\frac{I_{cor}(u^2 - v^2)}{I_{cor}(u^{-2} - v^{-2})}\right|$$

Multiplying through by (u^2v^2/u^2v^2) allows a more concise expression for r_1:

$$r_1 = \left|\frac{u^2v^2(u^2 - v^2)}{u^2v^2\ \frac{1}{u^2} - \frac{1}{v^2}}\right| - \left|\frac{u^2v^2(u^2 - v^2)}{(v^2 - u^2)}\right| = \left|-u^2v^2\right| = u^2v^2$$

In a similar fashion it can be shown that:

$$r_2 = \left|\frac{I_2}{I_1}\right| = u + v$$

To calculate the corrosion rate, I_{cor}, and values for the tafel slopes it is necessary to solve the following three equations simultaneously:

$$I_{cor} = I_1/(u - v)$$

$$r_1 = u^2v^2$$

$$r_2 = u + v$$

When this is done, the result is:

$$I_{cor} = \frac{I_1}{(r_2^2 - 4\sqrt{r_1})^{1/2}} \qquad (19)$$

If I_1 is in units of $\mu A/cm^2$, then I_{cor} has the same units. When I_1 is taken directly from the polarization curve its units are μA so the corrosion rate must be divided by the surface area of the electrode, A, in cm^2.

Tafel slopes can be calculated as well:

$$u = \exp(\frac{\Delta E}{ba}) \qquad \text{and } v = \exp(\frac{\Delta E}{bc})$$

So: $$ba = \Delta E/\ln u = \Delta E/(\ln[\frac{r_2+\sqrt{r_2^2 - 4\sqrt{r_1}}}{2}]) \quad (20)$$

likewise: $$bc = \Delta E/\ln v = \Delta E/\ln[\frac{r_2 - \sqrt{r_2^2 - 4\sqrt{r_1}}}{2}] \quad (21)$$

In order to calculate values for these parameters from an experimental curve three data points are needed, two of them selected at potentials positive with respect to E_{cor} and one negative with respect to E_{cor}. The first data point is arbitrarily selected to be (E_1,I_1) where $(E_1 - E_{cor}) = \Delta E$. Data point number two, (E_2,I_2), is then selected so that $(E_2 - E_{cor}) = 2\Delta E$ and data point number three, $(E_3 I_3)$, so that $(E_3 - E_{cor}) = 2\Delta E$. Figure 19 shows graphically this method of data point selection.

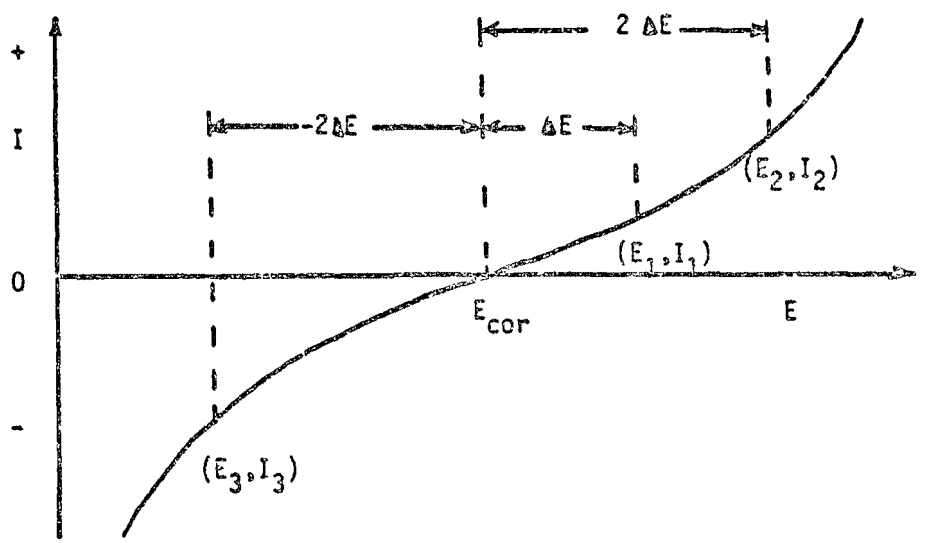

Figure 19. 3-Point Method for Calculating Corrosion Rate Under Kinetic Rate Control.

Once the points are chosen, the current magnitudes, $|I|$, at the three points can be used to calculate the corrosion rate using the following relationship derived by Barnartt.

$$i_{cor} = \frac{I_{cor}}{A} = \frac{I_1}{[|I_2/I_1|^2 - 4|I_2/I_3|^{1/2}]^{1/2} A} \quad (\mu A/cm^2) \tag{22}$$

Where A is the surface area of the working electrode in cm^2. This method has been used to calculate corrosion rates for polarization curves taken under kinetic rate control.

Transport Control of Anodic Reaction

The method to calculate corrosion rate derived in this section is appropriate for a corroding system in which the anodic (oxidation) reaction is transport controlled but the cathodic reaction is rate controlled by chemical kinetics. The form of the Stern-Geary equation that describes this situation is as follows:

$$I = I_{cor}\left[1 - \exp\left(\frac{E - E_{cor}}{bc}\right)\right] \tag{23}$$

Development of the method for corrosion rate calculation requires definition of the following terms:

1) $I = I_1$, when $(E - E_{cor}) = \Delta E$

2) $I = I_2$, when $(E - E_{cor}) = -\Delta E$

3) $I = I_3$, when $(E - E_{cor}) = -2\Delta E$

4) $v = \exp(\Delta E/bc)$

5) $r = \left|\frac{I_2}{I_3 - I_2}\right|$

Based on these definitions the following expressions can be developed for I_1, I_2, I_3 and r:

$$I_1 = I_{cor}(1 - v)$$
$$I_2 = I_{cor}(1 - 1/v)$$
and $$I_3 = I_{cor}(1 - 1/v^2)$$

so that:

$$r = \left| \frac{I_2}{I_3 - I_2} \right| = \frac{(1 - 1/v)}{(1 - 1/v^2) - (1 - 1/v)} = v$$

The corrosion rate can then be calculated from:

$$I_1 = I_{cor} (1 - r)$$

Since I_1, and r are of known value:

$$I_{cor} = \frac{I_1}{(1 - r)} \tag{24}$$

The value of the cathodic tafel slope, b_c, can also be calculated in a straightforward manner as follows:

$$b_c = \frac{\Delta E}{\ln r} \tag{25}$$

Data taken under rate control by oxide film growth and transport correspond to a situation where the anodic half-cell reaction is rate controlled by solid-state diffusion, but the cathodic half-cell is not. Figure 20 shows a polarization curve measured under conditions of transport control for the anodic half-cell along with the appropriate data points necessary to calculate the corrosion rate and cathodic tafel slope.

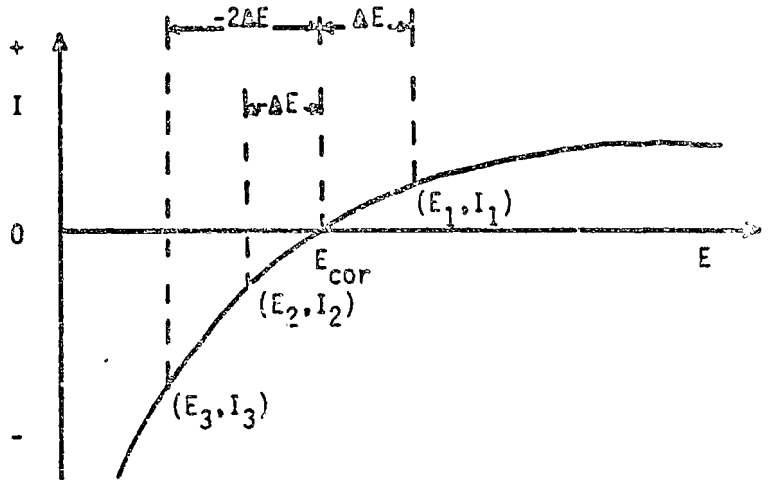

Figure 20. 3-Point Method for Calculating Rate Under Transport Control by Anodic Reaction.

The first data point (E_1, I_1) is arbitrarily selected above E_{cor} so that $(E_1 - E_{cor}) = \Delta E$. Data point number two (E_2, I_2) is chosen so that $(E_2 - E_{cor}) = -\Delta E$. The third data point, (E_3, I_3) is then chosen so that $(E_3 - E_{cor}) = -2\Delta E$. The corrosion rate is then calculated from the following relationship:

$$i_{cor} = \frac{I_{cor}}{A} = \frac{I_1}{A\left[1 - \left|\frac{I_2}{I_3 - I_2}\right|\right]} \quad (\mu A/cm^2) \tag{26}$$

and the corresponding cathodic tafel slope:

$$b_c = \frac{\Delta E}{\ln\left(\frac{I_2}{I_3 - I_2}\right)} \tag{27}$$

This method has been used to calculate corrosion rates from polarization curves measured under oxide film growth and transport control.

Transport Control of Cathodic Reaction

The method derived next is appropriate for calculation of corrosion rate and anodic tafel slope for a corroding system in which the cathodic reaction is transport controlled but the anodic reaction is rate controlled by chemical kinetics. The form of the Stern-Geary equation that describes this situation is:

$$I = I_{cor}\left[\exp\left(\frac{E - E_{cor}}{b_a}\right) - 1\right] \tag{28}$$

The following terms require definition for development of the method for corrosion rate calculation:

1) $I = I_1$, when $(E - E_{cor}) = \Delta E$
2) $I = I_2$, when $(E - E_{cor}) = -\Delta E$
3) $I = I_3$, when $(E - E_{cor}) = -2\Delta E$
4) $u = \exp(\Delta E/ba)$

and 5) $r = \left|I_2/(I_3 - I_2)\right|$

Based on these definitions, the following expressions can be developed for I_1, I_2, I_3, and r:

$$I_1 = I_{cor}(u - 1)$$

$$I_2 = I_{cor}(\frac{1}{u} - 1)$$

$$I_3 = I_{cor}(\frac{1}{u^2} - 1)$$

and $$r = \left|\frac{I_2}{I_3 - I_2}\right| = \frac{(\frac{1}{u} - 1)}{(\frac{1}{u^2} - 1) - (\frac{1}{u} - 1)} = u$$

The corrosion rate and anodic tafel slope can then be calculated from:

$$I_{cor} = \frac{I_1}{r - 1} \tag{29}$$

and $$b_a = \Delta E/\ln r \tag{30}$$

When the corrosion rate is controlled by transport through solution it is the cathodic half-cell that is diffusion controlled. This is observed visually by the shape of the polarization curve. Figure 21 shows the characteristic shape of a polarization curve with a diffusion controlled cathodic half-cell reaction.

The first data point, (E_1, I_1), is arbitrarily selected above E_{cor} so that $(E_1 - E_{cor}) = +\Delta E$. The second data point, (E_2, I_2) is selected below E_{cor} so that $(E_3 - E_{cor}) = -\Delta E$. The third data point, (E_3, I_3), is chosen below E_{cor} so that $(E_3 - E_{cor}) = -2\Delta E$. The corrosion rate and anodic tafel slope are calculated from:

$$i_{cor} = \frac{I_{cor}}{A} = \frac{I_1}{[(\frac{I_2}{I_3 - I_2}) - 1]A} \quad (\mu A/cm^2) \tag{31}$$

and $$b_a = \Delta E/\ln(\frac{I_2}{I_3 - I_2}) \quad (MV) \tag{32}$$

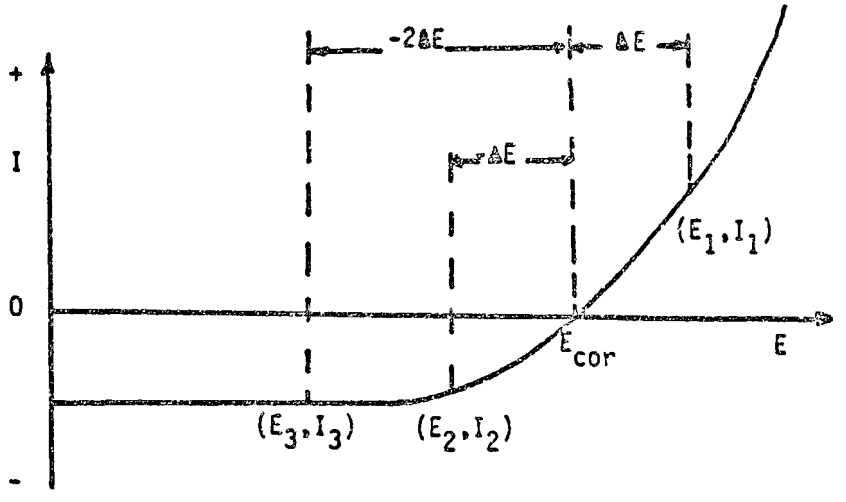

Figure 21. 3-Point Method for Calculating Corrosion Rate Under Transport Control by Cathodic Reaction.

Corrosion rates were calculated from polarization curves measured under rate control by solution mass transport in this fashion. In fact, all corrosion rate values presented in Section 6 involve electrochemical measurement and have been calculated by one of the three methods described here.

Instrumentation

The basic equipment required to generate a polarization curve consists of an electrochemical cell, a device to control electrode potential, a millivoltmeter to measure electrode potential, and a microammeter to measure cell current. The basic electrochemical cell is composed of three electrodes, the working electrode where the reaction whose rate is being measured occurs, a reference electrode which along with a luggin capillary allows measurement of electrode potential of the working electrode, and a counter electrode which is used to provide a reaction site for the half-cell reaction not being measured. The cell current which flows between the working and counter electrodes is measured with a microammeter. Electrode potential is measured with a millivoltmeter as the potential drop between the working and reference electrodes. A simple experimental system which can be used to generate polarization curves has been published in an ASTM Standard (7) and is shown

in Figure 22 below. By manually changing the electrode potential of the working electrode with the potentiostat and recording the cell current that flows at each electrode potential value, one can generate a polarization curve. This simple setup is not the actual experimental apparatus used on this project. It is presented here solely for the purpose of illustrating the basic manner in which a polarization curve is generated.

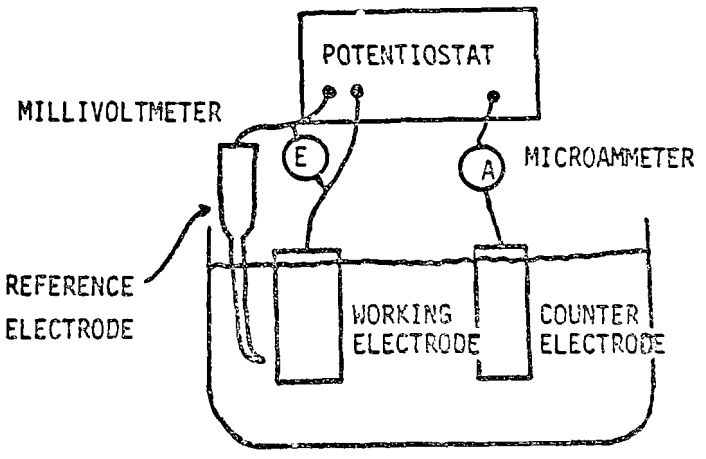

Figure 22. Basic Electrochemical Cell for Corrosion Rate Measurements.

The experimental apparatus used in this study is somewhat more elaborate than that shown in Figure 22 but contains the same essential electrochemical cell and potentiostat setup. Additional instrumentation includes a function generator (to sweep electrode potential linearly with respect to time), and X-Y recorder (to record the plot of cell current versus electrode potential), an IR Compensator (which allows removal of solution resistance effects in low conductivity water), and a rotating disc electrode (which allows measurements to be made under conditions of either kinetic or transport rate control). A schematic diagram of the instrumentation used is shown in Figure 23.

This setup allowed a somewhat automated polarization curve generation which tended to eliminate differences in operating procedures between runs and enhance reproducibility. Each component of this apparatus will now be described in greater detail.

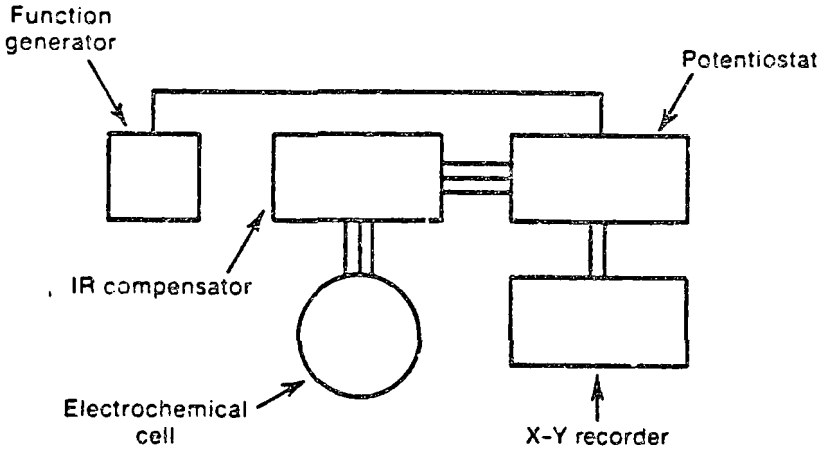

Figure 23. Experimental Apparatus Used in this Study.

Electrochemical Cell

The electrochemical cell used in this study is shown in Figure 24. The cell itself is a 1-liter Pyrex reaction vessel (Pyrex Resin Reaction Kettle, Corning 0947) into which 800 ml of test solution is placed. A 1/4-inch thick plexiglass lid covers the cell with holes drilled to allow insertion of electrodes, thermometer (not shown), and gas dispersion tube (not shown). Two 1-cm^2 platinum foil electrodes were used as counter electrodes. They were held in place by use of rubber cement and Nalgene stoppers. A hole was cut in the bottom of a hollow Nalgene stopper just large enough for the top end of a platinum foil electrode to pass through. The Nalgene stopper was then placed on the electrode and fixed in place by filling the hollow cavity with rubber cement. The Nalgene stoppers were of appropriate size to fit firmly into the holes drilled in the plexiglass lid. Both platinum foil electrodes were mounted in this way. A saturated Calomel reference electrode was used. It was mounted by placing it inside a salt bridge with a water tight seal. The salt bridge (luggin capillary) was held in its proper place in the cell by use of a Nalgene stopper assembly similar to that used for the counter electrodes. The salt bridge is then filled with test solution and its tip placed close to the face of the working electrode. The working electrode

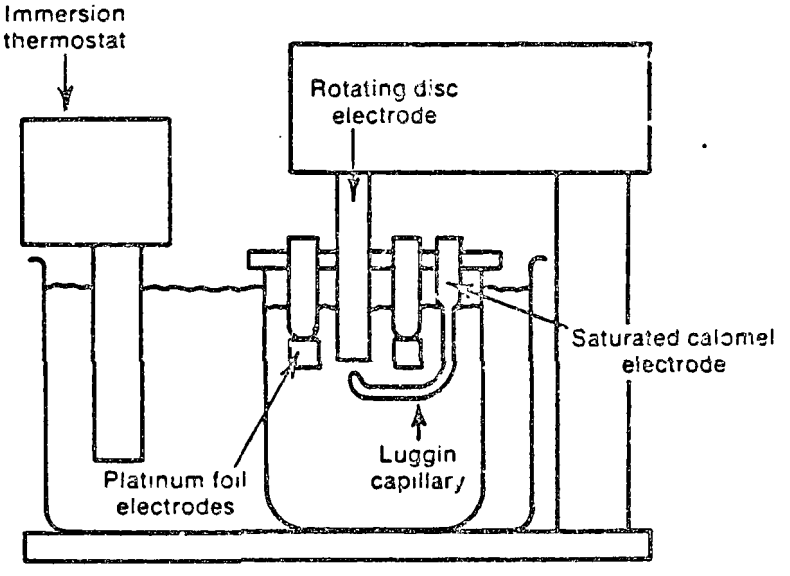

Figure 24. Electrochemical Cell used in This Study.

used was a copper rotating disc electrode, an instrument of adequate sophistication that it warrants the further discussion provided next.

By drilling holes in the plexiglass cell lid and mounting the electrodes and thermometer by use of Nalgene stoppers, the cell could be assembled and disassembled over and over without changing the precise spatial arrangement of electrodes, thus eliminating a possible reduction in reproducibility due to changing cell geometry.

When measurements were being made, temperature control was important. For that reason the entire reaction vessel was immersed in a 10-liter constant temperature water bath controlled by a Thermomix circulator Model 1441 BKU. This allowed temperature control to ±1°C over the range used (5°C to 25°C).

Rotating Disc Electrode

The rotating disc electrode is used to remove solution mass transport limitations on corrosion rate measurements. By rotating the electrode the rate of mass transport of reacting species in solution to the electrode

surface (as well as the rate of mass transport of aqueous phase reaction products away from the electrode surface) in increased. At some rotation speed, the mass transport rate is fast enough that it no longer limits the rate of reaction, thus making a kinetically controlled rate accessible to measurement. The instrument used is a Pine Instruments ASR Rotator with a DDI 15 removable end disc electrode. The apparatus is shown in Figure 25, along with a rotation speed control box (not shown) that allows precise setting of electrode rotation speed up to 10,000 RPM. The electrode is rotated about its vertical axis by the electric motor and drive belt assembly. The electrode is composed of a flat circular copper disc imbedded in a cylindrical teflon housing which rotates at controlled angular speeds. Figure 26 shows the copper disc.

When rotating in solution, a well-defined hydrodynamic flow regime is established. The flow regime becomes radial near the disc, even at low rotation speeds, and sets up a reproducible and laminar hydrodynamic boundary layer of constant thickness across the face of the disc. A diffusion layer is set up within the hydrodynamic boundary layer across which reacting species from the bulk must diffuse to reach the surface of the disc. Mass transport to and from the electrode surface may become limited by molecular diffusion across the diffusion layer, which is normally less than one-tenth the thickness of the hydrodynamic boundary layer. The relationship between diffusion layer thickness, δ_D, and rotating speed, ω, as originally derived by Levich (8) is:

$$\delta_D = 1.61\ D^{1/3}\ \nu^{1/6}\ \omega^{-1/2} \tag{33}$$

Where D is the diffusion coefficient of the electroactive species (cm^2/sec), ν is the kinematic viscosity of the solution (cm^2/sec), and ω is the rotation speed of the disc electrode (radians/sec). A reproducible diffusion layer can only exist within a laminar hydrodynamic boundary layer which has been shown by Schlichting (9) to be reproducible for $Re \leq 3x10^5$. Here Reynolds Number is based on the outer edge velocity of the teflon housing surrounding the copper disc.

$$Re = r^2\omega/\nu \tag{34}$$

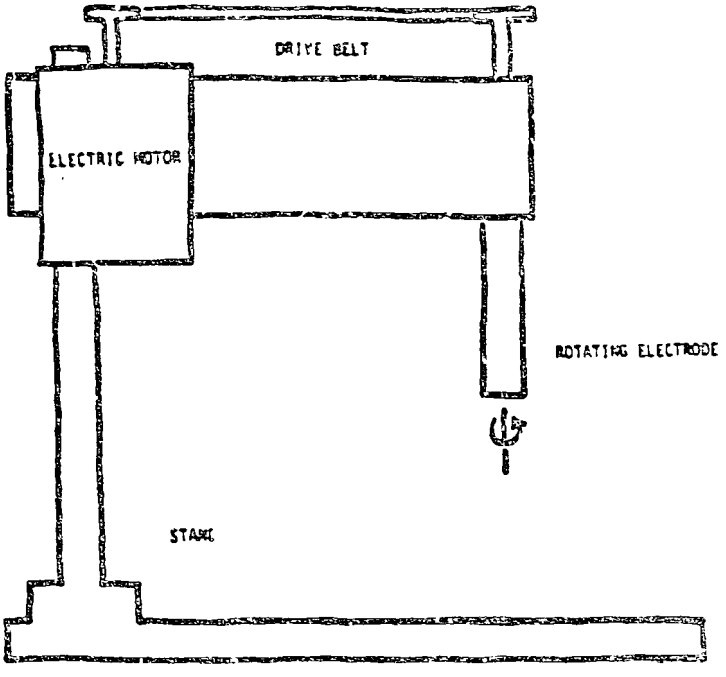

Figure 25. Rotator for Rotating Disc Electrode.

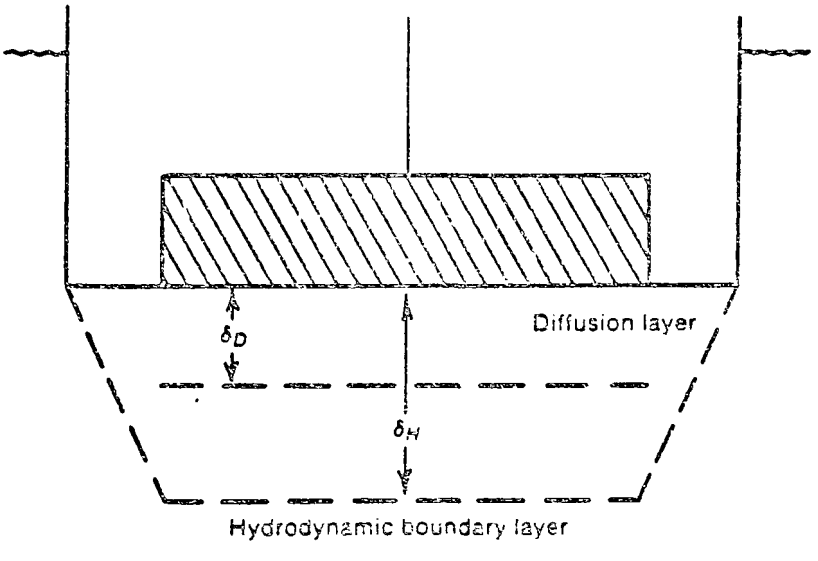

Figure 26. Rotating Copper Disc Electrode.

Although turbulent diffusion layers are sometimes used, and are discussed at length by Pleskov and Filinovskii (10), the upper limit on rotation speed set for a reproducible hydrodynamic boundary layer effectively limits electrode use for mass transport. The rate of solution mass transport is related to the diffusion layer thickness as follows:

$$J = D \frac{\partial c}{\partial x} = \frac{D(C_B - C_S)}{\delta_D} \tag{35}$$

Here C_B is the bulk concentration of diffusing species (moles/cm^3), C_S is the surface concentration of diffusing species (moles/cm^3), and J is the mass transport rate (moles/cm^{2}sec). When equations (33) and (35) are solved simultaneously, the explicit dependence of J on ω is shown.

$$J = \frac{D^{2/3}(C_B - C_S)\,\omega^{1/2}}{1.61\,\nu^{1/6}} \tag{36}$$

As rotation speed, ω, is increased the thickness of the diffusion layer, δ_D, is reduced bringing the bulk concentration of diffusing species closer to the surface of the rotating disc. This increases the concentration gradient and therefore the mass transport rate. For reactions with slow kinetics, such as molecular reduction, solution transport limitations may be eliminated at rotation speeds of less than 1000 RPM.

Potentiostat

The potentiostat is pernaps the most important piece of electronic instrumentation necessary for electrochemical corrosion rate measurements. A variety of commercial instruments is available. All of them provide a means of controlling the electrode potential of the working electrode, some have other built-in conveniences such as a voltmeter for electrode potential measurement and an ammeter for cell current measurement. An Aardvark Model V Standard Laboratory Potentiostast, built by Floyd Bell Associates, Inc. was used in this study. This potentiostat contains multiple scale electrode potential and cell current measuring devices as well as X-Y recorder jacks so that electrode potential and cell current can be plotted directly. An external voltage source input is included also which allows one the option of

either setting and changing electrode potential manually or having the electrode potential changed automatically by an attached external voltage source. Finally, the potentiostat contains shielded inputs for connection to each of the electrodes in the cell.

Function Generator

A function generator is used as an external voltage source to control the time rate of change of electrode potential of the working electrode. The instrument used in this study is an Aardvark Model Scan-3 Electronic Potential Scanner manufactured by Floyd Bell Associates, Inc. for use with the Model V Potentiostat. The potential scanner produces an output voltage that changes linearly with respect to time, at a controlled rate of change. This output voltage is applied to the external voltage source input of the potentiostat, which then applies the linear change in voltage with respect to time to the working electrode/solution interface.

IR Compensator

Generation of a polarization curve requires measurement of electrode potential of the working electrode while current is flowing through the cell. As the current flows out of the working electrode (when it is an anode) and passes through solution, a potential drop is generated between the electrode surface and the tip of the salt bridge (reference electrode) due to the resistance of the solution to current flow. Figure 27 shows this situation.

This potential drop is sometimes small and of little consequence, but in low conductivity solutions the solution resistance can be large enough that the IR_{soln} term distorts the measurement of electrode potential even at low cell current values. This extra voltage drop is called the IR drop and it shows up as either a positive or negative error in electrode potential measurement, depending on the direction of flow of cell current (that is whether the working electrode is acting as an anode or a cathode). When IR drop is present the measured potential between the working and reference electrode is:

$$E_{meas} = E + IR_{soln} \tag{21}$$

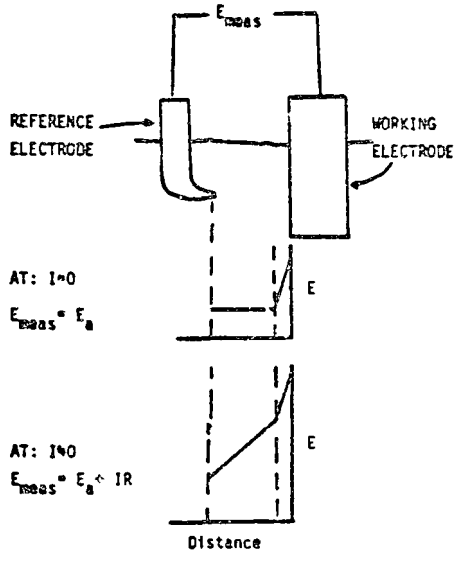

Figure 27. Solution IR Drop.

Where E_{meas} is the measured voltage drop, E, is the working electrode potential, and IR_{soln} is the voltage drop due to solution resistance.

The effect of solution IR drop can be eliminated electronically by use of an IR Compensator. An Aardvark Model IRX IR Compensator, manufactured by Floyd Bell Associates was used in this study. This model is manufactured for use with the Aardvark Model V Potentiostat and is easily inserted into the system between the potentiostat and the cell electrodes. By dialing in a compensating resistance approximately equal in value to the solution resistance between the tip of the salt bridge and the working electrode surface the solution resistance is effectively removed from the measurement of electrode potential. The Model IRX allows insertion of up to 100,000 ohms of compensating resistance, which would handle even distilled water.

Analytical Procedure

In order to ensure reproducibility and be able to compare corrosion rate measurements made at slightly differing solution composition it was necessary to develop a uniform laboratory procedure that would ensure that all experi-

mental runs were conducted as nearly as possible in an identical fashion. This included standard procedures for equipment preparation (electrodes, cell, and test solution), pH and conductivity measurements, final setup of instruments and actual measurement. The details of these standard procedures are outlined in this section.

Equipment Preparation

Each morning it was necessary to turn on the pH meter, IR compensator, and potential scanner one-half hour prior to use for warmup, after which it would operate consistently all day. Other equipment such as electrodes, glassware, and test solution required fresh preparation prior to each experimental run.

Three different copper disc electrodes were used on a rotating basis throughout the study. Each was polished before an experimental run first with Metadi Diamond Polish (6 micron)/deionized water rinse followed by polishing with 0.05 micron-alumina (Buehler Micropolish)/deionized water rinse, and finally cleaned for five minutes in a Branson B-220 Ultrasonic cleaner filled with fresh distilled water/deionized water rinse. This was followed by immediate immersion into test solution for corrosion rate measurement.

Two platinum foil counter electrodes were used in each run. The same two were used each time but were cleaned between runs using a Bon Ami/water solution and Q-tip cotton swabs. This was followed by rinsing three times with distilled deionized water and immersion into the test solution.

The saturated calomel reference electrode required daily check of solution level, uncapping, and insertion into the salt bridge for use throughout the day. The salt bridge was filled with test solution once each day and was merely rinsed with distilled deionized water between runs. At night it was dipped in Nitric Acid wash and stored in deionized rinse water.

The pyrex reaction vessels and plexiglass lid were immersed in the 6N HNO_3 wash overnight, then removed and generously rinsed with distilled water prior to contact with test solution. Normally two reaction vessels were used each day. Between runs, the vessels were rinsed three times with distilled water followed by a final rinse with distilled deionized water. By using two

vessels preparation for the next run could begin prior to completion of the present one.

Test solution composition was varied between runs. A standard mix of synthetic Tolt River water was prepared, 10 liters at a time, using reagent grade chemicals and glass distilled deionized water. The standard mix contained the principal inorganic anions and cations found in Tolt River water, without trace elements and organic constituents. All anions were added as either acids or salts of sodium or calcium. The composition of synthetic Tolt River water is shown in Table 6.

Prior to each run the synthetic Tolt River water had to be temperature equilibrated in the constant temperature water bath to the temperature specified for that run and then the pH was adjusted to its desired level by addition of 0.1 M CaO using an eyedropper.

Table 6
Synthetic Tolt Composition

Species	Concentration Range in Tolt River	Synthetic Tolt Concentration
HCO_3^-	1.4-4.5 mg/l as $CaCO_3$	2.47
Cl^-	1.8-2.6 mg/l	2.49
F^-	0-1.01 mg/l	0.95
$SO_4^=$	1.95	1.94
SiO_2	4.20	4.20
pH	6.0-6.3	6.3
k	25 μmhos/cm	18 μmhos/cm

pH And Temperature Measurement

pH and conductivity measurements were made on the test solution prior to and following each test run. On occasion pH was followed continuously throughout a run. pH was measured with a Metrohm/ Brinkman Model: pH-104

Digital pH meter using a Beckman glass pH electrode with a Beckman, Altex, ceramic junction, Silver/Silver Chloride reference electrode. The pH meter was normally calibrated at least once daily at the temperature at which experimental runs were to be made. Calibration at pH = 6.86 was found to be adequate since most measurements were made between $6.0 \leq pH \leq 9.0$. The test solution was stirred during pH measurement and a response time of roughly 10 minutes was found necessary for stabilization of pH in low conductivity water.

Conductivity was measured with a Barnsted Conductivity Bridge Model PM-70CB, using a Barnsted Model E3421 conductivity cell with a 0.1 cell constant. This cell with its electrodes was directly immersible in the test solution and completely self-contained. The instrument required little calibration or maintenance, just a rinsing of the cell electrodes with distilled deionized water prior to and following each use. Between uses the cell was immersed in distilled deionized water which was changed daily. The instrument response time was fairly rapid except at low conductivities (below approximately 30 μmhos/cm) when 8-10 minutes was needed for stabilization.

Final Setup And Measurement

When preparation of the electrodes, cell, and test solution is complete along with pH and conductivity measurements on the test solution, the electrochemical cell is then assembled by placing the electrodes in the test solution and hooking up the shielded electronic leads that run between the electrodes and the potentiostat. A reducing potential (approx. 200 mv below E_{cor}) is placed on the working electrode to prevent any oxidation from occurring. The X-Y recorder is zeroed and calibrated and appropriate IR compensation is dialed in for the upcoming test run. The potential scanner, set at the appropriate scan rate, is then turned on and the voltage scan begins. The electrode potential of the working electrode is then followed, as it changes with respect to time, on the X-Y recorder which keeps a plot of electrode potential and the corresponding cell current. The potential scanner sweeps the electrode potential of the working electrode in a positive direction through E_{cor} and on to a value approximately 150 mv positive of E_{cor}. The magnitude of the cell current starts off negative indicating that a net reduction reaction is occuring at the working electrode. Gradually

this current is reduced to zero as the potential is swept through the corrosion potential. It then increases in the positive direction as the oxidation half cell takes over at potential values more positive than E_{cor}. From this plot, the corrosion rate is calculated which corresponds to the composition of the test solution used in that run. By varying the concentration of a desired solution parameter and making corrosion rate determinations at each concentration one may determine quantitatively the effect of that parameter on the corrosion rate.

Sources of Error in Corrosion Rate Measurement

Each of the following effects could significantly impact the accuracy or reproducibility of measured corrosion rates:

1) interfering reactions;
2) stability of environmental conditions;
3) calibration of instrumentation; and
4) appproximations involved in corrosion rate calculation

When corrosion rates are determined from polarization curves using the method of Barnartt an assumption that the measured cell current contains contributions from only the anodic and cathodic half-cells of the corrosion rate is implied. When other redox couples are present in solution and reactive within the 200-400 MV range of swept electrode potential they may contribute to the overall cell current causing the shape of the polarization curve to depart somewhat from that predicted by the Stern-Geary model. Minor interferences reduce the accuracy of the corrosion rate calculated from the distorted polarization curve. Minor interferences can distort the shape of the polarization curve to the extent that it is impossible to calculate a corrosion rate estimate. This source of error is minimized by using solutions of known composition and impurity level.

Variation of system properties during the course of a measurement is another possible source of error in corrosion rate determination. The principal environmental variables in this research were temperature, solution pH, and diffusion layer thickness. Temperature was maintained at a constant value by use of the immersion thermostat and water bath configuration described earlier. It was continuously monitored throughout each run and

possible deviations due to heats of reaction were negligible. Temperature was at all times maintained within ±1°C of its prescribed value.

Constant solution pH could be maintained throughout a run only when the solution buffer capacity was adequate to neutralize the amount of hydroxyl ion produced during the course of a measurement.

In general, pH variation throughout a run was less than approximatley 0.3 pH units, despite the low alkalinity level of synthetic Tolt River water. Largest deviations occurred in runs taken under kinetic rate control at 25°C in the range $7.0 \leq pH \leq 8.5$ where the variations sometimes exceeded 1.0 pH unit. When this occurred, additional alkalinity in the form of bicarbonate was added (approx. 10 mg/ℓ as $CaCO_3$) and the measurement was remade.

Diffusion layer thickness was well-defined and stabilized in measurements made under rate control by interfacial reaction kinetics and oxide film growth by rotating the rotating disc electrode at 3000 RPM for each run. Under conditions of stagnant diffusion, diffusion layer thickness was less well defined but data shown later was very reproducible.

Improper calibrations of electronic instrumentation is an obvious source of error. During the course of this study it was found that the critical calibration was that of the zero point of current on the X-Y recorder. Even a small offset between an i = 0 reading on the microammeter (in the potentiostat) and that on the X-Y recorder can cause a large distortion in the shape of the polarization curve. Similar offsets in measurement of the zero of electrode potential are not nearly so critical in effecting corrosion rate values. These errors were minimized by offset calibration of the X-Y recorder before each run.

The final source of error discussed here involves the corrosion rate calculation itself. Using the method of Barnartt a measured polarization curve is evaluated as through it conformed exactly to the exponential of the Stern-Geary model. Although this model represents a simplified version of the corrosion process, for most polarization curves it adequately defines the shape of the curve. The numerical method developed by Barnartt then gives a precise and accurate value. Under these conditions the calculated corrosion rate is in theory independent of the size of ΔE used in the calculation. Problems with this method arise when the polarization curve,

for whatever reason, doesn't quite fit the Stern-Geary form. Under kinetic control, I_{cor} can be calculated from the following expression:

$$I_{cor} = \frac{I_1}{\left[\left|\frac{I_2}{I_1}\right|^2 - 4.0\left|\frac{I_2}{I_3}\right|^{1/2}\right]^{1/2} A}$$

where the values of I_1, I_2, and I_3 depend on the size of ΔE chosen. When the measured curve fits the model well the same I_{cor} value is calculated over a wide range of choices of ΔE. When the curve does not fit the model well, it may still be possible to calculate reasonable corrosion rate values but care must be taken in the choice of ΔE. A value too large or too small may cause the denominator in the above relationship to approach zero, thereby causing the calculated corrosion rate to approach infinity. Figure 28 shows a plot of I_{cor} values calculated from the same polarization curve but using differing ΔE values. A choice of $\Delta E < 20$ MV drives the corrosion rate value calculated from the model toward infinity. Likewise a choice of $\Delta E > 32$ does the same thing. Reasonable values must be chosen from within the range $20 \leq \Delta E \leq 32$. Calculated corrosion rates reported in the following chapter were made largely using a $\Delta E = 30$ MV since I_{cor} was approximately constant with respect to ΔE at that value.

The overall reproducibility of these measurements was quite good when the four possible sources of error mentioned above were accounted for. Table 7 shows the results of six runs under identical conditions of temperature, pH, and δ_D. A standard deviation of approximately 8% of the measured value gives a good indication of the high degree of reproducibility possible using this method.

WEIGHT LOSS TESTING

Standard weight loss coupon tests were run in addition to the electrochemical tests. The idea was to measure the corrosion rate of copper in synthetic Tolt River water at specified pH, temperature, and flow conditions by both methods, then to compare the quantitative results as well as the relative facility with which each test could be run. The results, The laboratory setup and procedure for conducting the weight loss tests along

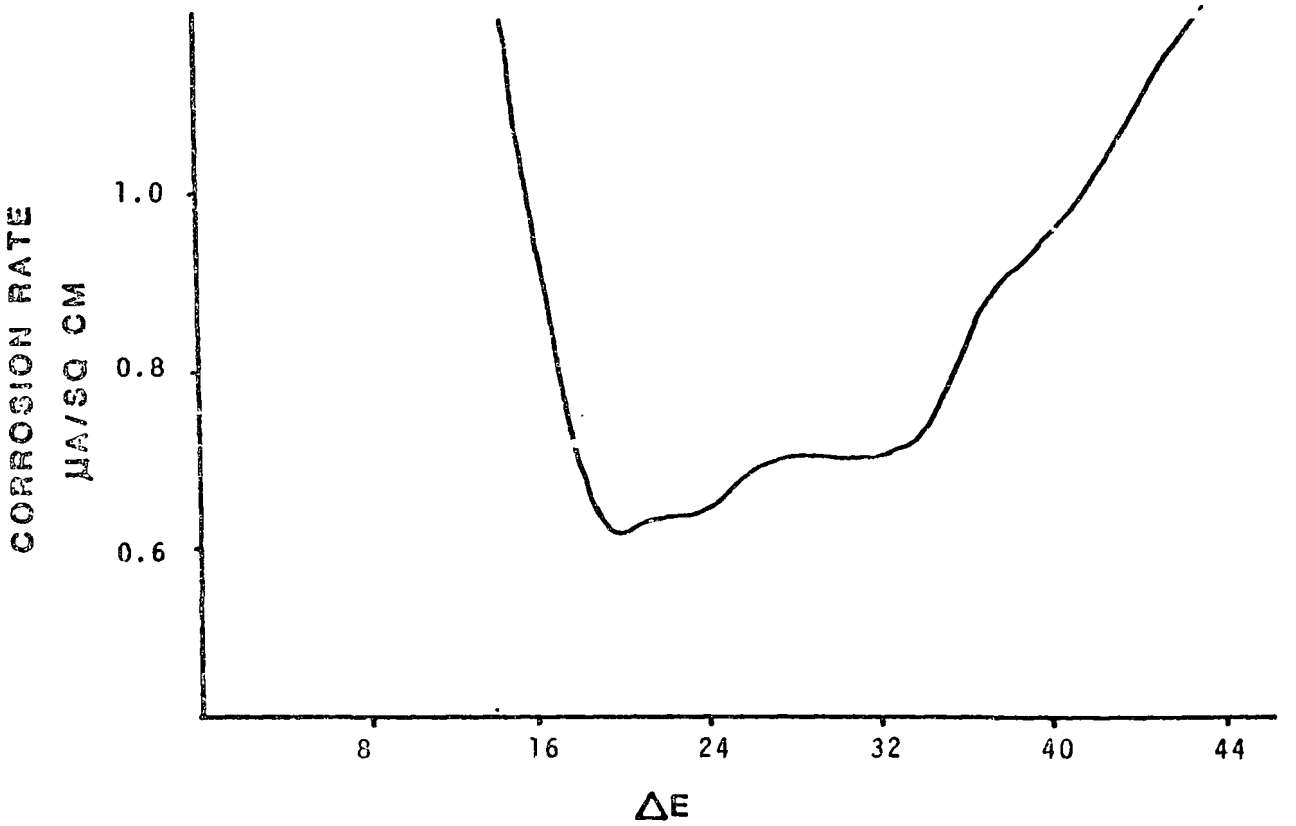

Figure 28. Variability in Three-Point Method.

Table 7
Corrosion Rate of Copper in Synthetic Tolt River Water
Electrochemical Measurements

Run No.	Corrosion Rate ($\mu A/cm^2$)	Corrosion Rate (MPY)
1	0.51	0.23
2	0.55	0.25
3	0.56	0.26
4	0.48	0.22
5	0.55	0.25
6	0.48	0.24
MEAN	0.52	0.24
STD. DEV.	± 0.04	± 0.02

with the method used for calculating corrosion rates will be discussed in this section.

Laboratory Setup and Procedure

Detailed guidelines are available for conducting weight loss coupon tests. The laboratory setup and procedures used in this research are similar to those outlined in NACE Standard TM-01-69 (1976 Revision) entitled "Laboratory Corrosion Testing of Metals for the Process Industries" (11) and ANSI/ASTM G1-72 (Reapproved 1979) entitled "Standard Recommended Practice for Preparing, Cleaning, and Evaluating Corrosion Test Specimens" (12). The tests consisted of preparing and weighing copper test specimens, immersing them in synthetic Tolt River water for a controlled time period, removing the corrosion products and reweighing. The corrosion rate was then calculated from the difference in mass due to formation of corrosion products during the immersion period.

Copper specimens were made from the same stock of electrolytic grade, 3/8 inch diameter, copper rod that was used to make the disc electrodes

mentioned earlier by segmenting the rod into discs. Hole were drilled in the center of each disc for purposes of suspending the specimen in the water. Each specimen was individually suspended in a test tube filled with synthetic Tolt River water. Figure 29 shows the details of how this was done. In all, nine specimens were used. Test tubes containing the specimens were placed in a test tube rack and lowered into a constant temperature water bath which ran continuously throughout the testing period, keeping the temperature of the test solution at 25°C. Figure 30 shows how this was done.

The teflon string suspending the copper specimens was tied to the Nalgene stoppers through small holes in the bottom of the stoppers. The holes were small enough to effectively keep the water in the constant temperature bath from splashing into the test tubes and contaminating the test water. Although small, the holes did allow air flow in and out of the test tube so that reduced levels of O_2 in the test water were avoided. The test water was changed daily by filling a clean test tube with fresh water and then transferring the coupon, which was still attached to the nalgene stopper by the teflon string, to the new test tube. This was a simple process which did not require touching the corroding copper specimens, since transfer from one test tube to another was made by holding the nalgene stopper, and involved less than a 10-second contact time between the copper coupon and the ambient air. Synthetic Tolt water used for replacement was prepared, as described earlier, in 10-liter volumes from reagent grade chemicals and distilled deionized water. New batches were made up as needed which turned out to be roughly every 3 to 5 days. Each specimen was identified by a number on its attached nalgene stopper and its date of immersion was recorded. At least 2 and normally 3 specimens were immersed for the same test period as replicates.

Prior to immersion each specimen was abraded with No. 240 and then No. 600 grade silicon carbide sand paper which removed a substantial layer of outer metal. This was done to reduce surface roughness as well as to eliminate variations in metallic surface conditions between specimens at the time of initial immersion. Specimen dimensions were measured with a micrometer caliper from which surface area calculations were made. This was followed by scrubbing the specimens with Bon Ami (a nonchlorinated and mild scouring powder) and a firm bristled tooth brush, rinsing with distilled water, air

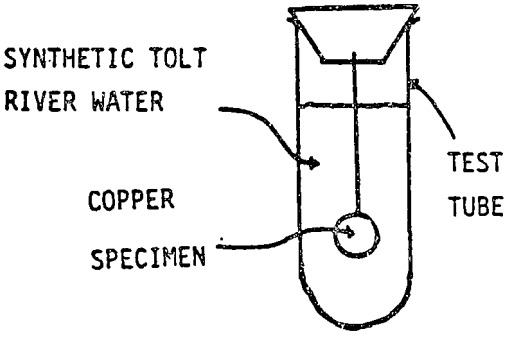

Figure 29. Test Tube Containing Weight Loss Coupon

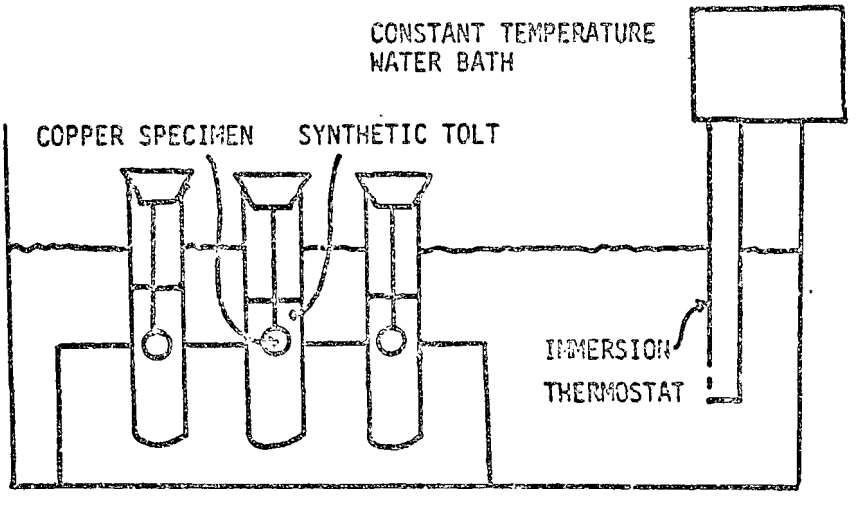

Figure 30. Weight Loss Test Apparatus.

drying, and weighing on a Metler Analytical Balance (Type H6). Specimen number, weight (to nearest 0.1 mg), surface area, and date/time of immersion were then recorded for later use.

When a specimen had been immersed for the desired time period it was removed from the test solution and scrubbed to remove corrosion products (using cold water, Bon Ami, and a strong bristled brush). The corrosion products formed on the copper specimens were principally a dull rust color, which corresponds to hydrated cuprous oxide (13). Occasionally, patches of black cupric oxide are observed. As the oxide films are removed from the copper, its surface becomes very bright. This brilliance was used as an indication that corrosion products had been successfully removed. Specimens are then rinsed, air dried, and weighed on an analytical balance.

Calculating Corrosion Rate from Weight Loss Data

The rate of uniform corrosion can be calculated from weight loss data for each coupon by use of the following relationship:

$$R_{(MPY)} = \frac{(\text{Wt. loss})\ \ 534}{(\text{Area})(\text{Time})(\text{Metal Density})} \tag{22}$$

Here $R_{(MPY)}$ is the corrosion rate in mils/year, 534 is a unit conversion factor, weight loss is in milligrams, area is in square centimeters, immersion time is in hours, and metal density is in grams/cm^3. The density of copper is 8.91 gm/cm^3.

Since coupons were immersed for varying time periods, the corrosion rate was determined by plotting weight loss versus time for all coupons, the slope of which is the corrosion rate. A weight loss parameter, B, was calculated for each coupon as follows:

$$B = \frac{(\text{Wt. Loss})\ \ 534}{(\text{Area})(8.91\ \text{gm/cm}^3)} \tag{23}$$

When B is plotted versus immersion time (hours) and a straight line is regressed between the data points, the slope of that line is the corrosion rate in mils/year.

Results of the weight loss tests are plotted in Figure 31 in the fashion described above. Data shown run from an immersion time of one to four

months. The slope of the regression line is shown to be 0.23 MPY, a value that compares quite favorably to the electrochemical corrosion rate measurements of Table 7. Those measurements were made under identical conditions and produced a value of 0.24 MPY. Based on this comparison it was concluded that the rate of the corrosion reaction was being measured correctly by the electrochemical system. Coupons immersed for periods longer than four months showed signs of localized corrosion, pitting, and were not very reproducible. Measured rates were slightly higher ranging from 0.23 MPY to just above 0.30 MPY for immersion times of seven months.

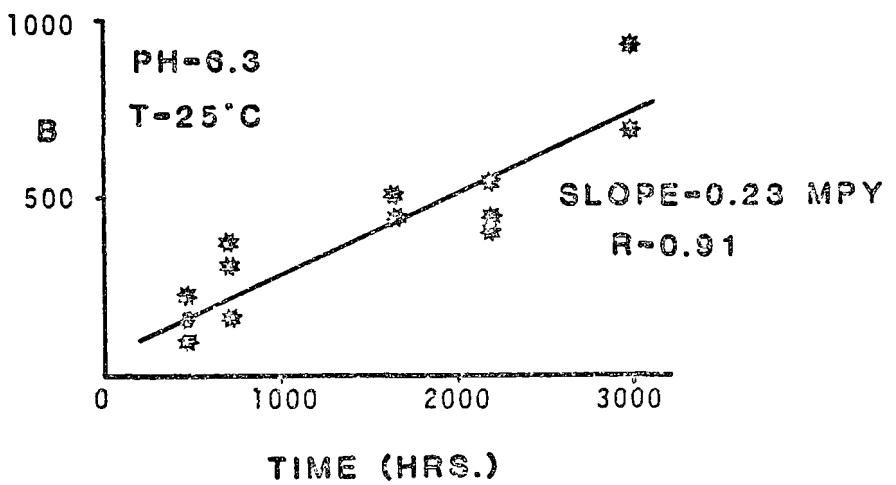

Figure 31. Weight Loss Test Results.

SECTION 6

EXPERIMENTAL RESULTS AND ANALYSIS

INTRODUCTION

The results of experiments designed to be under rate control by each of the component rate processes are presented in this chapter. Whenever possible these results are compared to theoretical models developed in Section 4 which describe the variations of each component process with respect to pH and temperature. This chapter begins with an explanation of methods of analysis developed for use in heterogeneous systems. A presentation and analysis of data taken under rate control by interfacial reaction kinetics follows with development of quantitative rate expressions. Presentation and analysis of data taken under rate control by oxide film growth and under rate control by solution mass transport follow. Appropriate rate expressions and possible mechanisms are developed. The chapter closes with a summary of findings and conclusions.

Many of the experiments reported on in this chapter were designed to completely eliminate the effects of solution mass transport and allow independent quantification of the underlying rate controlling process which could be either an interfacial reaction or oxide film growth depending on the conditions at the electrode surface. Design of these experiments was based on the assumption that the rate controlling diffusing species was molecular oxygen, whose mass transport rate is increased significantly even at low RPM. It was later determined, as is described below, that the rate controlling diffusing species is not O_2 but a reaction product which must diffuse away from the electrode surface. In theory, that species could be OH^-, Cu^{2+}, some $Cu(OH)_n^{2-n}$ complex, or a combination of some or all of those species. Since the stagnant diffusion data, presented later on, were fit quite well using OH^- as the diffusing species, the analysis that follows presumes that OH^- is the rate controlling diffusing species.

Experimental elimination of solution mass transport effects is more complicated when the diffusion species is a reaction product. Under such conditions the effect of diffusion on the overall rate may persist, even at high RPM making it more difficult to quantify the pH and temperature dependence of the underlying rate process. Special analytical methods are necessary to evaluate such data.

A method of analysis is presented here that allows quantification of rate data under conditions where an underlying rate process and solution mass transport both affect the overall rate. For the data presented here, both the rate of the underlying process and the rate of mass transport are dependent upon the interfacial OH^- concentration.

The rate of hydroxyl ion, $[OH^-]$, diffusing away from the electrode into bulk solution. It can be written as follows:

$$R_{MT} = \frac{D_{OH}}{\delta_D} (C_S - C_B) \tag{1}$$

Here C_s and C_B are the surface and bulk hydroxyl ion concentrations in (moles/cm^3), D_{OH} is the hydroxyl ion diffusion coefficient (cm^2/sec), δ_D is the diffusion layer thickness in cm, and R_{MT} is the rate of mass transport of OH^- away from the electrode surface in units of moles/ cm^2 sec. It is convenient to write the rate expression for the underlying process in terms of C_s as well, since C_s is related directly to pH by the ion product of water, K_w.

$$R_K = a\, C_s^b \tag{2}$$

Here, a and b are numerical constants that describe the dependence of the rate of the underlying process on hydroxyl ion concentration. R_k has the units of moles/cm^2sec, b is unitless, and a has the units necessary to make the relationship dimensionally consistent,

$$\left(\frac{(\text{Moles}^{1-b})(\text{cm}^{1+b})}{\text{sec}}\right) .$$

Under joint rate control the two rates are equal to the rate of the overall process, R:

$$R = R_{mt} = R_k$$

Equating the rate expressions produces the following:

$$a\ C_s^b = \frac{D_{OH}}{\delta_D}\ (C_S - C_B) \tag{3}$$

where a and b are the coefficients to be determined and δ_D and C_B are known. Methods of analysis for such problems have been developed by Frank-Kamenetskii (1) and elaborated by Levich (2) and Pleskov and Filinovskii (3) for use in electrochemical systems. Their method is developed by first defining a dimensionless concentration, C*, where:

$$C^* = \frac{C_S}{C_B}$$

Equation 3 can then be written in terms of C* by multiplying each side by C_B^{-b} and defining μ, such that:

$$\mu = \frac{a\delta_D}{D_{OH}}\ C_B^{b-1} \tag{4}$$

which yields the expression:

$$\mu C^{*b} = (C^* - 1) \tag{5}$$

In logarithmic form this becomes a linear relationship

$$\log \mu + b \log C^* = \log (C^* - 1) \tag{6}$$

with slope b and intercept, log μ. Figure 32 shows a plot of log C* versus log (C* -1). The three regions of constant slope (I, II, and III) are of physical significance in that they correspond to conditions of complete kinetic rate control, mixed kinetic and mass transport rate control, and complete diffusion control.

In Region I, log $C^* \cong 0$ so $C^* \cong 1$ and:

$$C_S \cong C_B$$

The process therefore proceeds at a rate defined by the rate of the underlying rate process with a rate expression of the form:

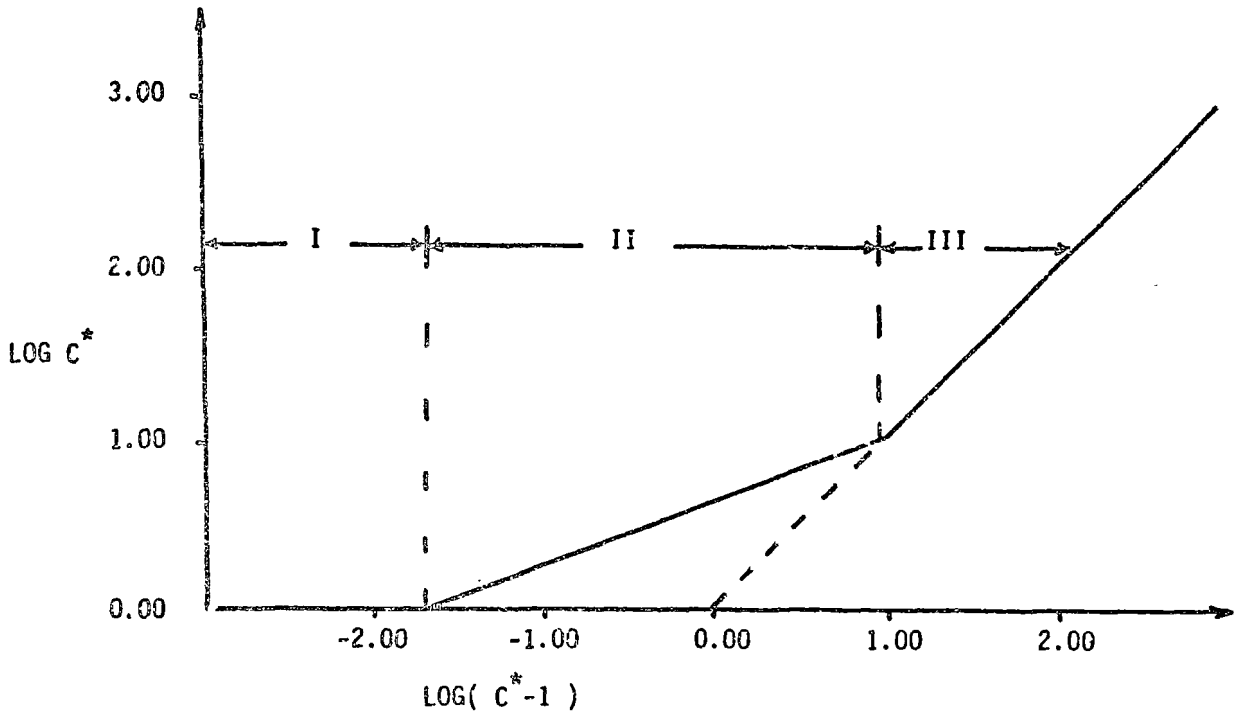

Figure 32. Frank-Kamenetskii plot for data taken in heterogeneous systems.

$$R = a\ C_s^b = a\ C_B^b$$

Data points that fall in this region are then analyzed by plotting log I_{cor} v. pH_B, since:

$$R = \frac{I(10^{-6})}{nF}$$

and: $$C_B = 10^{-3}\ K_w\ 10^{pH_B}$$

then: $$I = [(\frac{nFa}{10^{-6}})(10^{-3}\ K_w)^b] + 10^{b\ pH_B}$$

$$\log I = \log[\frac{nFa}{10^{-6}}(10^{-3}\ K_w)^b] + b\ pH_B$$

Regression of log I values on their corresponding pH_B values allows determination of b, as the slope and

$$\log[\frac{nFa}{10^{-6}}(10^{-3}\ K_w)^b]$$

as the intercept. From this value of the intercept, a can be calculated. When the underlying rate controlling process is an interfacial reaction the regression parameter, a, is an Arrhenius type rate constant which is temperature dependent:

$$a = A\ \exp(-\frac{E_A}{R_G T})$$

E_a is the activation energy for the rate controlling step of the surface reaction in (calories/mole °K), A is called the frequency factor, and R_G is the universal gas constant. When values of a are known at several temperatures, ln a can be plotted versus 1/T ($°K^{-1}$) since:

$$\ln a = \ln A - (\frac{E_A}{R_G})\ \frac{1}{T}$$

Regression yields the value of ln A as an intercept and $-E_A/R_G$ as the slope.

In region II, the rate of the overall process is jointly controlled by the rate of the underlying process and solution mass transport. That is, log $C^* > 0$ but not large enough to make any simplifying approximations. Determination of a and b is therefore accomplished in a different fashion than in region I. Here both rate processes are at work at rates of equal magnitude:

$$R_{MT} = \frac{D}{\delta_D} (C_S - C_B)$$

so

$$C_S = \frac{\delta_D R_{MT}}{D_{OH}} + C_B)$$

Substituting this relationship for C_S into the rate expression for the underlying rate process we get:

$$R_K = a(C_B + \frac{\delta_D R_{MT}}{D_{OH}})^b$$

Since the overall rate, R, is equal to R_K and R_{MT}. we can write:

$$R = a(C_B + \frac{\delta_D R}{D_{OH}})^b$$

This rate expression is now in a form suitable for determining coefficients, a and b, for the underlying process rate expression from data measured under joint kinetic/mass transport rate control. Taking logarithms, base 10, of both sides of the expression above we get:

$$\log R = \log a + b \log(C_B + \frac{\delta_D R}{D_{OH}})$$

Defining new variables Y and X, and coefficient a' we have:

$$Y = \log R$$

$$X = \log (C_B + \frac{\delta_D R}{D_{OH}})$$

$$a' = \log a$$

and the following linear relationship:

$$Y = a' + bX$$

By transforming each data point into the form of Y and X, we can by linear regression find values for a' and b. From a' we can determine a.

The measured corrosion rate, $I_{cor}(\mu_A/cm^2)$, can be converted into a Y value by noting that:

$$R = \left(\frac{I\ 10^{-6}}{nF}\right)$$

and: $$Y = \log R = \log \left(\frac{I\ 10^{-6}}{nF}\right)$$

Here n is the number of electrons transferred per mole of OH^- produced, n = 1. F is the farraday constant, 96,485 coul/eq, and I is the measured corrosion rate in (μ_A/cm^2).

X can be determined for each data point by noting that:

$$C_B = (10^{-3})\ K_w\ 10^{pH_B}$$

$$\delta_D = \begin{cases} 9.08 \times 10^{-2}\ D^{1/3}\ \nu^{1/6} & \text{(for RDE at 3000 RPM)} \\ 0.5\ (D_{OH}\pi t)^{1/2} & \text{(for Stagnant Diffusion at t = 40 sec.)} \end{cases}$$

and $$X = \log \left[C_B + \frac{\delta_D\ R}{D_{OH}}\right]$$

The values of K_w, D_{OH}, and ν are all temperature dependent but known, so that for a given data point:

$$I_{cor},\ pH_B,\ T$$

corresponding values of X and Y can be calculated. When Y is plotted versus X the slope of the regression line will be constant over a range of data where a single reaction mechanism is operating.

In range III, $C^* >> 1$, so that $C_S >> C_B$ and

$$(C_S - C_B) \cong C_S$$

This corresponds to a situation where the overall rate is completely controlled by diffusion in solution. The appropriate rate expression is then:

$$R = \frac{D}{\delta_D}(C_S - C_B) \cong \frac{DC_S}{\delta_D}$$

Under these conditions C_S generally increases to some steady-state or saturation value (2), which may or may not be related to the value of C_B. C_S becomes independent of C_B when its magnitude is controlled by some other reaction going on in solution, such as precipitation. Under these circumstances the overall rate may be represented as:

$$R = \frac{D\ C_{eq}}{\delta_D}$$

where C_{eq} is a concentration in equilibrium with other species in solution. It may be temperature dependent. A plot of I versus pH_B for data taken under these conditions is a straight line with slope of zero and intercept at:

$$I = \frac{nFD(10^{-6})C_{eq}}{\delta_D}$$

For the case where C_S is dependent upon C_B, a general form relating their values is:

$$C_S = pC_B^b$$

so that the overall rate expression becomes:

$$R = \frac{DPC_B^b}{\delta_D}$$

A plot of log I v. pH_B is now a straight line of the form:

$$\log I = \log\left[\frac{nFD_{OH}\ p(10^{-3}\ K_w)^b}{10^{-6}\ \delta_D}\right] + b\ pH_B$$

where the slope, b, and the intercept,

$$\log \left[\frac{nFD_{OH}\ p(10^{-3}\ K_w)^b}{10^{-6}\delta_D}\right]$$

can be determined by linear regression. The value of p can be determined from the slope and intercept values. The general form of the rate expression for reactions completely diffusion controlled is then:

$$I = \left(\frac{nFD_{OH}\ p(10^{-3}\ K_w)^b}{10^{-6}\ \delta_D}\right)\ 10^{bpH_B}$$

Data falling into region III are then analyzed by plotting log I vs. pH_B and regressing to find b and p. As $b \longrightarrow 0$, $p \longrightarrow C_{eq}$ a limiting case where C_S is independent of C_B.

A recapitulation of the methods necessary for analysis of data falling into regions I, II, and III is given in Table 8. It shows explicitly that analysis of data falling into regions I and III is much simpler than in region II, requiring only a plot of log I versus pH_B, linear regression, and direct calculation of appropriate parameter values. While analysis of data in region II requires calculation of transformed variables X and Y first and then regression. Calculation of appropriate parameter values is complicated in this region when the temperature dependence of data taken under these conditions reflects the joint effects of a changing rate of surface reaction and a changing rate of diffusion in solution.

Initial experimental design was then an attempt to generate data only in regions I and III. Experiments designed to be under rate control by interfacial reaction kinetics should give data in region I, completely free of solution mass transport effects. Experiments designed for rate control by oxide film growth and transport should also give data in region I, free of solution mass transport effects. Experiments designed to be under rate control by stagnant diffusion in solution should then give data in Region III. The extent to which this was successful becomes apparent as the data taken under each type of rate control are examined.

Table 8. Summary of Data Analysis Methodology

REGION I: COMPLETE KINETIC CONTROL

a) Rate Expression: $I = c\ 10^{bpH_B}$

where: $c = (\frac{nFa}{10^{-6}})(10^{-3}\ K_w)^b$, $I = \mu A/cm^2$; $a = A\ \exp(-\frac{Ea}{R_G T})$

b) Form for Regression: (Determine a and b)

$$\log I = \log c_o + b\ PH_B$$

REGION II: MIXED KINETIC/MASS TRANSPORT CONTROL

a) Rate Expression: $I = (\frac{nFa}{10^{-6}})\ C_S^{\ b}$

where C_S is determined from numerical solution of: $aC_S^b = \frac{D_{OH}}{\delta_D}(C_S - C_B)$

b) Form for Regression: $y = a' + bX$ (determine a and b)

where: $y = \log\ (\frac{I\ (10^{-6})}{nF})$

$$x = \log\ [10^{-3}\ K_W\ 10^{pH_B} + \frac{I(10^{-6})\ \delta_D}{nF\ D_{OH}}], \quad a' = \log a$$

REGION III: COMPLETE DIFFUSION CONTROL

a) Rate Expression: $I = (\frac{nFD_{OH}\ P(10^{-3}\ K_w)^b}{10^{-6}\ \delta_D})\ 10^{bpH_B}$

b) Form for Regression: (determine a and b)

$$\log I = \log\ [\frac{nF\ D_{OH}\ P\ (10^{-3}\ K_w)^b}{10^{-6}\ \delta_D}] + b\ pH_B$$

RATE CONTROL BY INTERFACIAL REACTIONS KINETICS

Data presented in this section resulted from experiments designed to measure corrosion rates under the conditions of rate control by interfacial reaction kinetics. It was assumed that by minimizing the influence of the other component rate processes that the dependency of the rate of the controlling interfacial reaction on solution pH and temperature could be determined quantitatively. Experimentally this meant running polarization curves on freshly polished copper electrodes rotated at 3000 RPM. Any oxide film present on the copper surface was effectively removed by polishing the surface, eliminating the influence of solid-state transport through an oxide film on the overall measured rate of corrosion. Rotation of the rotating disc electrode at 3000 RPM substantially decreases the thickness of the diffusion layer for OH^-, H^+, Cu^{2+} and O_2 and thereby reduces the influence of their respective rates of mass transport on the overall rate of the process. So the measured corrosion rate was intended to correspond to the rate at which the rate limiting interfacial reaction is taking place. This could be the metal dissolution, early stage oxide film growth, oxide film dissolution, or molecular oxygen reduction reaction. Rate variations with respect to pH and temperature are then used to compare measured data with theoretical rate expressions.

Data taken in this fashion at 25°C are shown in Table 9. Standard mix synthetic Tolt River water with pH adjustments made by CaO addition was used in each run. Details of the composition of this solution were shown earlier in Section 5. Values of pH and conductivity recorded in Table 9 are an a average of those measured at the start and completion of each run. Corrosion rate values have been calculated from polarization curves by the method of Barnartt. R_Ω is the amount of resistance necessary to compensate for the voltage drop due to solution resistance between the working and reference electrodes. The recorded temperature is that of the solution which was maintained at a constant value throughout each run by use of an immersion thermostat and water bath.

Figure 33, shows a plot of the data in the form of log C^* versus log (C^*-1). Here C^* was calculated in the following fashion:

Table 9. Kinetic Rate Control Data: 25°C

Run	T (°C)	pH	I ($\mu A/cm^2$)	RPM	χ	R_a	log C*	pH_s
1	25	7.88	0.53	3000	16.2	22,000	0.08	7.96
2	25	7.63	0.99	3000	16.3	21,000	0.23	7.87
3	25	8.22	0.68	3000	18.6	19,000	0.05	8.27
4	25	8.37	0.89	3000	19.0	18,000	0.05	8.41
5	25	8.63	0.59	3000	20.8	-	0.02	8.64
6	25	6.25	2.88	3000	15.8	21,000	1.69	7.95
7	25	6.57	1.84	3000	14.7	21,000	1.21	7.77
8	25	6.73	1.44	3000	15.2	21,000	0.96	7.69
9	25	6.35	2.99	3000	14.3	23,000	1.62	7.97
10	25	6.51	1.98	3000	14.7	22,000	1.28	7.80
11	25	6.65	1.64	3000	15.0	22,000	0.83	7.73
12	25	6.24	2.62	3000	13.9	23,000	1.67	7.91
13	25	6.90	1.52	3000	15.5	21,000	0.83	7.73
14	25	6.05	3.35	3000	-	27,000	1.96	8.01
15	25	6.54	1.61	3000	-	25,000	1.18	7.72
16	25	6.39	0.90	3000	-	20,000	0.58	7.57
17	25	7.02	0.96	3000	-	21,000	0.58	7.59
18	25	7.10	0.55	3000	-	26,000	0.37	7.47
19	25	7.33	0.74	3000	-	18,000	0.31	7.64
20	25	7.64	0.70	3000	-	19,000	0.170	7.81
21	25	7.63	1.06	3000	-	16,000	0.24	7.87
22	25	7.66	1.26	3000	-	17,000	0.26	7.97
23	25	7.68	0.66	3000	-	16,000	0.26	7.98

Table 9 - Continued

Run	T (°C)	pH	I ($\mu A/cm^2$)	RPM	χ	R_Ω	log C*	pH_S
24	25	7.76	1.41	3000	-	24,000	0.24	8.00
25	25	7.80	0.64	3000	-	22,000	0.010	7.92
26	25	7.75	0.71	3000	-	17,700	0.14	7.89
27	25	7.89	1.17	3000	-	10,500	0.16	8.05
28	25	7.92	0.78	3000	-	19,000	0.11	8.03
29	25	8.00	1.04	3000	-	23,000	0.12	8.13
30	25	9.19	0.42	3000	-	14,000	0.00	9.19
31	25	9.25	0.51	3000	-	12,000	0.00	9.25
32	25	9.37	0.56	3000	-	11,000	0.00	9.37
33	25	9.87	0.35	3000	-	7,700	0.00	9.87
34	25	9.91	0.23	3000	-	8,100	0.00	9.91
35	25	0.95	0.29	3000	-	7,000	0.00	9.96
36	25	7.76	1.11	3000	-	21,000	0.26	8.00
37	25	8.80	0.58	3000	20.9	16,000	0.01	8.80
38	25	9.15	0.48	3000	20.7	16,000	0.01	9.15

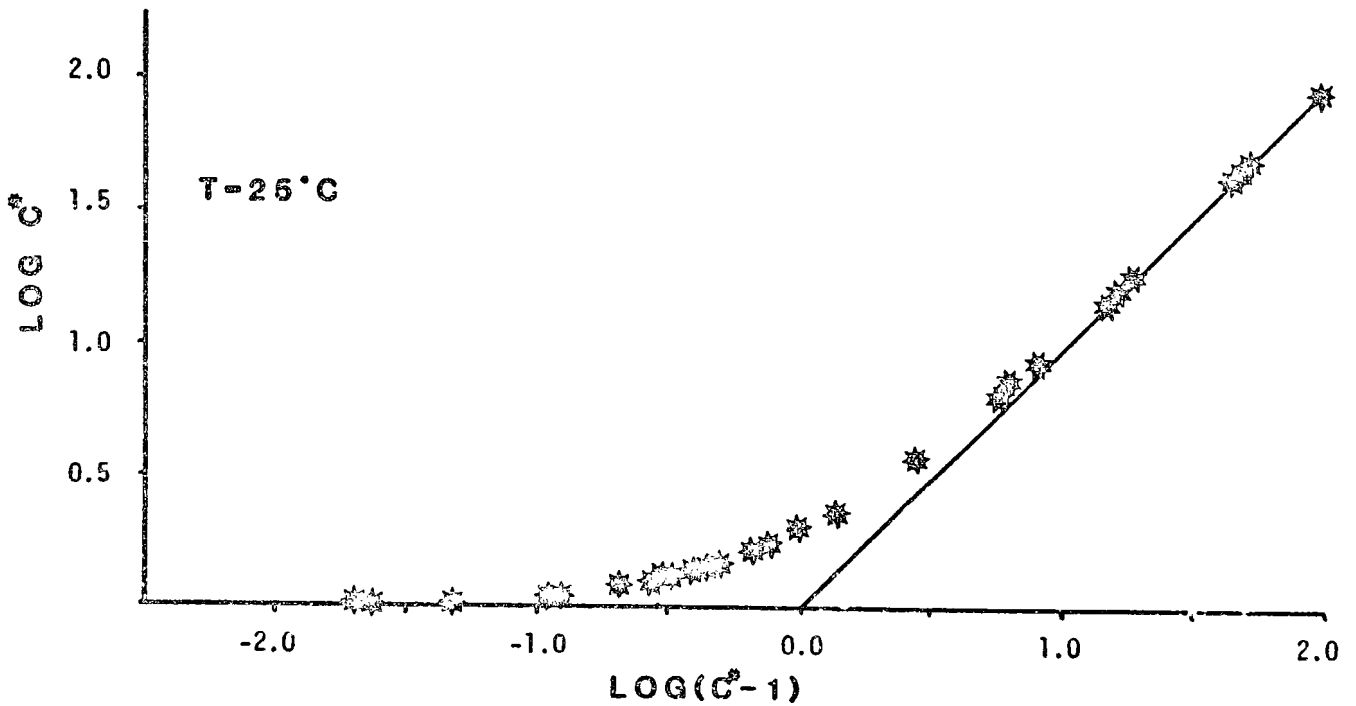

Figure 33. Frank-Kamenetskii plot of kinetic data at 25°C.

$$I(\mu A/cm^2) = \frac{nF\ D_{OH}}{10^{-6}\delta_D}\ (C_S - C_B)$$

so that: $$C^* = (\frac{C_S}{CB}) = (1 + \frac{10^{-3}\delta_D\ I\ 10^{-pH_B}}{nF\ D_{OH}\ K_W})$$

Each data point, (I, pH_B), has been determined under conditions of controlled temperature and diffusion layer thickness, so that C^* may be calculated and the plot of Figure 33 produced.

The plot of data points in Figure 33 is quite different than that expected based on the experimental design. That is, these data were expected to be either completely or nearly completely controlled by the rates of interfacial reaction which means that all data points should fall along or close to the log $C^* = 0$ axis with log $(C^* - 1) \leq -0.8$. In fact, only a few of the data points actually conformed to this expectation. Most fall into regions II and III indicating mixed kinetic/solution mass transport rate control and complete solution mass transport rate control respectively. It is interesting to note that each of these regions corresponds to a bulk solution pH range:

Region I: $8.63 < PH_B < 9.96$
Region II: $7.02 < pH_B < 8.63$
Region III: $6.05 < pH_B < 7.02$

indicating that as the solution pH is increased from an initial value of 6.05 to a value greater than 7.02 rate control of the overall process changes from complete diffusion control (Region I) to mixed rate control. When the pH is raised above pH = 8.63 the overall process is controlled by the rate of the underlying rate process. Each data point must then be evaluated in terms of whether it falls into regions I, II, or III and then subjected to the type of data analysis appropriate for that region.

Data taken at 15°C are shown in Table 10. The plot of Figure 34 shows that most data taken at this temperature fall into region III, with a few data points in region II but none in region I. Here the region of rate

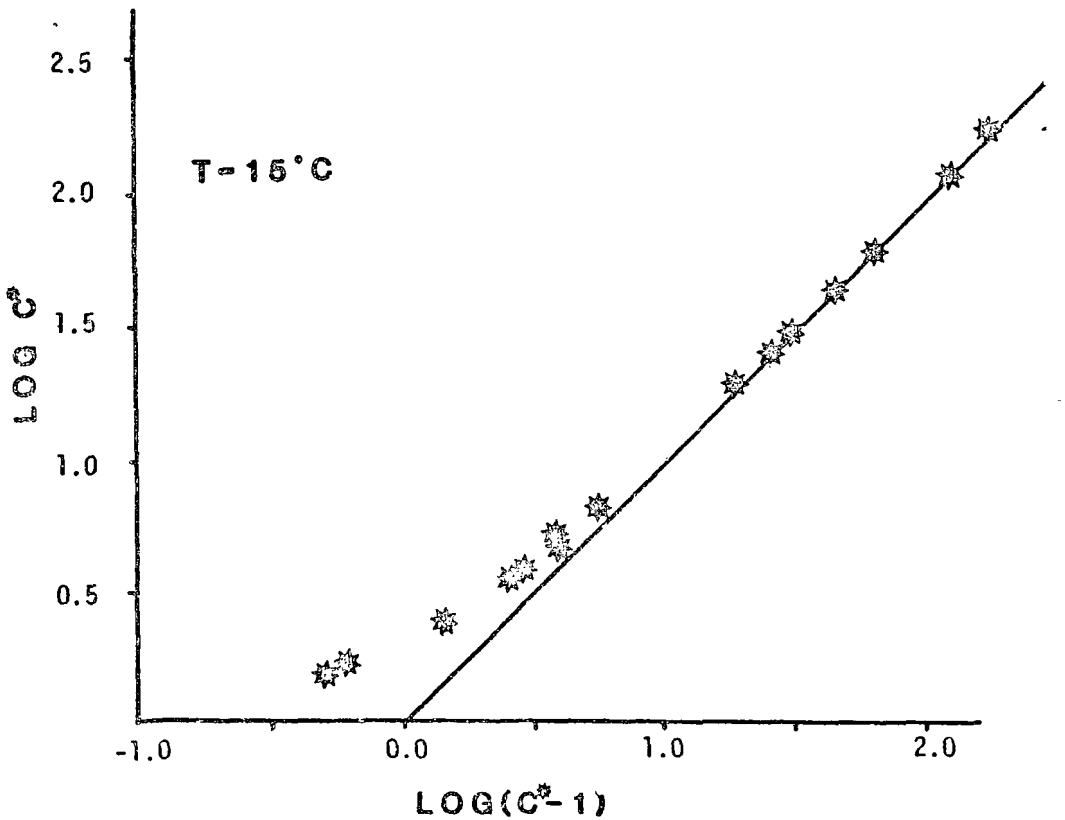

Figure 34. Frank-Kamenetskii plot of kinetic data at 15°C.

Table 10. Kinetic Control Data: 15°C

Run	T (°C)	pH	I ($\mu A/cm^2$)	RPM	k	R_Ω	log C*	pH_S
1	15	6.22	2.27	3000	10.1	33,000	2.07	8.19
2	15	6.27	3.37	3000	12.1	25,000	2.19	8.22
3	15	6.52	2.37	3000	13.6	22,000	1.79	8.31
4	15	6.86	2.49	3000	13.4	24,000	1.48	8.34
5	15	6.93	1.81	3000	12.0	27,000	1.28	8.21
6	15	7.42	1.69	3000	14.3	26,000	0.81	8.23
7	15	6.65	1.33	3000	12.7	27,000	1.42	8.07
8	15	7.54	1.61	3000	13.3	25,000	0.69	8.23
9	15	6.50	1.59	3000	11.6	26,000	1.64	8.14
10	15	6.04	2.23	3000	11.7	26,000	2.24	8.28
11	15	7.52	1.43	3000	11.8	28,000	0.67	8.19
12	15	8.00	1.62	3000	12.9	25,000	0.38	8.38
13	15	8.10	0.87	3000	13.6	20,000	0.20	8.30
14	15	7.52	0.95	3000	13.0	25,000	0.54	8.06
15	15	7.45	0.97	3000	12.5	28,000	0.59	8.04
16	15	8.19	0.92	3000	15.4	20,000	0.18	8.37
17	15	6.05	1.54	3000	10.0	33,000	2.07	8.12

Table 11. Kinetic Rate Control Data: $5^{o}C$.

Run	T (°C)	pH	I ($\mu A/cm^2$)	RPM	κ	R_Ω	log C*	pH_S
1	5	7.86	1.28	3000	12.2	25,000	0.77	8.63
2	5	6.30	1.40	3000	10.0	34,000	2.29	8.59
3	5	6.32	3.71	3000	10.7	32,000	2.69	9.01
4	5	6.37	2.58	3000	10.8	31,000	2.48	8.85
5	5	7.83	1.09	3000	12.3	27,000	0.74	8.57
6	5	8.19	0.63	3000	14.3	21,000	0.33	8.52
7	5	8.27	0.75	3000	12.8	24,000	0.33	8.60
8	5	7.14	0.84	3000	12.1	25,000	1.25	8.39
9	5	7.18	1.04	3000	10.5	28,000	1.30	8.48
10	5	6.79	1.17	3000	10.5	28,000	1.73	8.52

control by solution mass transport encompasses a pH_B range of 6.0 to roughly > 7.6, extending diffusion rate control to higher pH values than at 25°C.

Data taken at 5°C are presented in Table 11 and are plotted in Figure 35 in the form of log C^* versus log (C^*-1). This plot shows that nearly every data point at this temperature falls in region III, the region of complete rate control by diffusion in solution. The upper limit on pH_B for diffusion control is roughly 8.0 at this temperature, a change that corresponds to the trend noted in comparing data at 25°C and 15°C.

Analysis of Data in Region I

So, despite the initial intention to have all the data fall into region I, experimental results show that only a few data points, measured at 25°C and at solution pH values greater than 8.6, actually correspond to conditions of complete rate control by interfacial reaction kinetics. As will be shown later on in this chapter, this is presumed due to the persistent and unexpected influence of diffusion of hydroxyl ion, OH^-, away from the corroding metal surface, as a reaction product of the molecular oxygen reduction reaction. This mass transport effect is especially pronounced in poorly buffered solutions where the bulk concentration of OH^- is low (pH_B < 8.0) and only starts to die out at higher pH values where the amount of OH^- produced by the corrosion reaction is negligibly small in comparison to the OH^- concentration in solution. Region I data, therefore only exist at high pH. Corrosion rates measured at pH values high enough to be included here were only measured at 25°C.

Region I data are analyzed by plotting log I versus pH_B with the slope and intercept determined by linear regression. Data points in region I are shown in Table 12 and plotted in Figure 36. The solid line on the plot corresponds to the regressed linear relationship between log I and pH_B.

Regression of log I on pH_B gives the following rate expression:

$$\log I = -3.600 - 0.300\ pH_B$$

with: $r^2 = 0.907$

which can be written in the form:

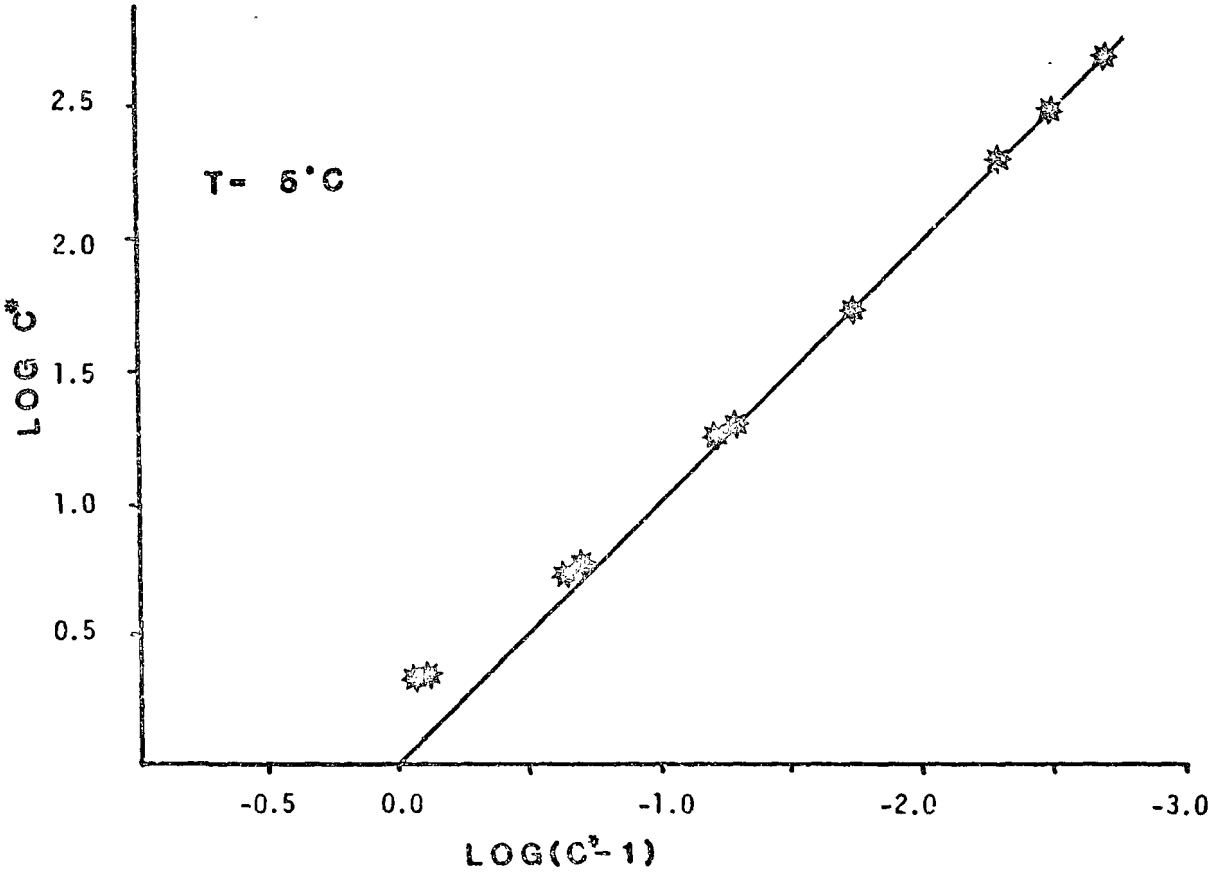

Figure 35. Frank-Kamenetskii plot of kinetic data at 5°C.

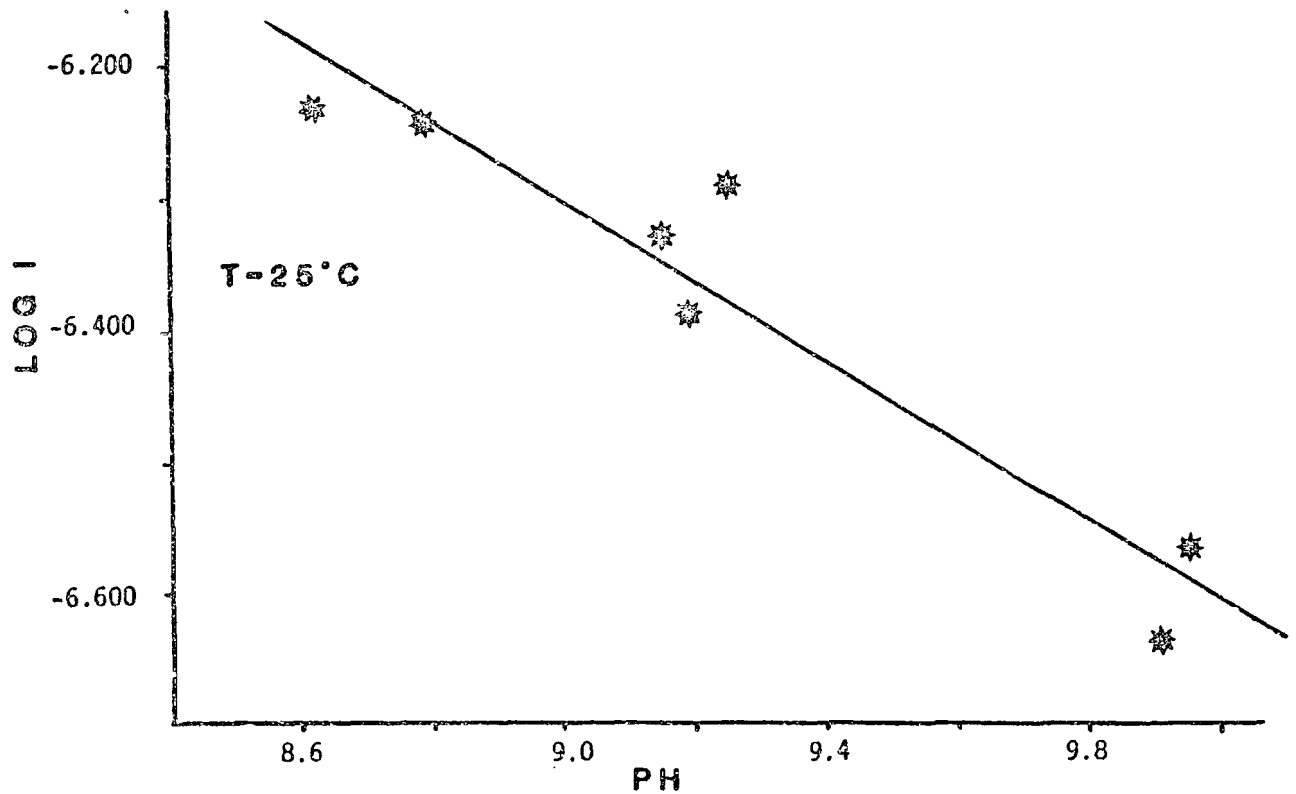

Figure 36. Kinetic data of region I at 25°C.

Table 12. Region I Data: 25°C

T(°C)	I ($\mu A/cm^2$)	pH_B	log I
25	0.59	8.62	-6.229
25	0.57	8.79	-6.244
25	0.47	9.15	-6.328
25	0.41	9.19	-6.387
25	0.51	9.25	-6.292
25	0.23	9.91	-6.638
25	0.27	9.95	-6.569

$$I = (2.509 \times 10^{-4})\ 10^{-0.30\ pH_B}$$

for I in units of A/cm^2. The Arrhenius factor, a, can be calculated since:

$$Co = \left(\frac{nFa}{10^{-6}}\right)K_w^b\ (10^{-3})^b = 2.509 \times 10^{-4}$$

or $$a = 3.26 \times 10^{-10}$$

Since no region I data were taken at temperatures other than 25°C it is not possible to determine the value of the activation energy, E_A, of the rate limiting step or the frequency factor, A.

Figure 37 shows a plot of data collected over the pH range of 6.0 to 10.0 at 25°C along with the regressed kinetic rate expression determined above. The regressed rate expression predicts a kinetic rate that is higher than that actually measured at pH < 8.5, which is in accord with the earlier realization that below pH = 8.5 the effects of solution mass transport tend to slow down the overall rate of the corrosion process. Whether or not the quantitative kinetic rate expression developed at high pH is appropriate for

data taken at pH < 8.5 can only be determined by evaluation of the data which fall into regions II and III.

Analysis of Data in Region II

Data that fall in the region of mixed kinetic/mass transport rate control are analyzed by first transforming variables (I, pH_B, T) into (X, Y, T) for each data point. Then by linearly regressing the values of Y on X at each temperature kinetic parameters a and b can be found from the intercept and slope of the regression line respectively. The regression variables X and Y are calculated from raw data values as follows:

$$X = \log \left[10^{-3} K_w 10^{pH_B} + \frac{I(10^{-6})\delta_D}{nF D_{OH}}\right]$$

and

$$Y = \log \left[\frac{I(10^{-6})}{nF}\right]$$

and tabulated in Table 13.

Only data taken at 25°C are analyzed in this fashion since approximately all lower temperature data fell into region III. A plot of Y versus X for data points in this region is shown in Figure 38. The solid line on the plot corresponds to the regressed linear relationship between X and Y, which can be expressed as follows:

$$Y = -6.814 + 0.461 X$$

with: $r^2 = 0.848$

which leads to the following rate expression for data in this region:

$$I = (1.482 \times 10^{4}) C_S^{0.461}$$

where C_S is found by solving the following non-linear algebraic equation:

$$C_S^{0.461} - (2.205 \times 10^5) C_S + (2.227 \times 10^{-12}) 10^{pH_B} = 0$$

Analysis of Data in Region III

In region III, the corrosion process is under rate control by diffusion through solution. The rate expression appropriate for this condition was derived earlier on to be:

Table 13. Region II Data: 25°C

T(°C)	I ($\mu A/cm^2$)	pH_B	Added $[HCO_3^-]$ (mg/ℓ)	y	x
25	0.56	7.10	0	-11.236	-9.528
25	0.74	7.33	0	-11.115	-9.357
25	1.17	7.89	0	-10.916	-8.944
25	0.74	7.36	10	-11.115	-9.339
25	0.85	7.37	10	-11.055	-9.304
25	0.74	7.60	10	-11.115	-9.202
25	0.94	7.82	10	-11.011	-9.020
25	0.84	7.60	10	-11.060	-9.181
25	0.92	7.58	10	-11.021	-9.177

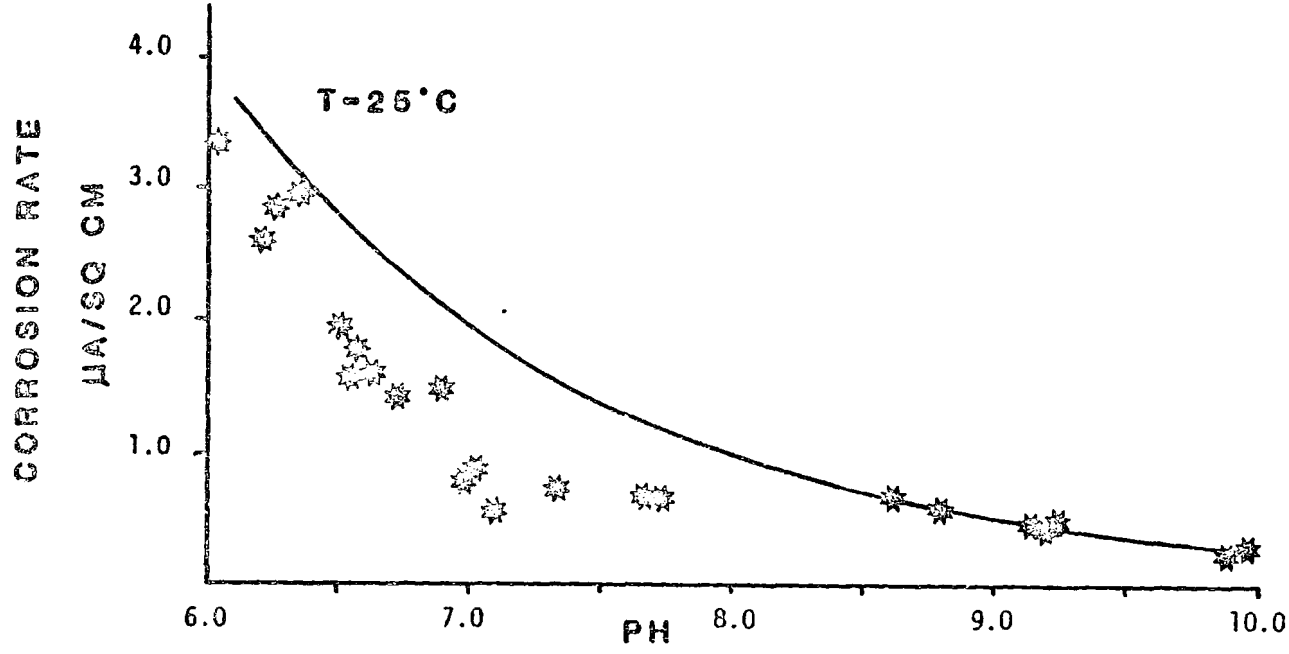

Figure 37. Comparison of region I results with all kinetic data at 25°C.

$$I = \left(\frac{nF\ D_{OH}\ p(10^{-3}\ K_w)^b}{10^{-6}\ \delta_D}\right) \cdot 10^{bpH_B}$$

which can be reduced to the linear form of:

$$\log I = c_o + b\ pH_B$$

where: $$c_o = \log \left[\frac{nFD_{OH}\ p(10^{-3}\ K_w)^b}{10^{-6}\ \delta_D}\right]$$

Data points in the form of (log I, pH_B) can be regressed at each temperature to find values of p and b. Data points in region III are shown in Table 14 and plotted in Figures 39 and 40 for 25°C, 15°C and 5°C respectively. The solid line on each plot corresponds to the regressed linear relationship between log I and pH.

At 25°C regression results in the following linear relationship:

$$\log I = -1.842 - 0.597\ pH_B$$

with: $r^2 = 0.975$

which leads to the following rate expression:

$$I = (1.440 \times 10^{-2})\ 10^{-0.597\ pH_B}$$

from this, the value of p can be calculated which is independent of temperature:

$$\left(\frac{nF\ D_{OH}\ p(10^{-3}K_w)^b}{10^{-6}\ \delta_D}\right) = 1.440 \times 10^{-2}$$

So: $p = 3.15 \times 10^{-22}$

This leads to the following general rate expression:

$$I = \left(\frac{1.876 \times 10^{-9}\ D_{OH}}{\delta_D\ K_w^{0.597}}\right) 10^{-0.597pH_B}$$

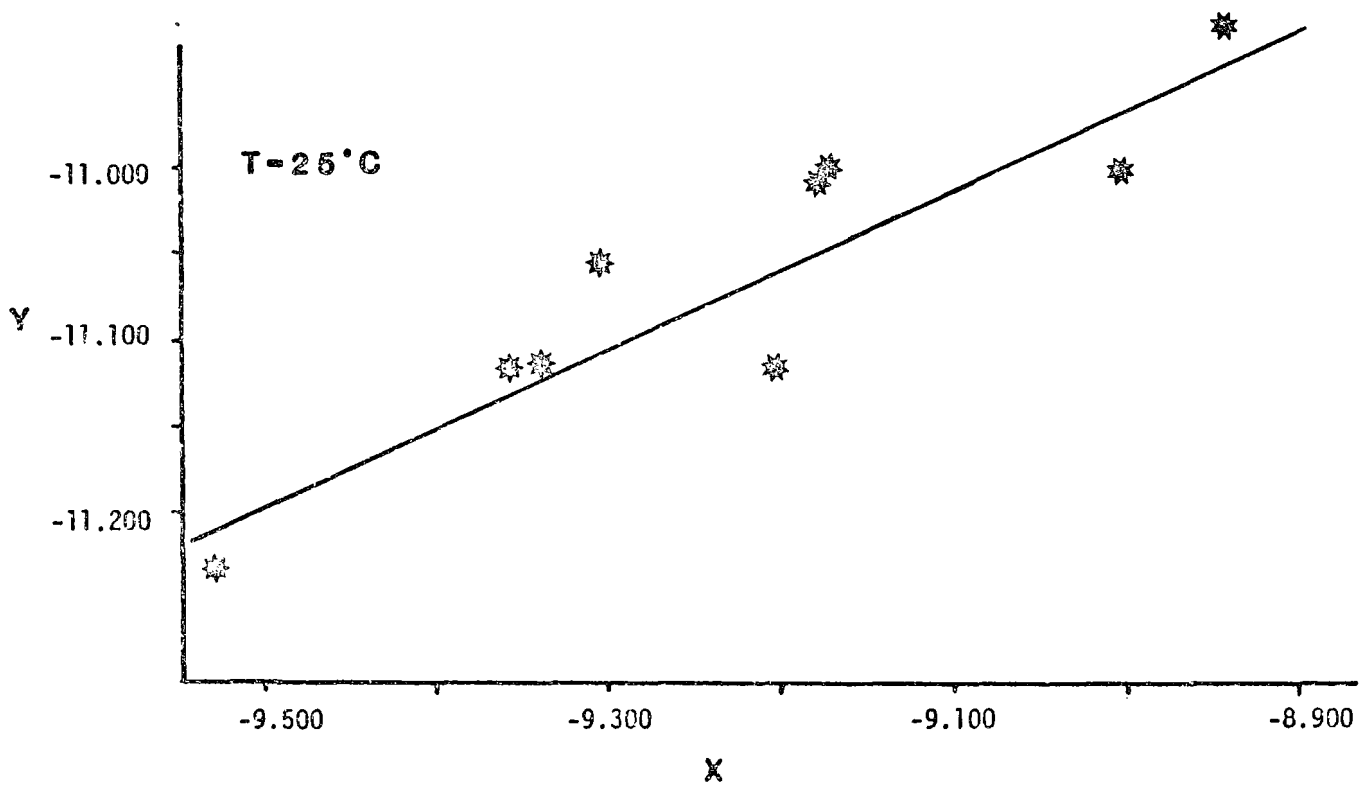

Figure 38. Kinetic data of region II at 25°C.

Table 14. Region III Data: 25°C, 15°C, and 5°C

T (°C)	pH_B	I ($\mu A/cm^2$)	log I
25	6.05	3.35	-5.475
25	6.24	2.62	-5.582
25	6.25	2.88	-5.541
25	6.51	1.78	-5.703
25	6.54	1.61	-5.793
25	6.57	1.84	-5.735
25	6.73	1.44	-5.842
25	6.65	1.64	-5.785
25	6.99	0.90	-6.056
25	7.02	0.96	-6.018
15	6.22	2.27	-5.644
15	6.27	3.37	-5.472
15	6.65	1.33	-5.876
15	6.50	1.59	-5.799
15	6.93	1.81	-5.743
15	6.52	2.37	-5.625
5	6.32	3.71	-5.431
5	6.37	2.58	-5.588
5	7.18	1.04	-5.983
5	6.79	1.17	-5.932

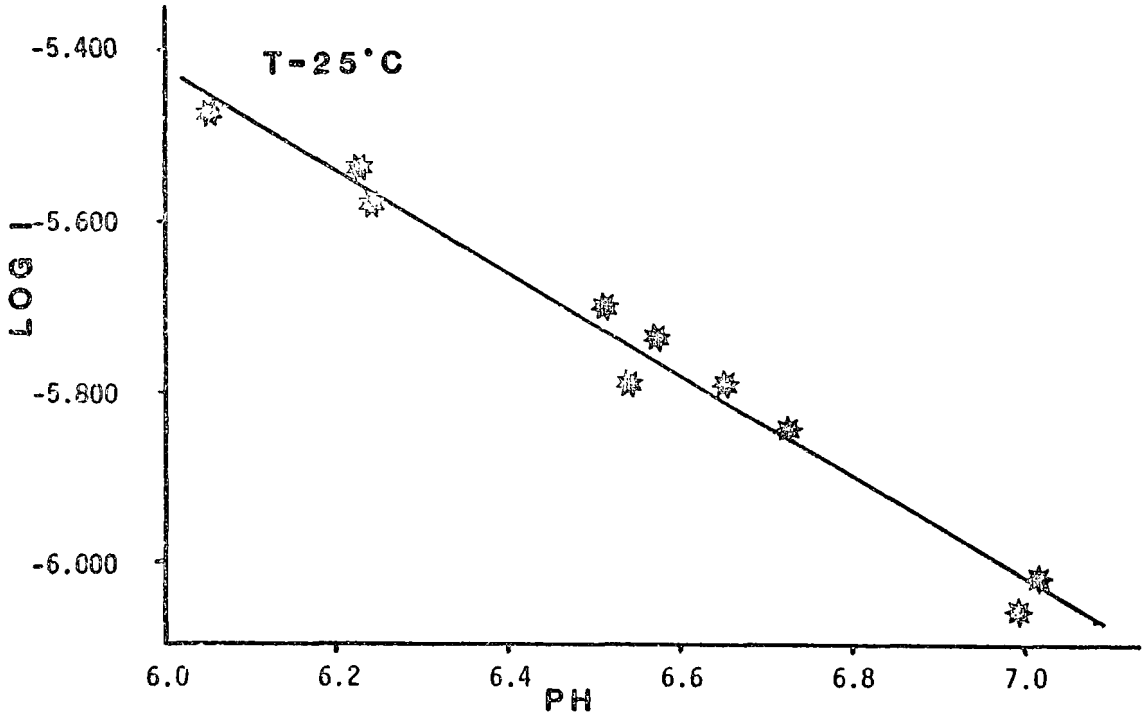

Figure 39. Kinetic data of region III at 25°C.

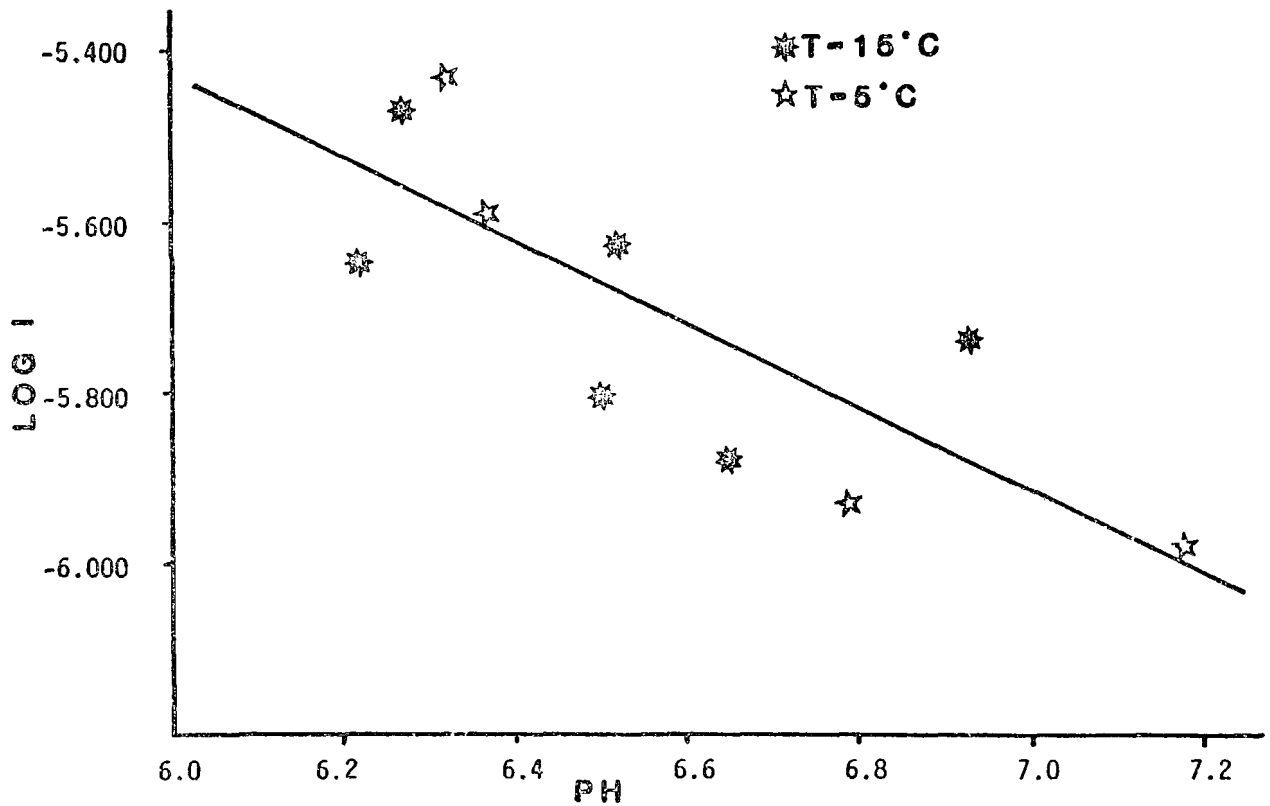

Figure 40. Kinetic data of region III at 15°C. and 5°C.

Where the temperature dependence is imbedded in D_{OH}, δ_D. and K_w.

At temperatures of 15 and 5°C the data points were of fewer number and a plot of log I versus pH_B values indicated that data at both temperatures could effectively not be distinguished. These data were then regressed together to give the following rate expression:

$$I = (3.074 \times 10^{-3})\ 10^{-0.486\ pH_B}$$

with: $r^2 = 0.647$.

from which p can be calculated at 15 and 5°C.

At T = 15°C: $p = 4.35 \times 10^{-21}$

At T = 5°C: $p = 3.63 \times 10^{-21}$

The following general rate expressions then pertain:

$$I = \frac{1.21 \times 10^{-8}\ D_{OH}}{\delta_D\ K_w^{0.486}}\ 10^{-0.486 pH_B} \quad \text{at } 15°C$$

and

$$I = \frac{1.00 \times 10^{-8}\ D_{OH}}{\delta_D\ K_w^{0.486}}\ 10^{-0.486 pH_B} \quad \text{at } 5°C$$

As noted before the temperature dependence is imbedded in D_{OH}, δ_D, and K_w.

Experiments designed to be under rate control by interfacial reaction kinetics have turned out to be principally under rate control by solution mass transport of OH^- away from the reacting surface. At low pH (less than 7.0) solution mass transport rate control was evident at all three temperatures tested. At temperatures lower than 25°C, mass transport rate control was extended to higher bulk pH values. Since at low pH mass transport rate control predominates, extension of results to pH values lower than those tested is easily done.

RATE CONTROL BY OXIDE FILM GROWTH AND TRANSPORT

Data presented in this section resulted from experiments designed to measure corrosion rates under the conditions of rate control by oxide film growth or solid-state transport. It was assumed that by minimizing the

effects of other component rate processes that the dependency of the rate of oxide film growth on pH and temperature could be determined quantitatively. Experimentally this meant running polarization curves on electrochemically aged copper electrodes rotated at 3000 RPM. The electrochemical aging process consisted of passing a 10 μA anodic current across the electrode solution interface for a period of two hours at the appropriate temperature and pH. These conditions promote oxide film growth in great excess of that needed to attain a steady-state thickness of Cu_2O. At 20 μA hr film thickness greater than 2000 Å could be attained if all copper oxidized went into forming the film, film dissolution was zero, and the film didn't break up. But the film is dissolving and breaking up so the 20 μA hr age time represents the shortest preparation time that gave cell current density values consistently as low as those measured at longer age times, indicating that the oxide film was exerting its maximum influence on the overall rate of the corrosion process. Rotation of the disc electrode at 3000 RPM, as explained earlier increases the rate of all solution mass transport processes minimizing their influence on the rate of the overall process. So the measured corrosion rate was intended to correspond to the rate of oxide film growth or solid-state transport through the oxide film. Rate variations with respect to pH and temperature are used to compare data with theoretical models developed in Section 6 for early and late stage film growth by quantum mechanical tunnelling.

A schematic diagram of the metal/oxide/solution system in which corrosion rate data presented in this section were taken is shown in Figure 41 below.

By minimizing the effects of mass transport in solution, the rate of oxide film growth which corresponds to the rate at which electron holes, $\overset{\circ}{h}$, and copper cation vacancies, $Cu^{+}[]$, are transported across the film, can be measured. A plot of log C^{*} versus log $(C^{*}-1)$ was then expected to give data points falling into Region I, the region in which the overall rate is completely controlled by the underlying rate process, free of solution mass transport influences. As it turns out, these data reflect an influence of solution mass transport of a reaction product away from the oxide/solution interface similar to that found for the data under interfacial reaction rate

control. So these experimental conditions turn out to give data that reflect the joint influence of:

1) Mass transport in solution (presumably OH^-)
2) Oxide film growth

The methods of Frank-Kamenetskii are then called upon once again to quantify the pH and temperature dependence of the coupled rate process of oxide film growth in the presence of OH^- diffusion. A rate expression that expresses the joint effects of these two processes can be developed from the data.

Data taken are shown in Tables 15, 16, and 17 for 25°C, 15°C and 5°C respectively. Plots of log C^* versus log (C^*-1) shown in Figures 42, 43 and 44 indicate that many of the data points fall into region III, the region of diffusion in solution control. Not enough data fell into region II to be able to characterize the underlying rate process so all data were evaluated in the form (log I, pH_B), as per region III. Estimates of the slope, b, and intercept, a, can be calculated for the relationship:

$$\log I = a + b\ pH_B$$

These values are presented in Table 18 along with 95% confidence interval values for each estimate and calculated values of p at each temperature.

The following rate expression appropriate for coupled oxide film growth and solution mass transport of OH^- can be used to predict rates of copper corrosion at 25, 15, and 5°C:

$$I = \left[\frac{nF\ D_{OH}\ p(10^{-3}\ K_w)^b}{10^{-6}\ \delta_D}\right] 10^{pH_B}$$

Values of parameters necessary for corrosion rate calculation are given in Table 19 below. Figures 45, 46 and 47 show the precision with which the quantitative rate expression fits the data at all three temperatures.

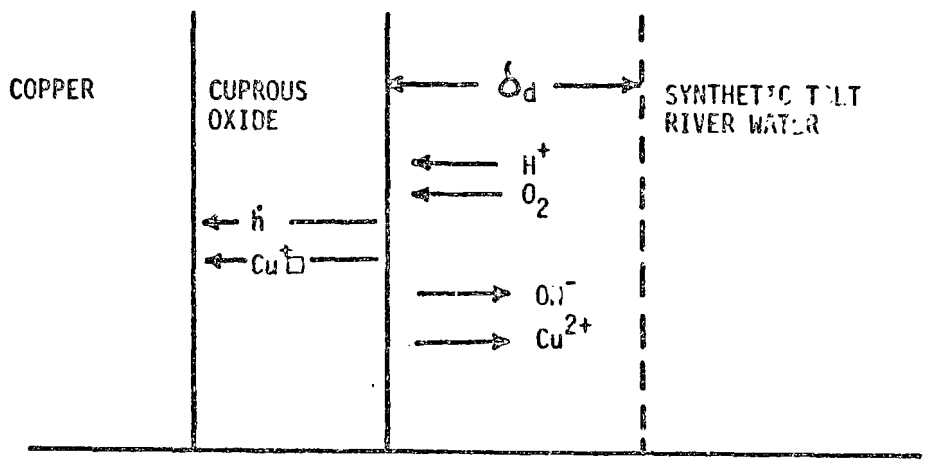

Figure 41. Electrode/solution interface in experiments designed for oxide film growth rate control.

Table 15. Oxide Film Growth Rate Control Data: 25°C.

Run No.	T (°C)	pH	I_{COR} ($\mu A/cm^2$)	RPM	κ ($\frac{\mu mhos}{cm}$)	R_Ω	Growth Time ($\mu A \cdot hr$)	log C*	pH_S
1	25	6.24	0.96	3000	13.5	20,000	20	1.25	7.49
2	25	8.40	0.51	3000	16.7	16,000	20	0.03	8.43
3	25	6.01	0.87	3000	12.7	26,000	20	1.14	7.45
4	25	8.09	0.49	3000	18.5	16,000	20	0.05	8.14
5	25	7.18	0.58	3000	16.6	21,000	20	0.34	7.52
6	25	7.38	0.62	3000	16.6	21,000	20	0.25	7.63
7	25	7.19	0.72	3000	16.6	21,000	20	0.38	7.57
8	25	7.90	0.66	3000	17.0	19,000	20	0.10	8.00
9	25	6.22	0.98	3000	13.4	25,000	20	1.28	7.50
10	25	6.43	0.68	3000	15.1	23,000	20	0.94	7.37

Table 16. Oxide Film Growth and Rate Control Data: 15°C.

Run No.	T (°C)	pH	I_{COR} ($\mu A/cm^2$)	RPM	κ ($\frac{\mu mhos}{cm}$)	R_Ω	Growth Time ($\mu A \cdot hr$)	log C*	pH_S
1	15	6.66	0.71	3000	12.6	24,000	20	1.15	7.81
2	15	7.97	0.56	3000	15.4	18,000	20	0.18	8.15
3	15	6.21	0.62	3000	11.8	27,000	20	1.52	7.73
4	15	7.06	0.71	3000	15.9	21,000	20	0.80	7.86
5	15	6.88	0.49	3000	14.9	26,000	20	0.81	7.69
6	15	6.87	0.50	3000	15.4	21,000	20	0.83	7.70
7	15	8.33	0.43	3000	18.1	13,000	20	0.07	8.40
8	15	6.04	0.78	3000	11.5	24,000	20	1.79	7.83
9	15	7.59	0.54	3000	14.0	27,000	20	0.34	7.93

Table 17. Oxide Film Growth Rate Control Data: $5^{o}C$.

Run No.	(°C)	T pH	I_{COR} ($\mu A/cm^2$)	RPM	κ ($\frac{\mu mhos}{cm}$)	R_{Ω}	Growth Time ($\mu A \cdot hr$)	log C*	pH_S
1	5	7.50	0.63	3000	11.0	29,000	20	0.81	8.31
2	5	7.40	0.38	3000	11.0	28,000	20	0.71	8.11
3	5	8.47	0.47	3000	14.0	19,000	20	0.16	8.63
4	5	8.16	0.48	3000	13.3	23,000	20	0.28	8.44
5	5	7.28	0.37	3000	11.6	27,000	20	0.80	8.08
6	5	6.86	0.49	3000	10.4	28,000	20	1.29	8.15
7	5	6.77	0.56	3000	9.4	32,000	20	1.48	8.21
8	5	7.99	0.43	3000	11.7	23,000	20	1.35	8.34
9	5	6.48	0.57	3000	10.6	24,000	20	1.73	8.21
10	5	6.25	0.54	3000	9.8	27,000	20	1.92	8.18

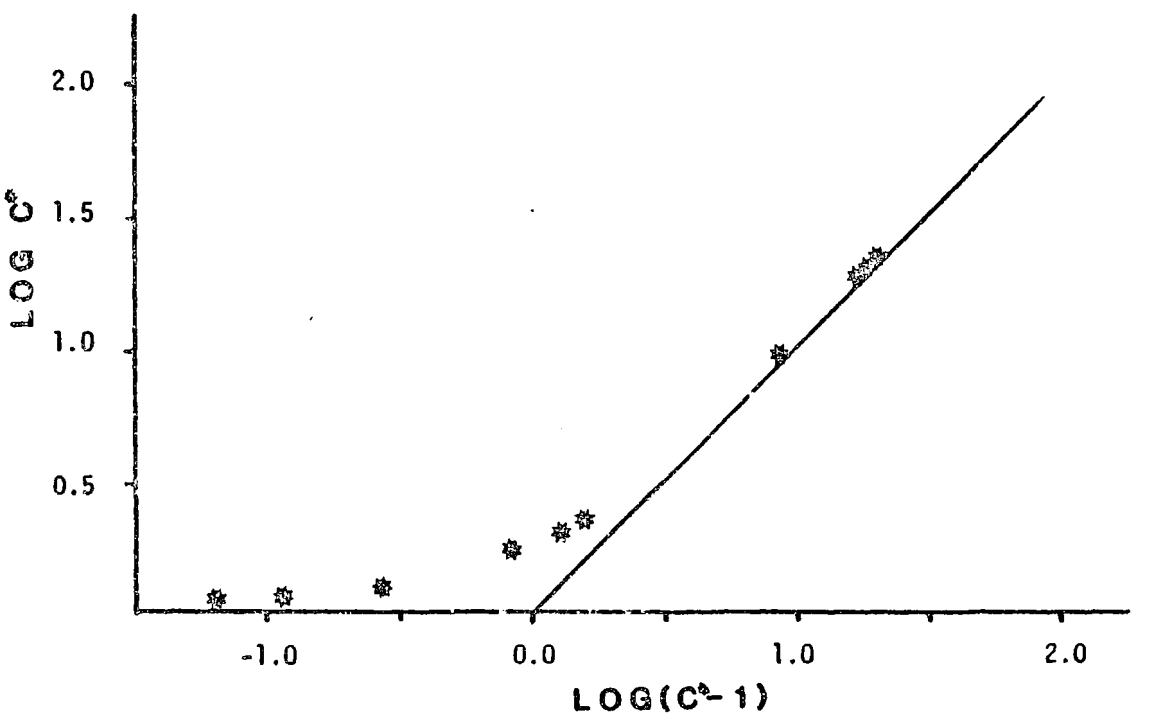

Figure 42. Frank-Kamenetskii plot of oxide film growth data at 25°C.

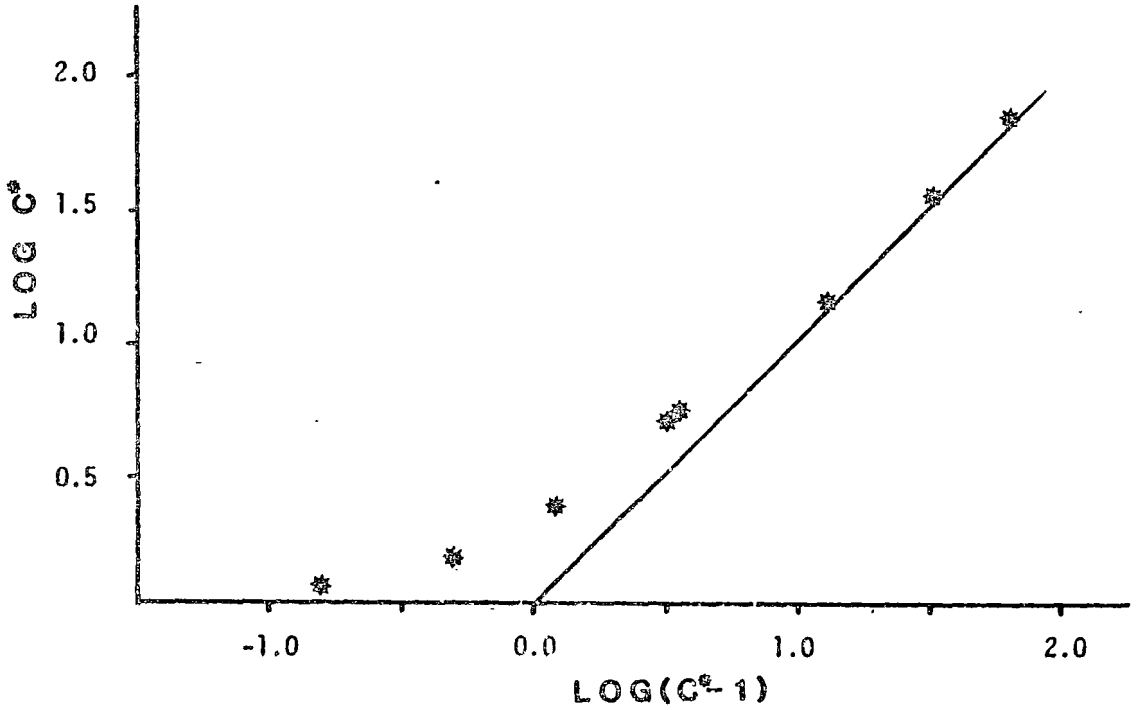

Figure 43. Frank-Kamenetskii plot of oxide film groth data at 15°C.

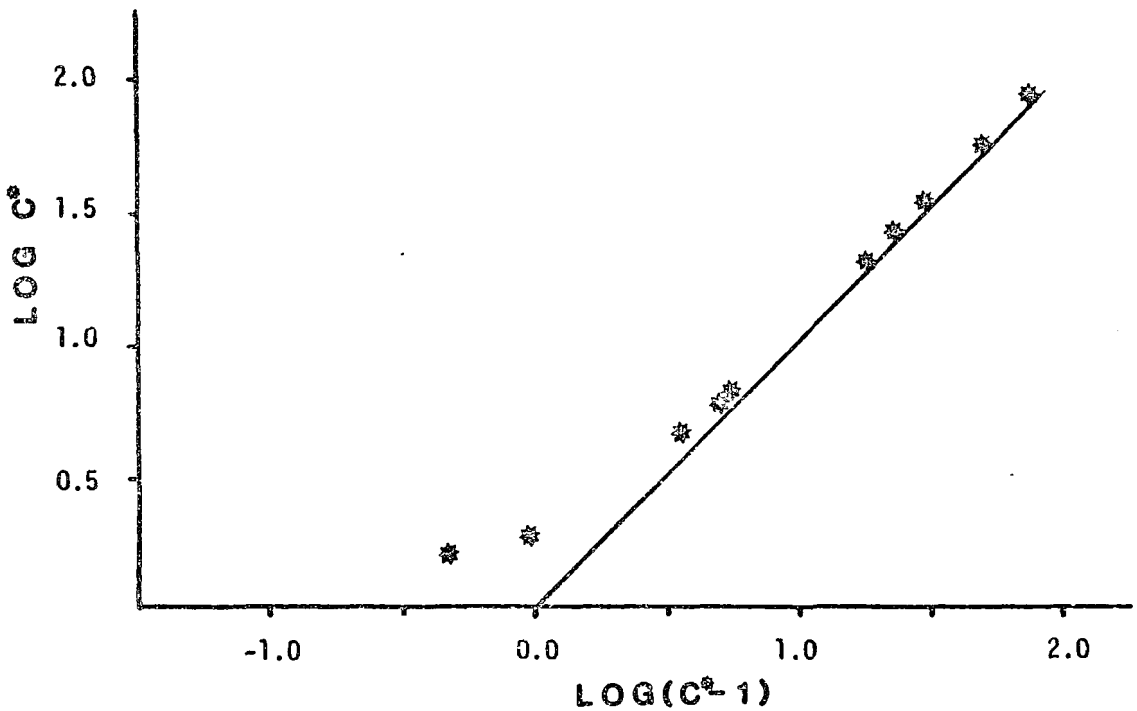

Figure 44. Frank-Kamenetskii plot of oxide film growth data at 5°C.

Table 18. Regression Results for Oxide Film Growth Data

T	a	$\pm a_{(95)}$	b	$\pm b_{(95)}$	r	p
25	- 4.845	± .428	- 0.183	± .060	- 0.929	3.393×10^{-18}
15	- 5.608	± .444	- 0.085	± .062	- 0.847	3.151×10^{-17}
5	-6.023	± .257	- 0.038	±.035	- 0.790	9.971×10^{-17}

Table 19. Parameter Estimates Calculated for oxide Film Growth Data.

T°C	b	p	D_{OH}	K_w	$\delta_{D(at\ 3000\ RPM)}^{RDE}$
25	-0.183	3.39×10^{-18}	5.26×10^{-5}	1.01×10^{-14}	1.553×10^{-3}
15	-0.085	3.15×10^{-17}	3.98×10^{-5}	0.45×10^{-14}	1.463×10^{-3}
5	-0.038	9.97×10^{-17}	2.89×10^{-5}	0.18×10^{-14}	1.385×10^{-3}

RATE CONTROL BY SOLUTION MASS TRANSPORT

Data under rate control by solution mass transport were taken by designing experiments in which the influence of interfacial reaction kinetics and oxide film growth were minimized. This was done by running polarization curves on freshly polished copper electrodes that were not rotated. Under these conditions mass transport through stagnant solution was expected to be the slowest step in the overall corrosion process. A comparison of rates measured under conditions of kinetic or oxide film growth rate control with solution mass transport data taken at the same pH and temperature indicate that in all cases measured rates were significantly reduced when the working electrode was not rotated. This is an indication that solution mass transport rate processes are going on and do influence the overall corrosion rate

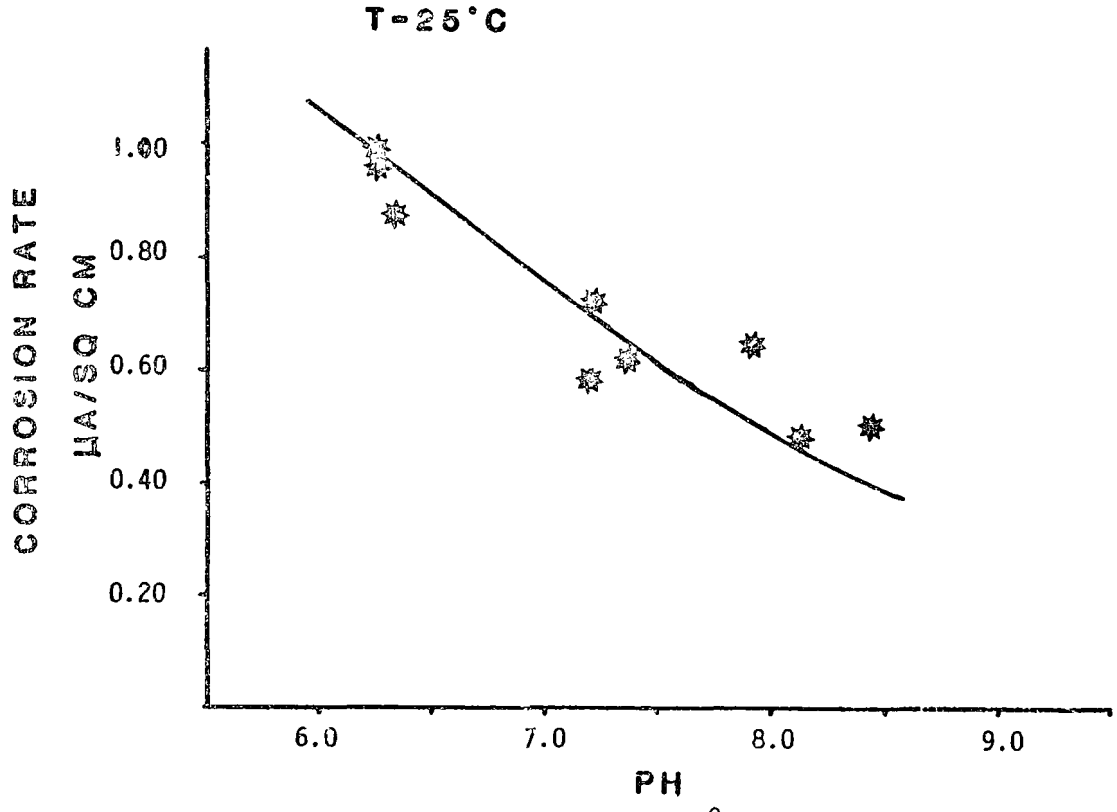

Figure 45. Oxide film growth data at 25°C.

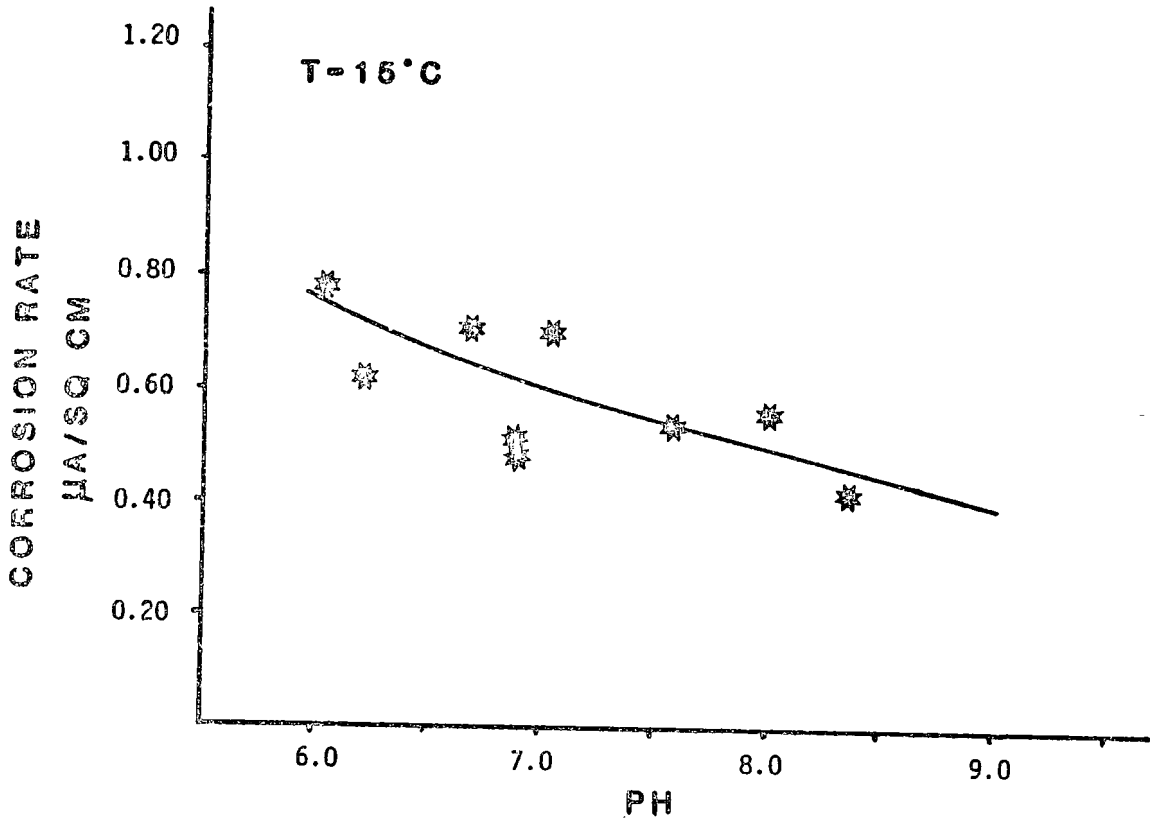

Figure 46. Oxide film growth data at 15°C.

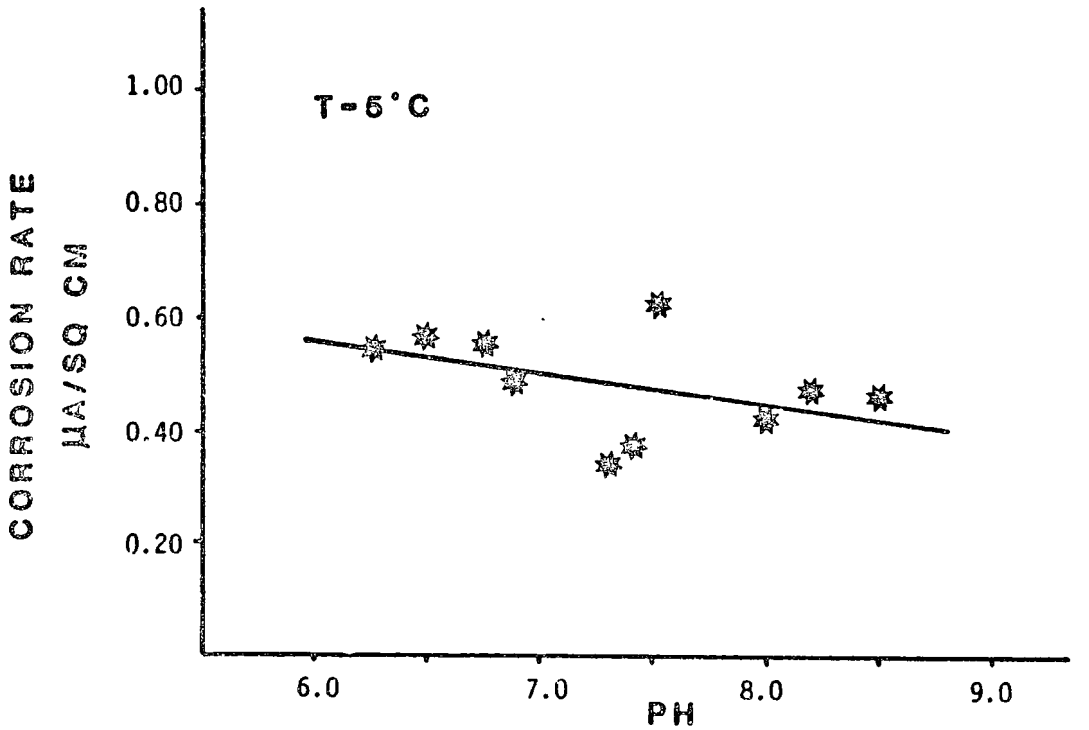

Figure 47. Oxide film growth data at 5°C.

especially in stagnant solution. These data then were taken under conditions most likely to produce complete rate control by solution mass transport. Rate variations in the data with respect to pH and temperature should then correspond to the pH and temperature dependence of the rate controlling diffusion process. This could be the rate of mass transport of H^+ or O_2 to the electrode surface to act as reactants in the cathodic half-cell reaction or mass transport of OH^- or Cu^{2+} away from the electrode surface as reaction products of the cathodic half-cell or oxide film dissolution reaction respectively. A schematic diagram representing the metal/oxide/solution system from which data presented in this section were measured is shown in Figure 48.

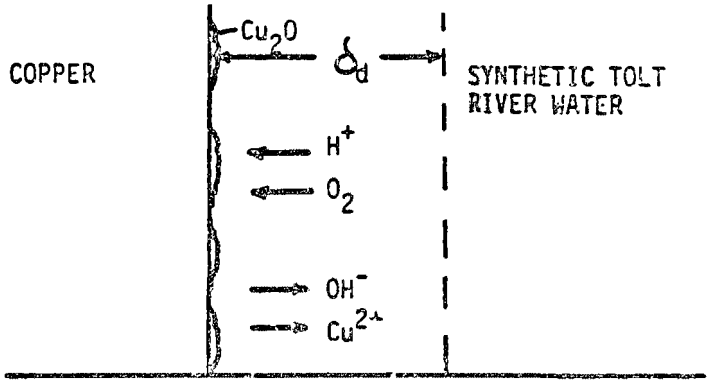

Figure 48. Electrode/solution interface in experiments designed for stagnant diffusion rate control.

Since the diffusion layer thickness, δ_D, is time dependent and of different magnitude for each diffusing species time-averaged mass transport rates are necessary for each diffusing species. Appropriate rate expressions were developed in Section 4 and are presented here as follows:

1. For diffusion of H^+ from bulk solution to interface:

$$I = \left[\frac{2nFD_{H^+}(10^3)[1 + a(\frac{D_{H^+}t}{r^2})^{1/2}]}{\pi^{1/2} \; t^{1/2}} \right] [H^+]_B$$

when: $[H^+]_B >> [H^+]_S$

$n = 1$ mole e^-/mole

2. For diffusion of O_2 from bulk solution to interface:

$$I = \left[\frac{2nFD_{O_2}(10^3)[1 + a(\frac{D_{O_2} t}{r^2})^{1/2}]}{\pi^{1/2} t^{1/2}} \right] [O_2]_B$$

when: $[O_2]_B >> [O_2]_S$

$n = 4$ moles e^-/mole O_2

3. For diffusion of OH^- from interface to bulk solution:

$$I = \left[\frac{2nF\ D_{OH}\ (10^3)\ [1 + a(\frac{D_{OH} t}{r^2})^{1/2}]}{\pi^{1/2}\ t^{1/2}} \right] \left([OH^-]_S - [OH^-]_B \right)$$

$n = 1$ mole e^-/mole OH^-

4. For diffusion of Cu^{2+} from interface to bulk solution:

$$I = \left[\frac{2nF\ D_{Cu^{2+}}(10^3)[1 + a(\frac{D_{Cu}\ t}{r^2})^{1/2}]}{\pi^{1/2}\ t^{1/2}} \right] [Cu^{2+}]_S$$

when: $[Cu^{2+}]_S >> [Cu^{2+}]_B$ and $[Cu^{2+}]_S \approx \frac{K_{sp\ Cu(OH)_2}}{[OH^-]_S^2}$

$n = 1$ mole e/mole Cu^{2+}

In all of these expressions, $a = 2.12$, $r^2 = 0.2270\ cm^2$, and the stagnation time, t, is taken as 40 sec. Experimental results are presented next and ultimately compared with these rate expressions for determination of which diffusing species is rate controlling.

Data taken are shown in Table 20, 21 and 22 for 25°C, 15°C and 5°C respectively. A plot of log C^* versus log (C^*-1), in Figures 49, 50 and 51 will be shown later, indicates that a great majority of data points at all

Table 20. Stagnant Diffusion Data: 25°C

Run No.	T (°C)	pH	I_{COR_2} ($\mu A/cm^2$)	RPM	($\frac{\mu mhos}{cm}$)	R_Ω	log C*	pH_S
1	25	6.39	0.55	0	14.0	23,000	2.17	8.56
2	25	6.38	0.48	0	14.3	23,000	2.12	8.50
3	25	6.39	0.48	0	14.1	23,000	2.11	8.50
4	25	7.39	0.36	0	15.2	18,000	1.03	8.42
5	25	8.84	0.16	0	16.2	17,000	0.06	8.90
6	25	7.33	0.42	0	15.1	17,000	1.14	8.47
7	25	7.06	0.43	0	14.9	18,000	1.41	8.47
8	25	8.45	0.21	0	16.1	17,000	0.17	8.62
9	25	8.56	0.31	0	15.8	17,000	0.19	8.75
10	25	6.86	0.46	0	16.9	16,000	1.63	8.49
11	25	7.70	0.39	0	16.6	16,000	0.79	8.49
12	25	8.82	0.16	0	17.7	15,000	0.06	8.88
13	25	8.22	0.31	0	16.0	16,000	0.35	8.57
14	25	7.85	0.33	0	15.2	19,000	0.61	8.46
15	25	6.02	0.53	0	13.1	23,000	2.52	8.54
16	25	9.37	0.16	0	18.5	14,000	0.02	9.39

Table 21. Stagnant Diffusion Data: 15°C.

Run No.	T (°C)	pH	I_{COR} ($\mu A/cm^2$)	RPM	κ ($\frac{\mu mhos}{cm}$)	R_Ω	log C*	pH_S
1	16	6.44	0.38	0	12.3	29,000	2.38	8.82
2	15	8.31	0.15	0	14.5	21,000	0.37	8.68
3	15	6.73	0.27	0	11.9	30,000	1.95	8.68
4	15	9.59	0.23	0	18.7	16,000	0.03	9.72
5	16	6.05	0.39	0	10.5	33,000	2.78	8.83
6	16	6.97	0.32	0	12.7	25,000	1.78	8.75
7	16	7.90	0.15	0	13.1	26,000	0.63	8.53
8	16	7.31	0.25	0	12.8	28,000	1.35	8.66
9	15	7.62	0.25	0	13.0	26,000	1.06	8.68

Table 22. Stagnant Diffusion Data: $5^{o}C$.

Run No.	T (°C)	pH	I_{COR} ($\mu A/cm^2$)	RPM	κ ($\frac{\mu mhos}{cm}$)	R_{Ω}	log C*	pH_S
1	5	7.08	0.23	0	12.1	25,000	2.00	9.08
2	5	7.25	0.22	0	13.0	23,000	1.82	9.07
3	5	7.26	0.22	0	11.4	26,000	1.81	9.07
4	5	8.36	0.13	0	11.5	26,000	0.60	8.96
5	5	6.05	0.35	0	10.2	30,000	3.21	9.26
6	5	6.36	0.26	0	12.2	25,000	2.77	9.13
7	5	6.30	0.40	0	11.4	30,000	3.02	9.32
8	5	6.36	0.31	0	12.7	27,000	2.85	9.21
9	5	8.39	0.25	0	11.0	28,000	0.80	9.19
10	5	8.81	0.12	0	12.2	26,000	0.29	9.10
11	5	8.71	0.18	0	13.6	24,000	0.45	9.16

three temperatures lie in Region III, the region of rate control by diffusion in solution. Data are then analyzed in the form {log I, pH_B}. Estimates of the slope, b, and intercept, a, for the relationship:

$$\log I = a + b\ pH$$

are presented in Table 23, along with 95% confidence interval values. The correlation coefficient, r, for each data set is also presented.

The log I versus pH_B plot can be used to determine which of the possible diffusing species is actually rate limiting. The possible species, as mentioned earlier, are H^+, O_2, OH^-, and Cu^{2+}. Considering the general expression:

$$\log I = a_0 + b_0\ pH_B$$

The values of a_0 and b_0 appropriate for rate control by diffusion of H^+ or O_2 to the electrode surface and diffusion of Cu^{2+} away from the electrode surface are given in Table 24 below. The values of a_0 and b_0 predicted for each of the diffusing species above are then compared to values of a and b determined by regression of the data points.

By Null hypothesis testing (5) one can determine whether the regressed values of a and b differ significantly from the theoretical values of a_0 and b_0 for each diffusing species. If the (a_0, b_0) values of one diffusing species do not differ significantly from the regressed (a,b) values that species can be selected as the rate controlling diffusing species. In Table 25 below the results of these tests are described by a (+) for acceptance of the Null hypothesis and a (-) for rejection of the Null hypothesis. The Null hypothesis in each case is that a = a_0 or b = b. A (+) therefore means that there is no significant difference between a and a_0 or b and b_0. A (-) means that there is a significant difference. All comparisons are made at 25°C. On the basis of these tests none of the species above can be selected to explain the data at 25°C under conditions of diffusion in solution rate control.

The diffusion of OH^- was not considered in the table above since it involves coupling of an underlying process that is dependent upon the surface hydroxide concentration with that of mass transport in solution. The method

Table 23. Regression Results for Stagnant Diffusion Data

T	a	± a(95)	b	± b(95)	r
25	- 5.6061	± .1913	- 0.109	± .027	- 0.950
15	- 5.1866	± .5499	- 0.196	± .076	- 0.932
5	- 5.8132	± .5765	- 0.111	± .071	- 0.793

Table 24. Calculated Diagnostic Parameters for Diffusion Rate Control

Species	a_0 (Functional Form)	a_0 (T = 25°C)	b_0
H^+	$\log\left[\frac{10^{+3}\ nF\ D_{H^+}}{\delta D_{H^+}}\right]$	+ 5.325	-1.0
O_2	$\log\left[\frac{10^{3}\ nF\ D_{O_2}\ [O_2]_B}{\delta D_{O_2}}\right]$	+ 1.950	0
Cu^{2+}	$\log\left[\frac{10^{3}\ nF\ D_{Cu^{2+}}\ K_{Sp}\ Cu(OH)_2}{K_w^2\ \delta D_{Cu^{2+}}}\right]$	+13.030	-2.0

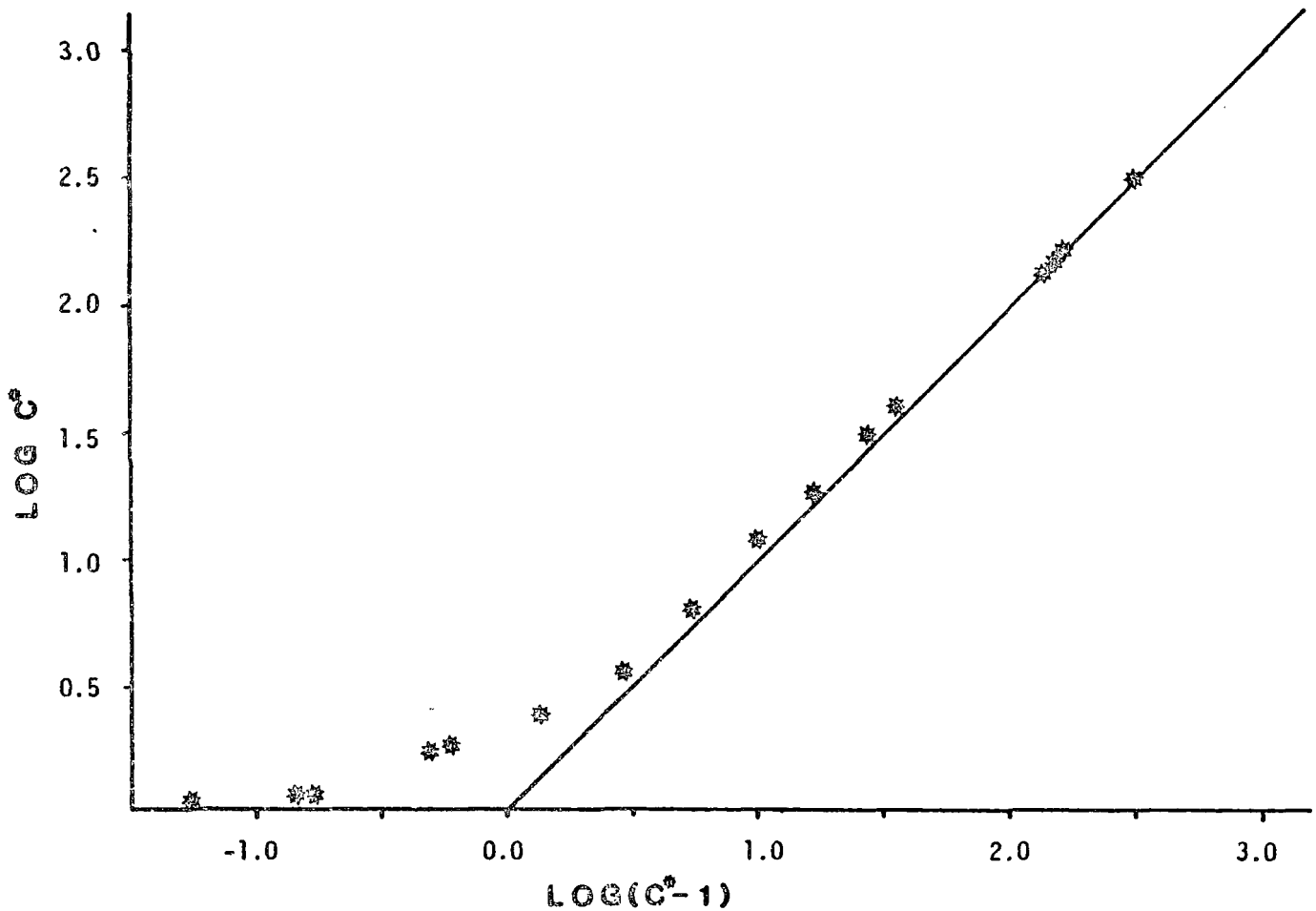

Figure 49. Frank-Kamenetskii plot of stagnant diffusion data at 25°C.

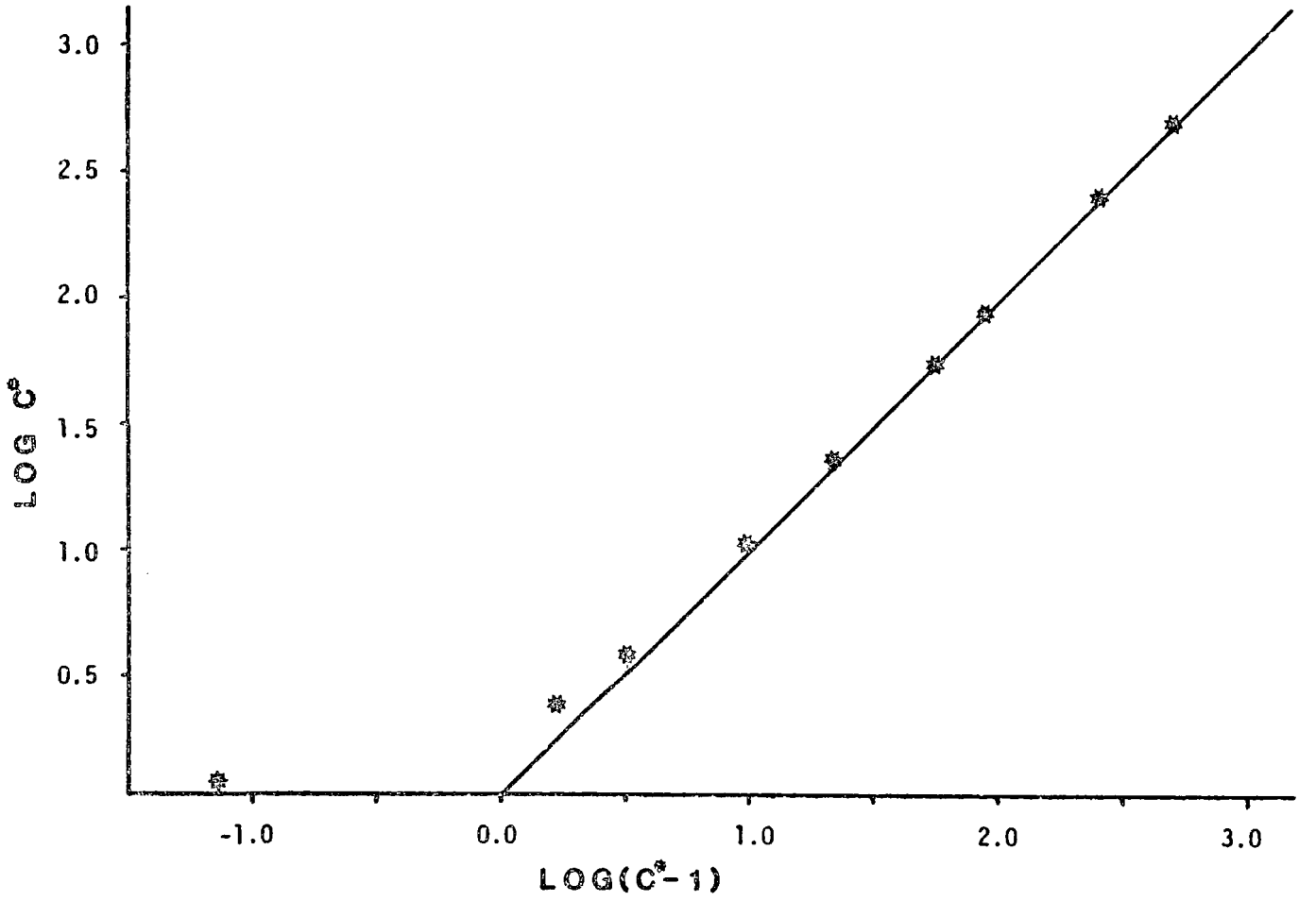

Figure 50. Frank-Kamenetskii plot of stagnant diffusion data at 15°C.

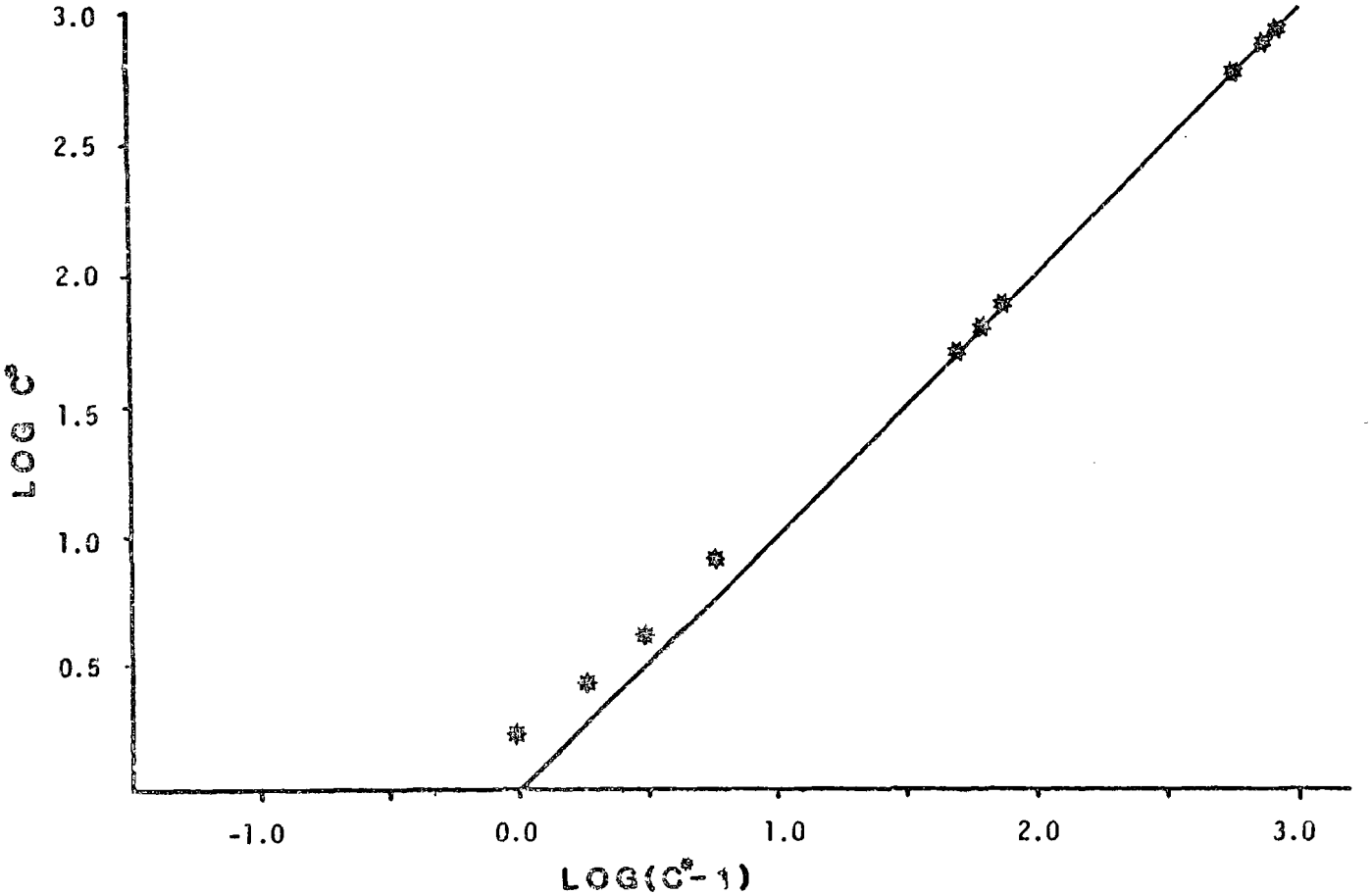

Figure 51. Frank-Kamenetskii plot of stagnant diffusion data at 5°C.

Table 25. Null Hypothesis Testing Results.

Species	a/a_0	b/b_0
O_2	-	-
H^+	-	-
Cu^{2+}	-	-

of Frank-Kamenetskii, described at the outset of this chapter, provides the basis for comparing the data with a theoretical model.

This analysis suggests that diffusion of OH^- away from the surface of the electrode may be the rate controlling diffusion process in solution. It further suggests that the underlying rate process is also dependent on the surface concentration of OH^-, or surface pH, a result shown to be the case for both, oxide free and oxide covered electrodes earlier in Section 4.

The rate expression appropriate for region III is once again:

$$I = \left(\frac{nFD_{OH}\ p(10^{-3}\ k_w)^b}{10^{-6}\ \delta_D}\right) 10^{bpH_B}$$

From the regressed values of a and b at 25, 15, and 5°C the temperature dependence of b and p can be evaluated and a general rate expression developed which closely models the measured data at all three temperatures. Table 26 shows the numerical values of p and b at all three temperatures, along with their 95% confidence interval variations.

Figures 52, 53 and 54 show the precision with which the quantitative rate expressions fit the data for all three temperatures.

Data presented in this section were found to be largely under rate control by solution mass transport, in accord with experimental design. The rate limiting diffusing species has not been determined, although the field of possibilities has been reduced. The pH and temperature dependence of the data were characterized quite well by the diffusion of OH^- away from the electrode surface and it may very well be the rate limiting diffusing

Table 26. Parameter Estimates Calculated for Stagnant Diffusion Data

T	$b \pm \Delta b$	$p \pm \Delta p$
25	-0.109 ± .027	$2.313 \times 10^{-16} \pm 1.280 \times 10^{-16}$
15	-0.106 ± .076	$2.026 \times 10^{-17} \pm 1.523 \times 10^{-17}$
5	-0.111 ± .071	$1.547 \times 10^{-16} \pm 1.135 \times 10^{-16}$

species. To characterize this with more certainty will require a more rigorous accounting of all the reactions occurring at the oxide/solution interface. This should include the effects of copper cation complexation, $Cu(OH)_2$ precipitation, along with the effects of surface and solution buffer capacity.

DATA ANALYSIS SUMMARY

Several general observations can be made concerning the likelihood and importance of rate control by each of the component rate processes. First of all, a comparison of the magnitude of the three types of data as a function of pH, shown in Figures 55 and 56 at 25°C, show the following:

a) Corrosion rates measured at pH < 7.0 on electrodes without oxide films were much larger than those measured on oxide covered electrodes.

b) Corrosion rates measured in stagnant solution were considerably lower than those made at 3000 RPM.

These observations are significant in that they demonstrate both the influence of oxide film growth and solution mass transport on the overall rate and suggest that a model of the overall process include the coupled effects of these two rate processes. Kinetic data may be important but only at sites where the oxide film has been damaged or removed. The fact that solution mass transport control data were of smaller magnitude than the other two sets of data at corresponding pH and temperature values indicates tht there is

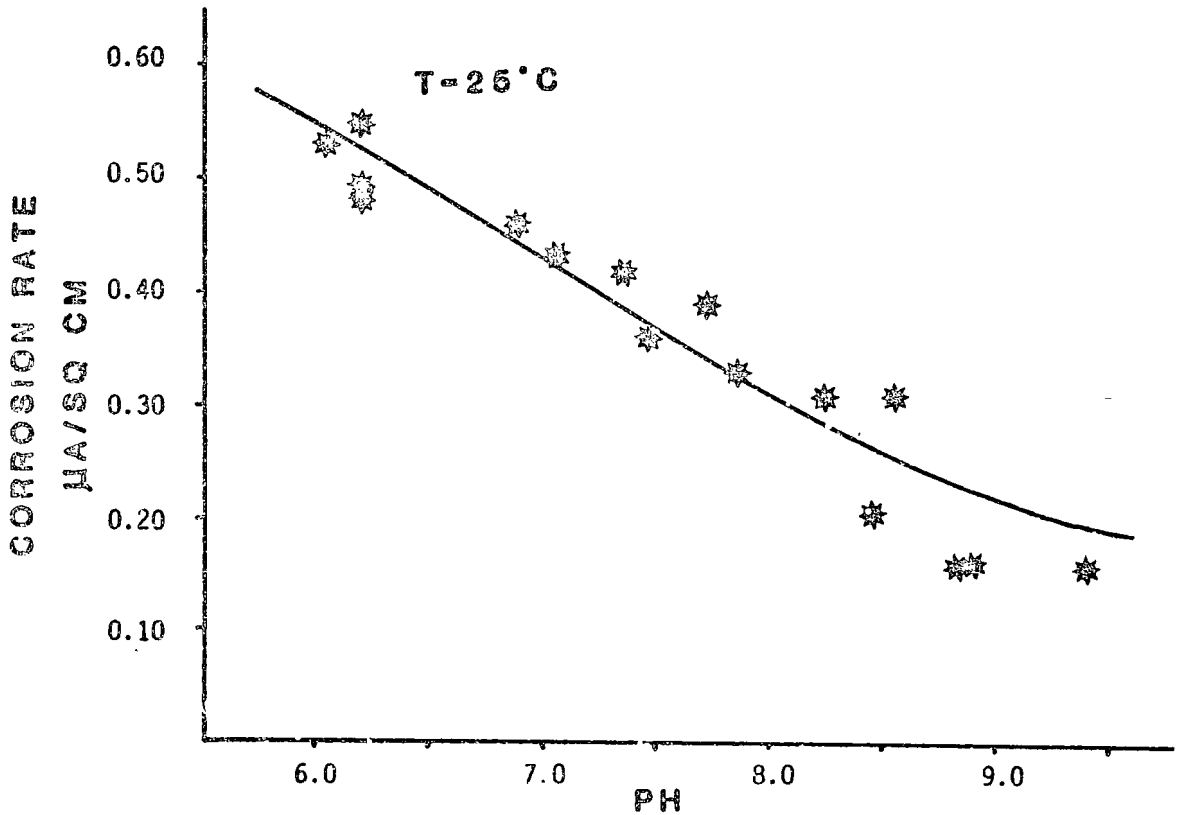

Figure 52. Stagnant diffusion data at 25°C.

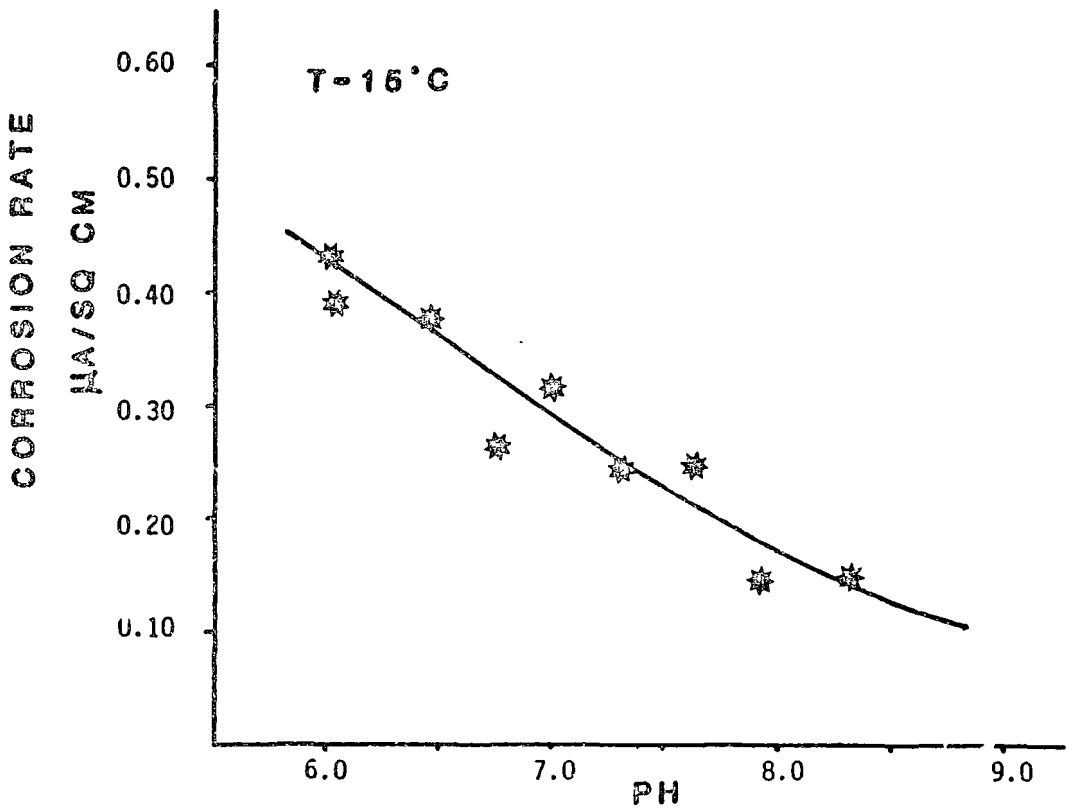

Figure 53. Stagnant diffusion data at 15°C.

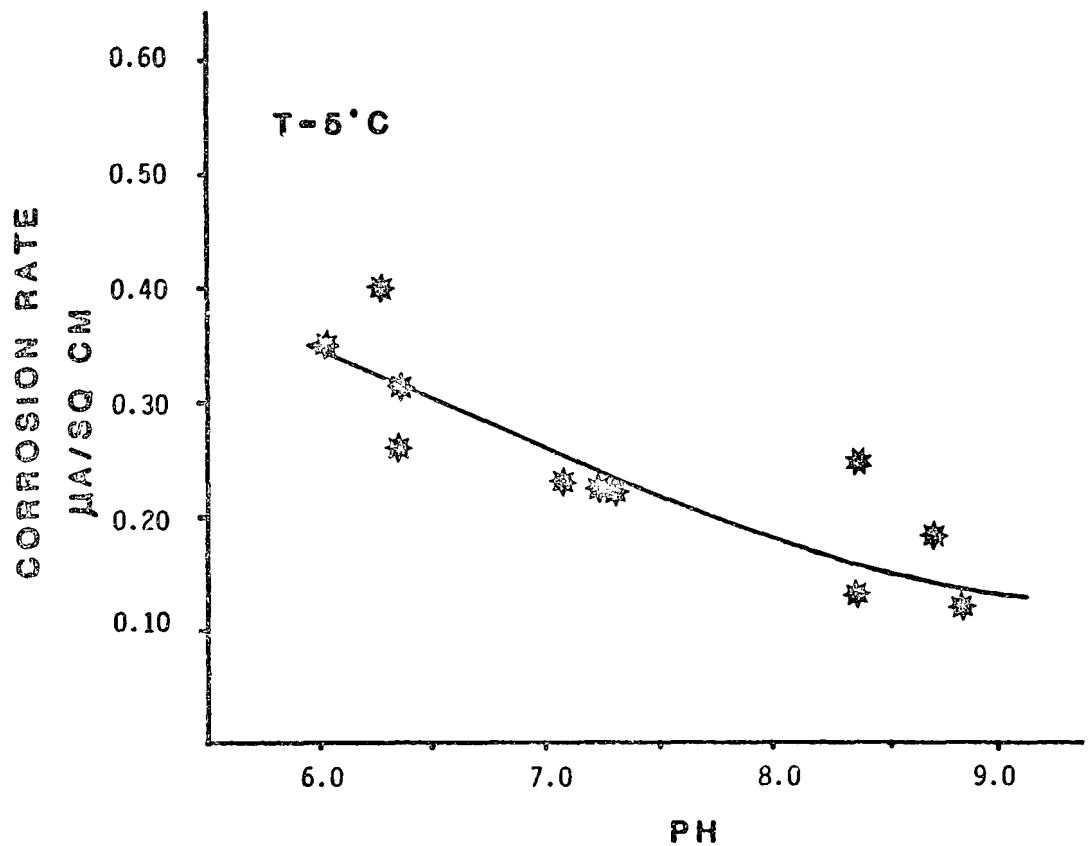

Figure 54. Stagnant diffusion data at 5°C.

some species in solution whose rate or diffusion effects the rate of the overall corrosion process.

The rate of the process therefore is dependent upon not only the chemical reactions involved and the growth of oxide film but also on the hydrodynamic flow regime of the corroding system, since it inevitably influences the rate of solution mass transport. There is a definite solution mass transport influence and the species exerting that influence may very well be OH^- diffusing away from the surface into bulk solution. This situation where a reaction product must diffuse away from the reaction site is characterized by a persistent influence on the overall rate of the process even at very high Reynolds Numbers to the point of masking the effects of the underlying process. The effect of a slow diffusion of OH^- away from the surface is to increase the pH of the solution adjacent to the oxide surface reducing the oxide film growth rate. As the diffusion rate is increased, at higher Re, the surface pH can drop allowing a faster rate of oxide film growth and greater corrosion rate. The high pH values that arise at the oxide surface may promote precipitation of such solids as $Cu(OH)_2$ which have low solubilities. This may even suggest that actual rate control of the corrosion process occurs in the solution adjacent to the oxide surface, not within or on the oxide itself. In addition a variety of $Cu(OH)_n^{2-n}$ complexes may form in the solution adjacent to the oxide surface reducing the "free OH^-" concentration, lowering the surface pH.

Empirical Characterization of pH_S

Data assigned to be under oxide film growth rate control and solution mass transport rate control were both, in reality, principally under rate control by diffusion of a reaction product away from the electrode surface. Assuming that the diffusing species to be OH^- it is possible to calculate the surface pH, pH_S, for each data point as follows:

$$pH_S = \log\left[\frac{\delta_D\, I}{C\, K_W} + 10^{pH_B}\right]$$

where: $I = \mu A/cm^2$

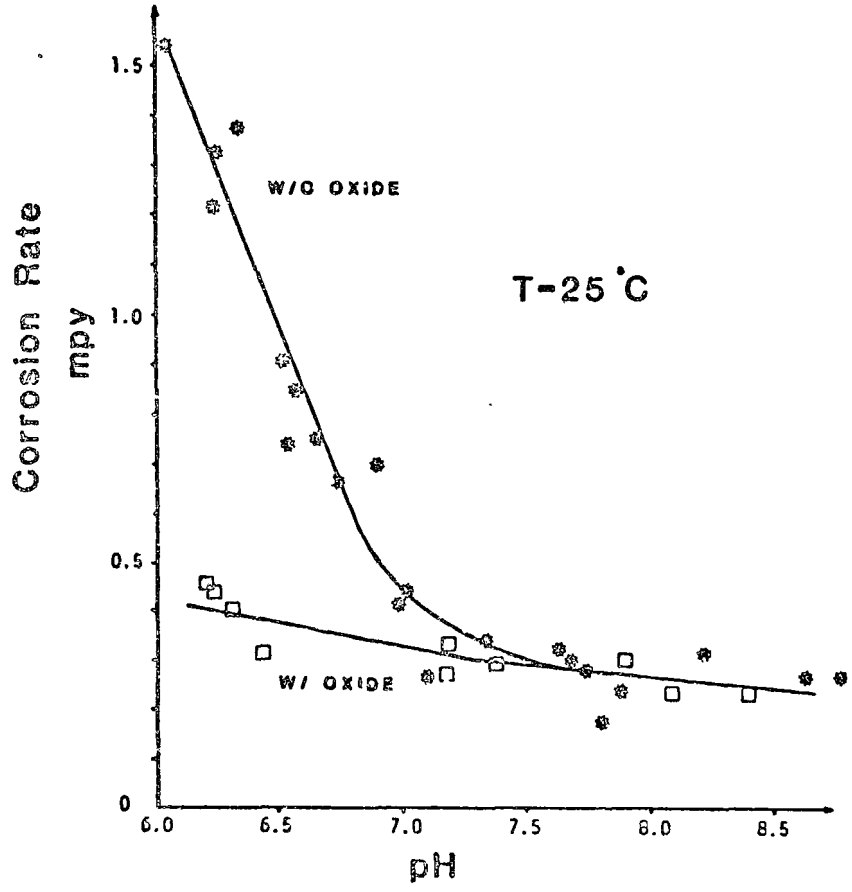

Figure 55. Comparison of Corrosion Rates Measured with and without Oxide Film at 25°C.

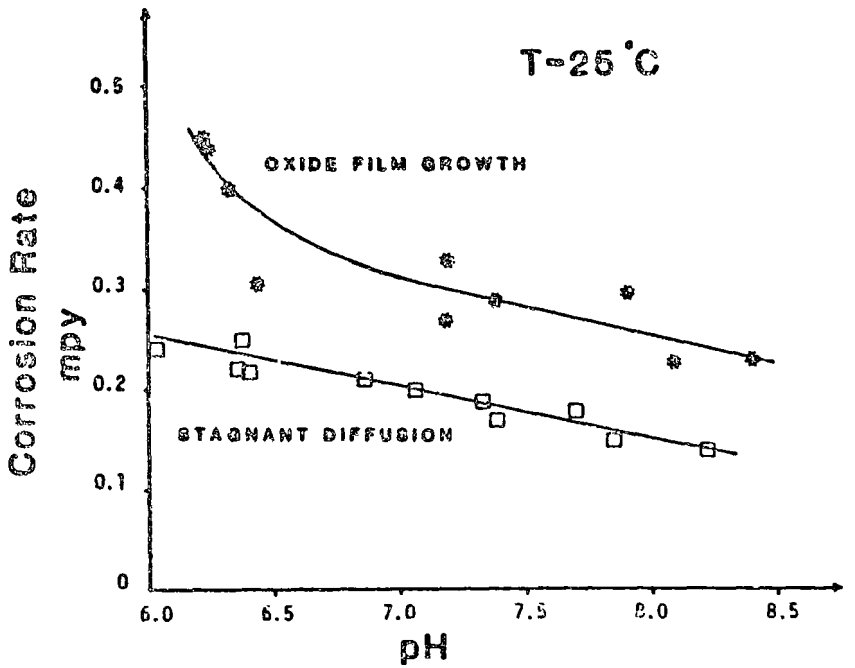

Figure 56. Comparison of Corrosion Rates Measured with and without Solution Mass Transport Effects at 25°C.

$$C = 10^3 \, nF \, D_{OH}$$

These values were calculated and included in Tables 15, 16, 17, 20, 21 and 22, for oxide film growth and solution mass transport data sets. These calculated values show that pH_S is dependent upon temperature, pH_B, and diffusion layer thickness, as one might expect. Since it wasn't possible to completely characterize mechanistically or quantitatively the underlying rate process accompanying OH^- mass transport in solution, the following empirical formulation was decided upon:

$$pH_B = f(T, pH_B, \delta_D)$$

It was apparent from looking at the two data sets at varied temperature, pH, and diffusion layer thickness that pH_S depended upon these three variables, in some fashion that couldn't a priori be modeled deterministically as earlier intended.

By writing pH_S in the general form of:

$$pH_S = K(pH_B)^{\alpha} \, T^{\beta} \delta_D^{\gamma}$$

and then taking $\log_{10}$ of both sides:

$$\log pH_S = \log K + \alpha \log pH_B + \beta \log T + \gamma \log \delta_D$$

a relationship for pH_S as a function of pH_B, T, and δ_D could be established by means of multiple linear regression. This regression could then include both oxide film growth and solution mass transport rate control data sets, a total of fifty-eight data points. When this was attempted it was found that the dependence on pH_B could not be properly characterized in this form although the T and δ_D dependence could be. So instead of pH_B, a new function, $\emptyset$, was used which was dependent only upon pH_B.

The functional form of $\emptyset$ was determined by regressing pH_S vs. pH_B data for oxide film growth to a third order polynomial and finding that a better fit was gained at all temperatures. This functional form of $\emptyset$ was used in regression with pH_S. The relationship for which log pH_S values were regressed was:

$$\log pH_S = \log K + \alpha \log \emptyset + \beta \log T + \gamma \log \delta_D$$

When all 58 data points were regressed in this form the following values for K, α, β, and γ were found:

$r = 0.948$

$K = 7.962 \times 10^3$

$\alpha = 0.333$

$\beta = -1.075$

$\gamma = .0328$

Using these regressed values the following quantitative form for pH_S results:

$$pH_S = (7.962 \times 10^3)\ \phi^{0.333}\ T^{-1.075}\ \delta_D^{.0328}$$

where: $\phi = 1.0 - 0.32\ pH_B + 0.039\ pH_B^2 - 0.0015\ pH_B^3$

T = absolute temperature (°K)

In this form variations in the data with respect to all three principal system variables are captured.

The goodness of fit of this function is shown in Figures 57, 58 and 59 for comparison with data at 25, 15 and 5°C respectively.

This regression equation, which incorporates solution pH, T, and δ_D, to predict the variations in pH_S, which must be estimated based on some of the same parameters, is an unsatisfactory modeling result. The importance of the pH at the interface is significant and is expected to have a controlling effect on the rate of the cathodic reaction, on Cu^+ oxidation and on precipitation of $Cu(OH)_2$, as well as determining the soluble copper hydroxide species. The regression equation does catalog the data in a form that predicts the estimated parameter, pH_S, within reasonable limits. The task of understanding and mechanistically modelng the interfacial reactions remains for future studies.

CONCLUSIONS

The finding that uniform copper corrosion in synthetic Tolt River water proceeds under rate control by solution mass transport of a reaction product, likely to be OH^-, is significant in providing direction for further research

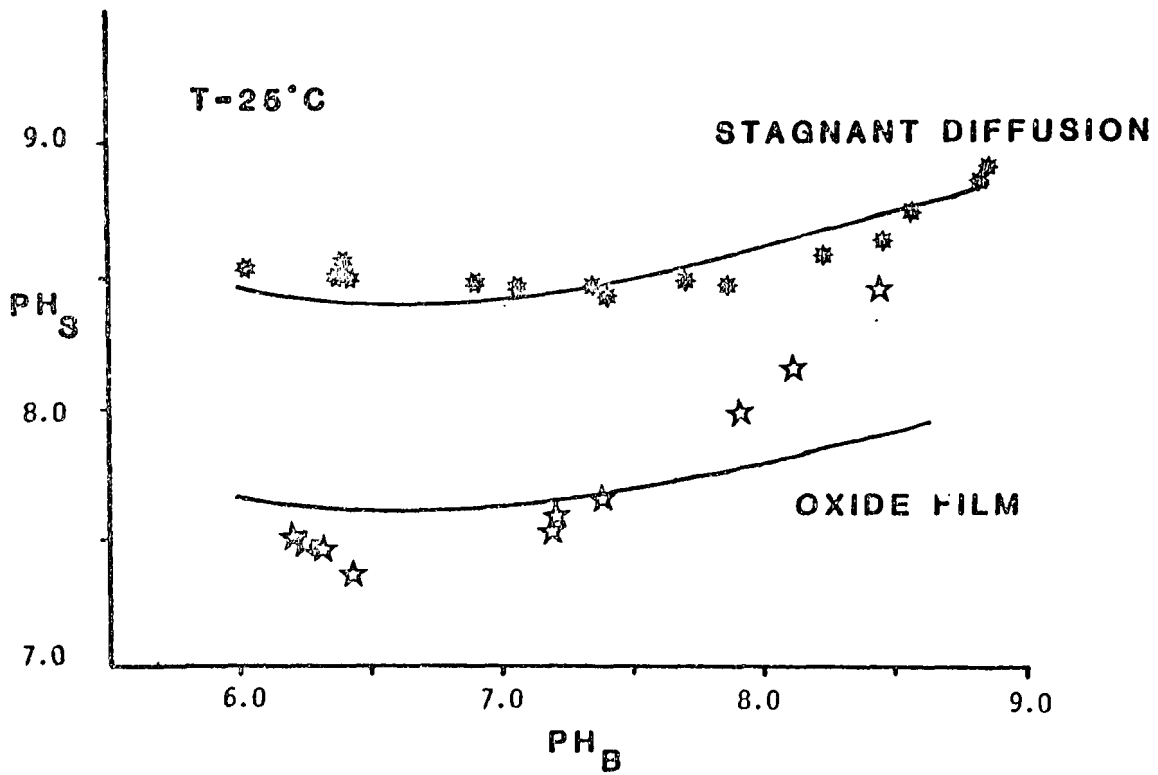

Figure 57. Comparison of surface pH values calculated from data with those predicted by empirical expression for surface pH at 25°C.

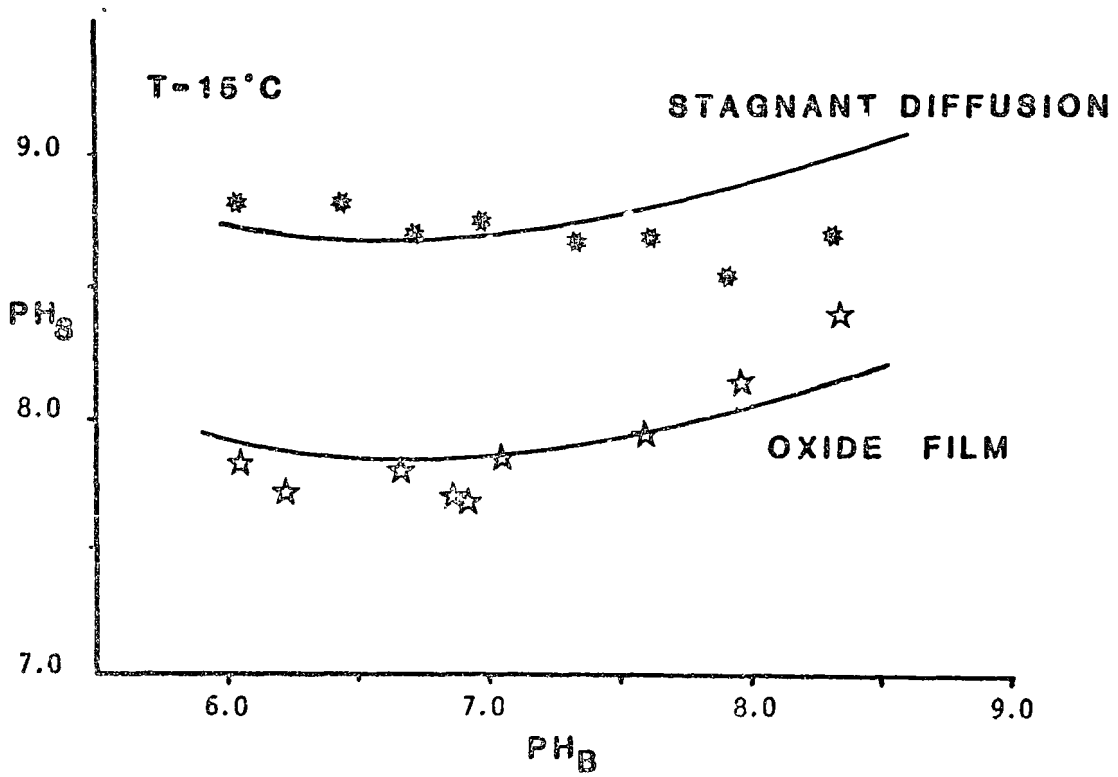

Figure 58. Comparison of surface pH values calculated from data with those predicted by empirical expression for surface pH at 15°C.

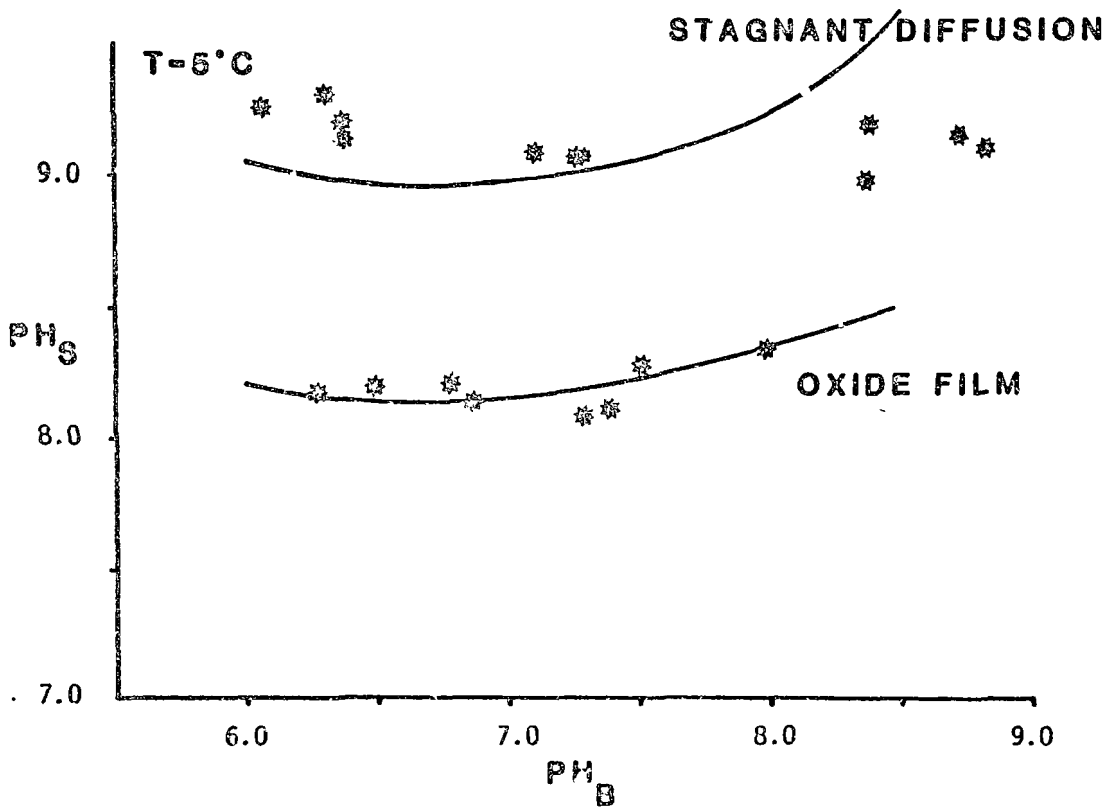

Figure 59. Comparison of surface pH values calculated from data with those predicted by empirical expression for surface pH at 5°C.

in copper corrosion in drinking water. The study of precipitation and complexation of dissolved copper species may prove to be the key to further understanding of the complexity of processes making up aqueous corrosion of copper. This finding has implications for other metals as well. Since OH^- is a product of the O_2 reduction reaction, a cathodic half-cell for almost all metal corrosion in aqueous solution of near neutral pH, its mass transport, complexation, and precipitation by metal cations present may be controlling the rate of other corroding systems.

SECTION 7

PROPOSED STEADY-STATE PIPE FLOW MODEL FOR UNIFORM COPPER CORROSION

INTRODUCTION

The use of copper tubing for cold water transport in households and commercial buildings is widespread. Problems arising from its accelerated corrosion have been outlined earlier. The principal value of corrosion research performed in the laboratory lies in its application to real life corroding systems, such as copper tubing used for cold water plumbing. In this chapter a simulation model is presented that allows one to predict the rate at which copper tubing will corrode under a given set of environmental conditions. It is developed based on the presumption that mass transport of OH^- is the rate controlling process and combined results of laboratory studies presented in Section 6 with quantitative models for mass transport in laminar and turbulent pipe flow presented in Section 4. The result is an ability to predict the rate of uniform copper corrosion in cold water plumbing systems under varied conditions of flow, temperature and pH of the water. Such a model can provide valuable insight into identification of principal variables affecting the overall process, the extent to which each variable exerts an influence, and the range of magnitude in which the maximum effect is manifested. Possible strategies for corrosion control, or at least corrosion rate reduction are also suggested.

RATE EXPRESSION DEVELOPMENT

To develop a mathematical model that predicts the changes in corrosion rate of copper due to variations in flow, temperature, and chemical composition of the water, the coupled effects of several rate processes need to be considered. As discussed earlier it is presumed that the cuprous oxide film covering the copper grows to some steady-state thickness where the rate of

film growth and the rate of film dissolution are equal. The following stoichiometric relationships were given for film growth and dissolution:

$$CU^{+1} + 1/2\ H_2O \longrightarrow 1/2\ Cu_2O + H^+ \quad \text{(film growth)}$$

$$1/2\ Cu_2O + H^+ \longrightarrow Cu^{2+} + 1/2\ H_2O + e^- \quad \text{(film dissolution)}$$

Both of these reactions occur at the oxide/solution interface and involve either the production or consumption of protons. When the rate of production of Cu_2O by the film growth reaction equals the rate of dissolution, or Cu_2O consumption, by the film dissolution reaction the net rate of proton production by these two reactions is zero. That is, the rate of H^+ produced in film growth is exactly offset by the rate of H^+ consumed in film dissolution.

The other reaction occurring at the oxide/solution interface is the molecular oxygen reduction reaction which has differing stoichiometry in acidic and alkaline solutions:

$$O_2 + 2H^+ + 2e^- \longrightarrow H_2O_2 \qquad \text{at pH} < 7.0$$

$$\text{and}\quad O_2 + 2H_2O + 4e^- \longrightarrow 4OH^- \qquad \text{at pH} \geq 7.0$$

Obviously there is net consumption of H^+ (or production of OH^-) involved in this reaction in both acidic and alkaline solutions. Therefore, it can be noted, that at the oxide/solution interface where film growth, film dissolution, and O_2 reduction all take place simultaneously an overall consumption of protons occurs regardless of the solution pH. The effect then of the corrosion reactions is a tendency to increase the pH of the solution adjacent to the oxide surface. How large the pH change is depends on the overall rate of O_2 reduction, the buffer capacity of the solution and oxide surface, and the rate of mass transport of OH^- away from the surface into bulk solution.

For a corroding copper system at steady-state film thickness, rate control was shown to be due principally to the persistent effect of mass transport in solution of a reaction product presumably OH^-. It was also influenced by the underlying rate process through its effect on pH_s. This overall

effect was captured by the empirical relationship derived for pH_s as a function of T, pH_B, and δ_D in Section 6:

$$pH_s = (7.9616 \times 10^3)\phi^{0.333} (273.0 + T)^{-1.075} \delta_D^{.0328}$$

where: $\phi = 1.0 - 0.32pH_B + 0.039\ pH_B^2 - 0.0015\ pH_B^3$

This expression for pH_s was found to best fit the 58 data points regressed and serves as an expression that catalogs the temperature, pH, and $_D$ dependence of the chemical process occurring at the interface. When used in conjunction with laminar and turbulent mass transport pipe flow models, uniform copper corrosion in those systems can be characterized. The rate expression used in the model here is that presented earlier in Table 4-5:

$$I(\mu a/cm^2) = \frac{nF\ D_{OH}}{10^{-6}\delta_D} [C_S - C_B]$$

Here C_s is the OH^- concentration in (moles/cm^3) in the solution adjacent to the surface and C_B is the bulk OH^- concentration, with the diffusion layer thickness, δ_D. The rate expression above can be rewritten in a form more suitable for use as follows:

$$I = \frac{C\ K_w}{\delta_D} [10^{pH_S} - 10^{pH_B}]$$

where: $C = 10^3\ nF\ D_{OH}$

$$\delta_D = \begin{cases} 0.5(\pi\ D_{OH}\ t)^{1/2} & \text{Stagnant Diffusion} \\ 1.453\left[\frac{\langle V_y \rangle}{y\ D_{OH}\ r}\right]^{-0.333} & \text{Laminar Diffusion (Re} \leq 2800) \\ 133.3r\ Re^{-0.88}\ Sc^{-0.333} & \text{turbulent diffusion (Re} > 2800) \end{cases}$$

$$pH_s = (7.9616 \times 10^3)\ \emptyset^{0.333}\ (273.0 + T)^{-1.075}\ \delta_D^{.0328}$$

$$\emptyset = 1.0 - 0.32\ pH_B + 0.039\ pH_B^2 - 0.0015\ pH_B^3$$

These relationships constitute the proposed steady-state pipe flow model for uniform copper corrosion. As mentioned earlier they are a combination of results of this research with results presented in the literature for solution mass transport in pipe flow. These equations are easily programmed on a digital computer. Corrosion rate estimates, computed in this fashion, are presented for flow in a circular pipe of one-half inch diameter. Numerical values for C, Kw, and D are provided in Table 27 at 5, 15, and 25°C.

Table 27. Pipeflow Model Parameter Values

	T = 25°C	T = 15°C	T = 5°C
C	5.076×10^3	3.841×10^3	2.798×10^3
K_w	1.01×10^{-14}	0.45×10^{-14}	0.18×10^{-14}
S_c	171.1	276.4	519.0
δ_D (Lam.)	$2.146\ Re^{-0.333}$	$Sc^{-0.333}$	
δ_D (Turb.)	$84.646\ Re^{-0.88}$	$Sc^{-0.333}$	

The diffusion layer thickness, δ_D, depends on the Reynolds number, Re, and the Schmidt Number, S_c, the pipe radius, r, and for laminar flow the distance down the axial length of the pipe from its inlet, y. Results presented below are calculated using a pipe radius of 1/2 inch and an axial distance of 4.0 cm from the pipe inlet. The Reynolds Number for pipe flow is defined as:

$$Re = \frac{d\langle v_y \rangle}{\nu}$$

where d is the inside pipe diameter (cm), $\langle v_y \rangle$ the mean solution velocity in the direction parallel to the corroding surface ($\langle v_y \rangle$ = A/Q cm^2/sec), and ν is the kinematic viscosity of the solution in (cm^2/sec). The Schmidt Number is defined as follows:

$$Sc = \frac{\nu}{D_{OH}}$$

with both ν and D_{OH} being temperature dependent. For known conditions of T, pH_B, and δ_D values of pH_s and corrosion rate can be calculated.

RANGE OF APPLICATION OF PIPE FLOW MODEL

The range of application of the pipe flow model is limited in two respects. First, for the model to be valid the corrosion process must be completely or at least partly controlled by the rate of solution mass transport of OH^-. The rate expression used in the model presumes this. Second, the corroding system must be operating within the range of values of pH_B, T, and δ_D over which data was taken and used in determination of the empirical relationship for pH_s. Each of these constraints exerts some influence on the overall spectrum of usage but neither turn out to be overly limiting. The only data found not to be at least partly under rate control by solution mass transport (Region I), occurred at very high pH (pH > 8.5). Under these circumstances, the underlying rate process be it oxide film growth or an interfacial reaction, completely controls the rate of corrosion. At pH values of 8.5 and below the data showed a persistent influence of solution mass transport of OH^-.

The second constraint places limits on pH, T and δ_D due to the range of variation of these parameters exhibited by the data used to generate the empirical relationship for pH_s. The regressed relationship for pH_s is not a good fit to the data at T = 25°C, 3000 RPM (oxide film data), and $pH_B > 7.5$ and underestimates pH_s by as much as 0.5 pH units at $pH_B = 8.5$. At 15°C and 3000 RPM the regressed relationship for pH_s once again underestimates pH_s at $pH_B > 8.0$. Overall the regressed relationship for pH_s fits the data reasonably well for $pH_B < 7.5$ at all temperatures and values of diffusion layer thickness tested. Data taken was limited to the following range in parameter values:

$$6.0 \leq pH \leq 8.5$$

$$5 \leq T \leq 25°\ C$$

$$1.385 \times 10^{-5} \leq \delta_D \leq 3.375 \times 10^{-6} \quad cm$$

Since the first constraint was met, universally at pH < 8.5 the limitations set by the second constraint are in general the controlling conditions. These limitations being the range of parameter values shown above modified to exclude regions of poor goodness of fit of the regressed relationship for pH_s. Care should be taken in interpretation of corrosion rate predictions under conditions near or beyond these limits. Extrapolation to pH values less than 6.0 seems justified since the first constraint is met, but extrapolation beyond pH = 8.5 is not justified.

RESULTS OF PIPE FLOW MODEL

Corrosion rate estimates have been calculated using the pipe flow model for a wide range of temperature, pH_B, and flowrate values. Some presented values correspond to areas outside the range of safe application outlined in the last section. Of note, are conditions at high flowrate (Re > 10000) and high pH_B (pH > 8.0). Here the model predicts corrosion rates that rapidly approach zero as either pH_B or Re is increased, a tendency that is not in accord with experimental results. This occurs when the regressed expression for pH_s underestimates its actual value, causing the term:

$$[10^{pH_S} - 10^{pH_B}]$$

to be substantially reduced in value and approach zero. This same effect occurs when the overall rate is either being significantly influenced by or completely controlled by the rate of the underlying rate process. As Re is increased the transition from solution mass transport rate control to rate control by the underlying rate process occurs at a lower pH_B. The diffusion layer thickness produced by a rotating disc electrode at 3000 RPM corresponds to diffusion layer thicknesses produced in turbulent pipe flow at the following Reynolds Numbers:

Re = 34,500	at	T = 25°C
Re = 30,750	at	T = 15°C
Re = 25,800	at	T = 5°C

At higher Reynolds Numbers the transition in rate control begins to occur at $7.5 \leq pH_B \leq 8.5$.

In calculating rates for presentation in Figures 60 through 64 the proposed model gave some estimates that rapidly approached zero at high Reynolds Numbers. When this occurred the values presented are those predicted at the same pH_B and T, but at a lower Re. These estimates are drawn with broken lines. This is a reasonable approximation since an increase in solution mass transport rate, as signified by an increase in Re, should not decrease the overall rate but at a minimum allow it to remain unchanged in the limit where the rate of the underlying rate process completely controls the overall rate. In Figure 60 corrosion rate, in mils per year, is plotted verus Log Re at 25°C over a range in flowrate that includes both laminar and turbulent flow. Corrosion rates estimated at low flowrates (laminar flow regime) range between 0.50 and 0.20 MPY with the major rate changes occurring between pH = 5.0 and pH = 6.0. At high flow rate (turbulent flow regime) corrosion rate estimates range between values greater than 1.0 and 0.2 MPY with significant rate reductions occurring as pH is increased above 7.5.

A plot similar to that described above is given in Figure 61 for pipe flow at 15°C. Corrosion rate estimate at low flowrate varied between 0.4 and 0.20 MPY with the major changes occurring between pH = 5.0 and 5.5. At high flowrate, corrosion rate estimates range from 0.8 MPY at pH 5.0 to 0.2 MPY at $pH \geq 8.0$ down slightly from the corresponding rate estimates at 25°C.

The combined effects of pH and flowrate on the rate of copper corrosion at 5°C are shown in Figure 62. Corrosion rate estimates at low flowrates range from 0.28 to 0.20 MPY at pH < 5.5 but at higher pH_B are effectively independent of pH_B at a value of 0.16 MPY, a slightly lower value than high pH estimates at 15 and 25°C. At high flowrate, corrosion rate estimates vary from 0.80 MPY at pH 5.0 down to 0.20 MPY at pH 8.5. Once again showing slightly lower values than corresponding estimates at higher temperatures. Looking at these three plots of corrosion rate estimates it is obvious, as was mentioned above, that the effects of pH and temperature on corrosion rate are considerably different at low flow rates than at high flowrates. At low flowrate (RE < 1000) as shown in Figure 63, there is only a dependence on pH_B at pH < 6.0, and only a minimal temperature dependence. Above pH = 6.0

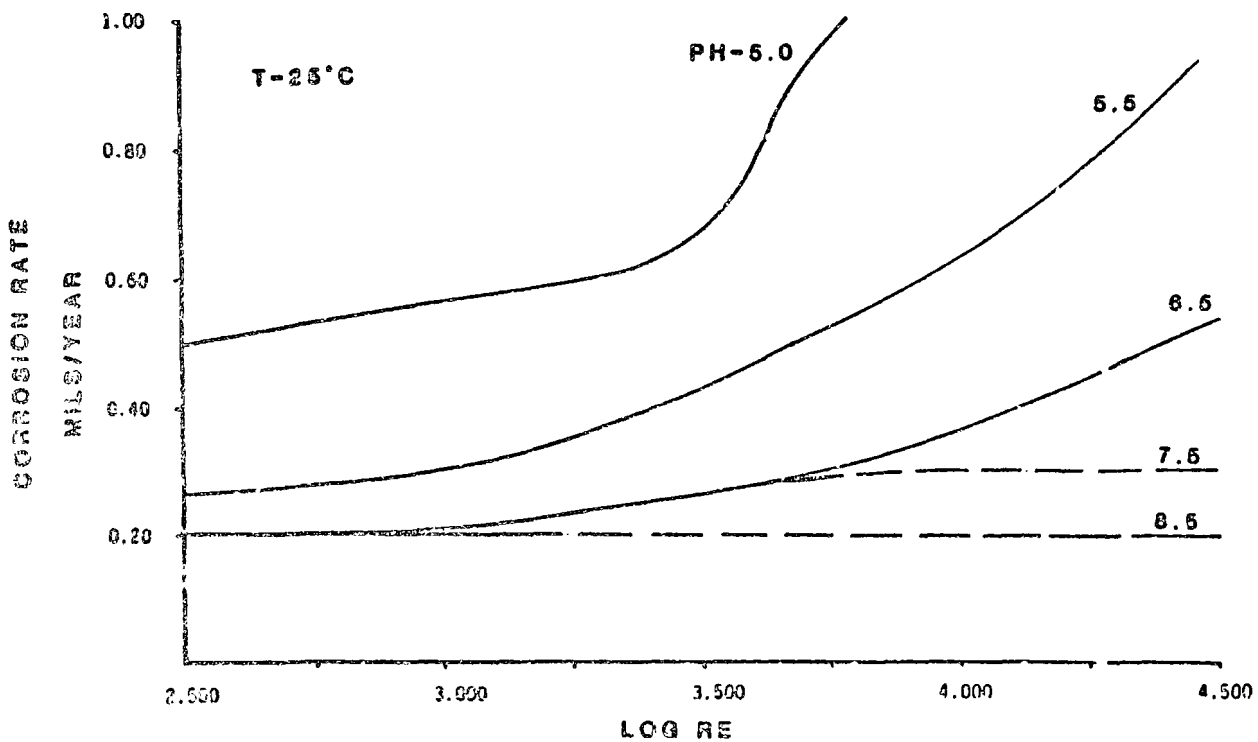

Figure 60. Corrosion rate estimates for 1/2 inch copper tubing at varied flowrate and 25°C.

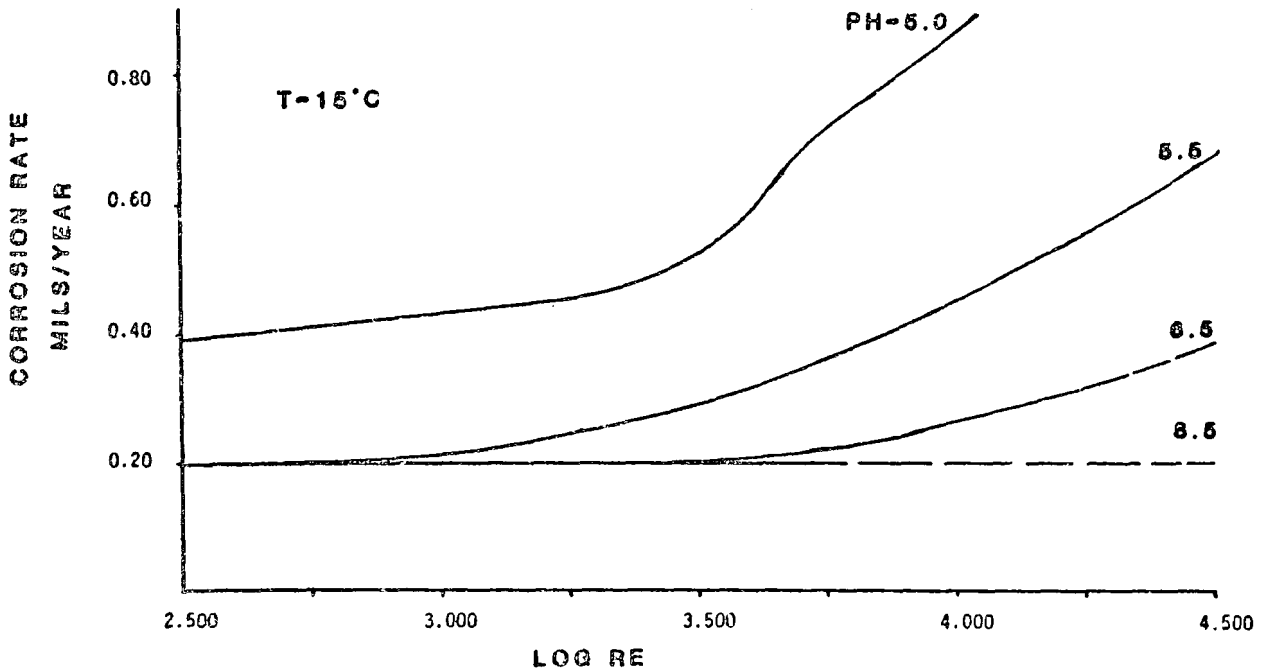

Figure 61. Corrosion rate estimates for 1/2 inch copper tubing at varied flowrate and 15°C.

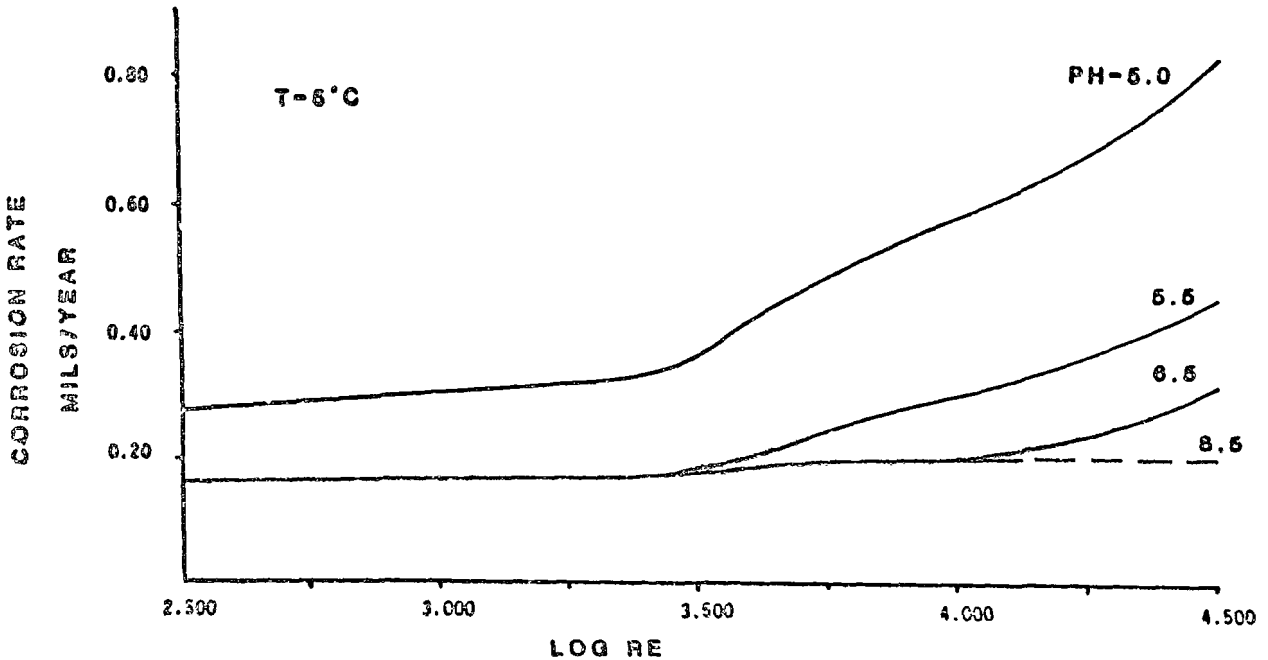

Figure 62. Corrosion rate estimates for 1/2 inch copper tubing at varied flowrate and 5°C.

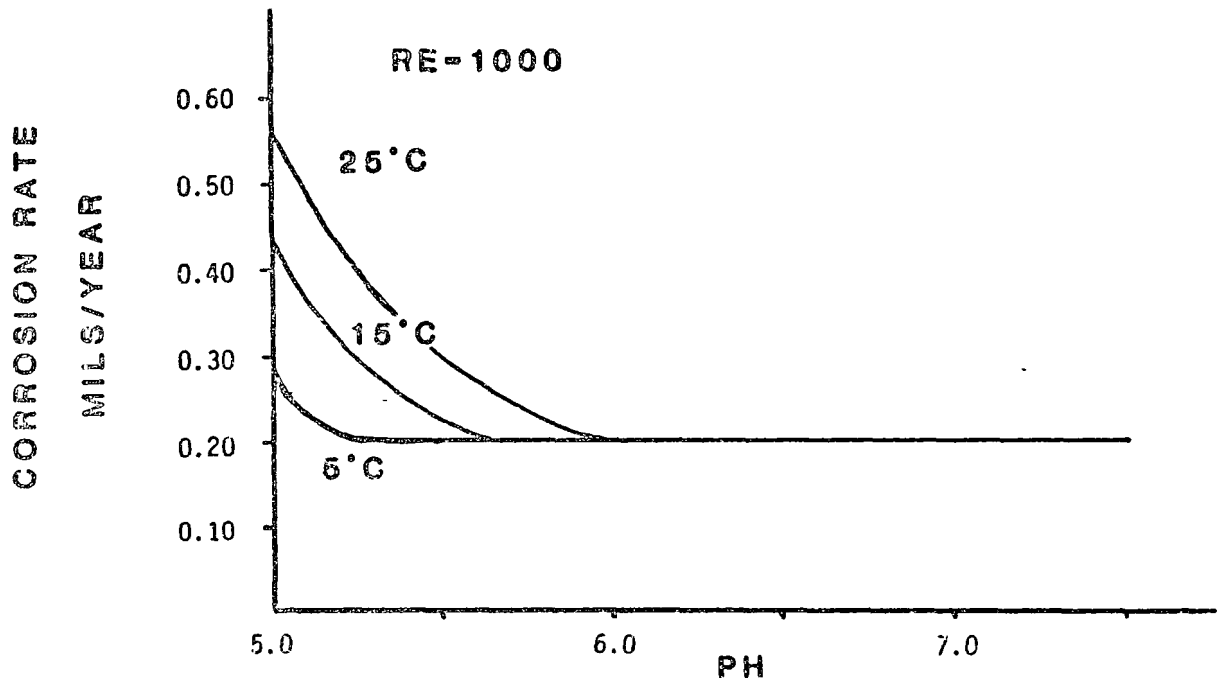

Figure 63. pH dependence of corrosion rates estimated for laminar flow conditions.

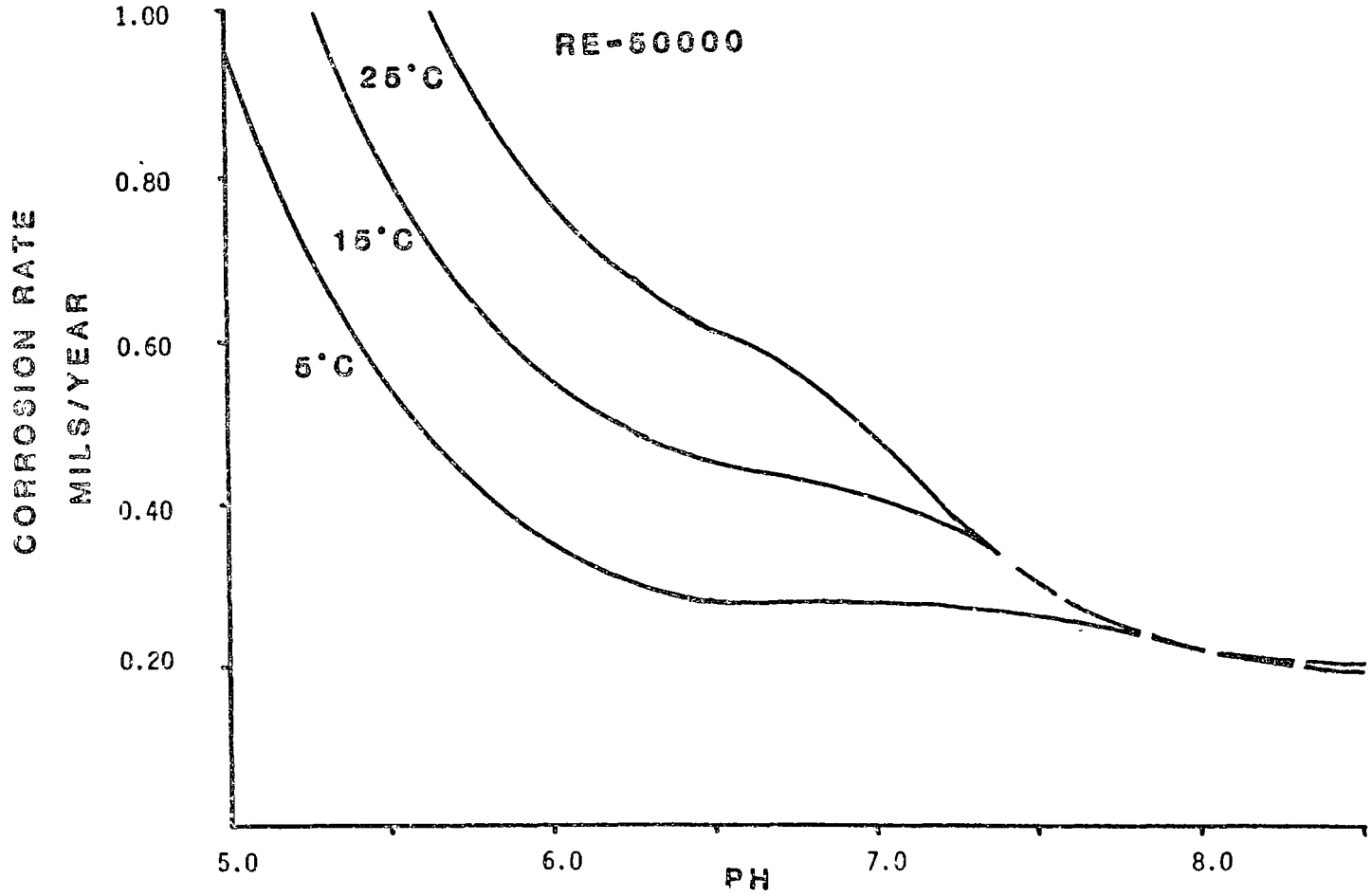

Figure 64. pH dependence of corrosion rates estimated for turbulent flow conditions.

corrosion rate estimates are consistently less than 0.25 MPY, where 0.3 MPY is sometimes considered the maximum desirable corrosion rate for copper in drinking water. At high flowrates (Re = 50,000) corrosion rates can increase dramatically. Figure 64 is a plot of corrosion rate versus pH_B at 5, 15, and 25°C and Re = 50,000. It shows some interesting results. At low pH_B (pH_B < 7.0) both flowrate and temperature exert significant influence on predicted rates. The combination of low pH_B and high temperature give the most unfavorable situation with rates increased as much as 500% over rates predicted under comparable conditions at low flowrate. This effect is lessened greatly as pH_B is increased to a value above 7.0. In fact, for pH_B > 8.0 the accelerating effects of temperature, flowrate, and pH_B are essentially eliminated.

MODEL VERIFICATION

The accuracy with which the proposed model predicts corrosion rates under specified environmental conditions can only be tested by comparison with independently measured field data. Ideally, field data would be available over the entire range of pH_B, temperature, and flowrate desired and the model could be tested over its entire range of desired use. Although much field data exists on copper corrosion in Tolt River Water, most of it was taken in the presence of a chlorine residual. Since chlorination has a big impact on corrosion rate (3, 4) but was not considered in the development of this model, data taken at a nonzero chlorine residual is not considered. A small amount of field data is available, at present for limited model verification. Data taken in studies conducted by the Seattle Water Department (1, 2) are presented here and compared with model predictions. Corrosion rates were measured by weight loss of copper coupons mounted in a pipe flow test loop. Since data presented were taken at different flowrates and temperature,some standardization was required for comparison. For each field datum presented a model prediction corresponding to the same environmental conditions was calculated. The ratio of measured rate to predicted rate is then used as a goodness of fit criteria. When this ratio equals 1.0 the model perfectly fits the data. Deviations from 1.0 are a measure of the inability of the model to predict measured values. Data values along with predicted model values are presented in Table 28. Over the range of pH_B com-

Table 28. Data for Verification of Pipe Flow Model.

pH_B	T(°C)	Pipe diam. (in)	Flow	Re	Corrosion Rate Measured (MPY)	Corrosion Rate Predicted (MPY)	a/b	Reference
6.7	9	1.0	0.45 gal/min	6927	0.14	0.18	0180	1
6.55	9	1.0	0.45 gal/min	6927	0.18	0.18	1.00	1
6.7	9	1.0	0.45 gal/min	6927	0.18	0.18	1.00	1
6.6	12	1.0	0.25 ft/sec	1760	0.15	0.20	0.85	2
6.7	12	1.0	0.25 ft/sec	1760	0.15	0.20	0.75	2
6.7	12	1.0	0.25 ft/sec	1760	0.14	0.20	0.70	2
6.0	12	1.0	0.25 ft/sec	1760	0.29	0.27	1.07	2
6.0	12	1.0	0.25 ft/sec	1760	0.35	0.27	1.29	1

pared ($6.0 \leq PH_B \leq 6.7$) Figure 65 shows the reasonably good predictions afforded by the pipe flow model. Thorough verification of this model, however, must wait until adequate field data is available for comparison over the full range of pH_B, temperature and flowrates desired.

CONCLUSIONS

A steady-state pipe flow model for uniform copper corrosion in Tolt River water has been developed in this chapter. It is proposed for use in determining optimum environmental conditions favorable to a reduced rate of corrosion of copper tubing used for cold water transport of Tolt River water. The model is developed based on the presumption that mass transport of OH^- away from the corroding surface controls the rate of the overall process, a presumption that seems well founded in light of results reported in Section 6. Predicted values compared favorably with field data and show explicitly individual effects of pH, temperature and flowrate on the overall rate of corrosion.

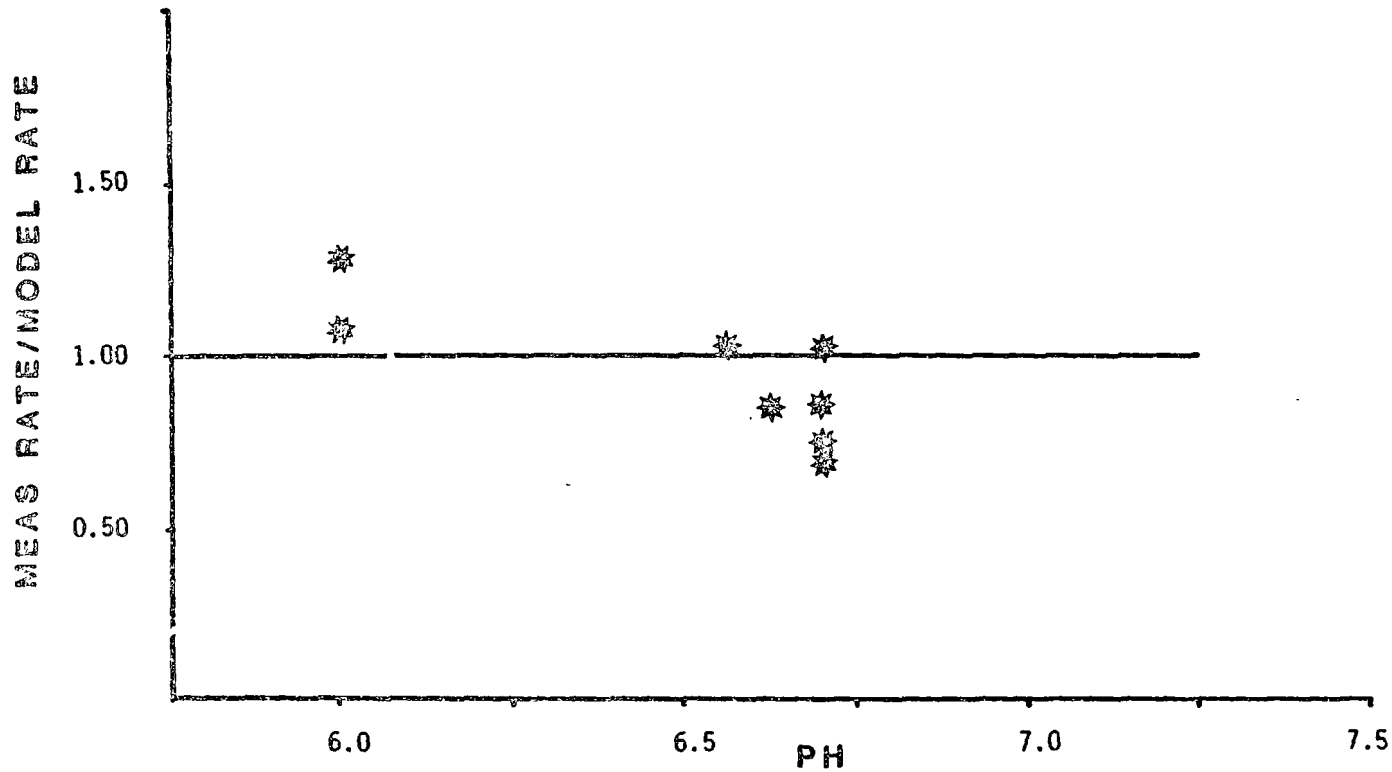

Figure 65. Comparison of copper corrosion rates predicted by pipe flow model with rates measured by independent sources.

REFERENCES

SECTION I

1. Economic Effects of Metallic Corrosion in the United States, Part I, NBS, Special Publication 511-1, L.H. Bennett et al. eds. May, 1978.

2. Economic Effects of Metallic Corrosion in the United States, Part 2, NBS Special Publication 551-2, J.H. Payer et al., eds. May, 1978.

3. Hudson, H.E. and Gilcreas, F.W. Health and Economic Aspects of Water Hardness and Carrosiveness, Journal AWWA, 68, 201, 1976.

4. Cotruvo, Joseph A. EPA Policies to Protect the Health of Consumers of Drinking Water in the United States, in Water Supply and Health, H. Van Lelyveld. Ed. Elsevier, N.Y., 1981. p. 345.

5. Quality Goals for Potable Water, Journal AWWA, 60, 1317, 1968.

6. Singley, J.E. Principles of Corrosion, in Proceedings of AWWA Seminar on Controlling Corrosion Within Water Systems, Atlantic City, NJ, June 25, 1978.

7. Sussman, S. Implication of the EPA Proposed National Secondary Drinking Water Regulation on Corrosivity, in Proc. AWWA Seminar on Controlling Corrosion Within Water Systems, Atlantic City, NJ, June 25, 1978.

8. Courchene, J. and Kirmeyer, G. Seattle Internal Corrosion Control Plan - Summary Report, in Proc. AWWA Seminar on Controlling Corrosion Within Water Systems, Atlantic City, NJ, June 25, 1978.

9. Larsen, T.E. and Sollo, F.W. Loss in Water Main Carrying Capacity, Journal AWWA, 59, 1565, 1967.

SECTION II

1. Ives, D.J.G. and Rawson, A.E. Copper Corrosion I: Thermodynamic Aspects, J. Electrochem. Society, 109, 447, 1962.

2. Ives, D.J.G. and Rawson, A.E. Copper Corrosion II: Kinetic Studies, J. Electrochem. Soc., 109, 452, 1962.

3. Ives, D.J.G. and Rawson, A.E. Copper Corrosion III: Electrochemical Theory of General Corrosion, J. Electrochem. Soc., 109, 458, 1968.

4. Ives, D.J.G. and Rawson, A.E. Copper Corrosion IV: The Effect of Saline Additions, J. Electrochem. Soc., 109, 462, 1962.

5. Hoare, J.P. The Electrochemistry of Oxygen, Wiley Interscience 1968, Chaps. 4 and 9.

6. Damjanovic, A. Mechanistic Analysis of Oxygen Electrode Reactions, in Modern Aspects of Electrochemistry, Vol. 8, 1973.

7. Damjanovic, A. Continued Growth of Anodic Oxide Films on Platinum and the Mechanism and Catalysis of Oxygen Evolution, in Nat. Bur. of Stds. Special Publication 455, Electrocatalysis on Non-Metallic Surfaces, Nov., 1976.

8. Yeager, Earnest. Mechanisms of Electrochemical Reactions on Non-Metallic Surfaces, in National Bureau of Standards Special Publication 455 Electrocatalysis on Non-Metallic Surfaces, Nov. 1976.

9. Smyrl, William H. Electrochemistry and Corrosion on Homogeneous and Heterogeneous Metal Surfaces, in Comprehensive Treatise of Electrochemistry, Vol. 4: Electrochemical Materials Science, Plenum Press, 1981, p. 97.

10. Fromhold, A.T. Theory of Metal Oxidation, Volume 1- Fundamentals, North Holland Publishers, 1976.

11. Vetter, K.J. Electrochemical Kinetics: Theoretical and Experimental Aspects, Academic Press, 1967.

12. Fromhold, A.T. and Cook, E.L. Kinetics of Oxide Film Growth on Metals: Electron Tunnelling and Ionic Diffusion, in Physical Review, 158, 600 (1967).

13. Mott, N.F. The Theory of the Formation of Protective Oxide Films on Metals - III, Transactions of the Faraday Society, 43, p. 429, 1947.

14. Cabrera, N. and Mott, N.F. Theory of the Oxidation of Metals, Reports on Progress in Physics, 12, p. 163, 1948-9.

15. Simmons, J.G., "Electric Tunnel Effect Between Dissimilar Electrodes Separated by a Thin Insulating Film," Journal of Applied Physics, 34, 2581, 1963.

16. Gibbs, D.B. Anodic Films on Copper and Silver in Alkaline Solution, Ph.D. Thesis, University of Toronto, 1968.

17. Simmons, John G. Generalized Formula for the Electric Tunnel Effect Between Similar Electrodes Separated by a Think Insulating Film, Journal of Applied Physics, 34, 1793, 1963.

18. Newman, John. The Fundamental Principles of Current Distribution and Mass Transport in Electrochemical Cells, in Electroanalytical Chemistry, Vol. 4, A.J. Bard, ed., 1968. Marcel Dekker, Inc.

19. Pickett, D.J. Electrochemical Reactor Design, Elsevier Press, 1979.

20. Crank, J. Mathematics of Diffusion, 2nd Ed., Clarendon Press, 1975.

21. Levich, V.G. Physicochemical Hydrodynamics, Prentice-Hall, Inc., 1962.

22. Denn, M.M. Process Fluid Mechanics, Prentice-Hall, Inc., 1980.

23. Schlichting, H. Boundary Layer Theory, 6th Ed., McGraw Hill Publisher, 1968.

24. Newman, J. Electrochemical Systems, Prentice-Hall, Inc., 1973.

25. Graetz, L. Ueber die Warmeleitungsfahigkeit von Flussigkeiten, Annalen der Physik und Chemie, 18, 79, 1883; und 25, 337, 1885.

26. Leveque, M.A. Les Lois de la Transmission de Chaleur par Convection, Annales des Mines, Memoires, 12, 201, 1928.

27. Linton, W.H., Sherwood, T.K. "Mass Transfer from Solid Shapes to Water in Streamline and Turbulent Flow," Chem. Eng. Progress, 46, p. 258, 1950.

28. Van Shaw, P., Reiss, L.P., Hanratty, T.J. "Rates of Turbulent Transfer to a Pipe Wall in the Mass Transfer Entry Region," A.I.Ch.E. Journal, 9, p. 363, 1963.

29. Chung, B.T.F. and Pang, Yuan. A Model for Mass Transfer in Turbulent Pipe Flow With a First-Order Chemical Reaction, Proc. of the 1980 Heat Transfer and Fluid Mechanics Institute, Stanford Univ. Press, 1981, p. 64.

30. Davies, J.T. Turbulence Phenomena, Academic Press 1972.

31. Chilton, T.H. and Colburn, A.P. Mass Transfer (Absorption) Coefficients. Prediction from Data on heat Transfer and Fluid Friction, Industrial and Engineering Chemistry, 26, 1183, 1934.

32. Harriot, P. and Hamilton, R.M. Chem. Eng. Sci., 20, 1973, 1965.

33. Adams, R.N. Electrochemistry at Solid Electrodes, Marcel Dekker, Inc., 1969.

34. Sherwood, T.K., Pigford, R.L., and Wilke C.R. Mass Transfer, McGraw Hill, 1975.

35. Soos, Z.G. Lingane, P.J. "Derivation of the Chronoamperometric Constant for Unshielded, Circular, Planar Electrodes", J. Phys. Chem. 68, p. 3821, 1964.

36. Lingane, P.J. "Chronopotentiometry and Chronoamperometry with Unshielded Planar Electrodes." Anal. Chem, 36, p. 1723, 1964.

37. Cornet, I., Banington A.E., and Behrsing G.U. "Effect of Reynolds Number on Corrosion of Copper By Sulfuric Acid", J. Electrochem. Soc. Oct. 1961 p. 947.

38. Frank-Kamenetskeii, D.A. Diffusion and Heat Transfer in Chemical Kinetics, Plenum Press 1969.

39. Roberts, K.J. Schemilt, L.W. "Strain Effects in the Corrosion of Copper in a Flowing Electrolyte", Trans. Inst. Chem. Engr., 47, T204 (1969).

40. Zembura, Z. "Relationship Between Metallic Corrosion and Limiting Current Using the Rotating Disc Method," Corrosion Science, 8, p. 703, 1968.

41. Zembura, Z. and Fulinski, A. "Rotating-Disk Investigations of Kinetics of Metal Dissolution: Case of Two Independent Dissolution Reactions", Electrochimica Acta, 10, p. 859, 1965.

SECTION III

1. Skeld, R.V. Larsen, T.E.D "Measurement of the Instantaneous Corrosion Rate by Means of Polarization Data", Corrosion, 13, 69, 1957.

2. Baboian, R. "Electrochemical Techiniques for Corrosion," Nat. Soc. for Corrosion Engrs. (NACE), 1977.

3. Mansfeld, F. "Polarization Resistance Technique for Measuring Corrosion Currents", Advances in Corrosion Science and Technology, Vol. 6, 1976 Plenum Press.

4. Stern, M, Geary, A.L. "Electrochemical Polarization I. A Theoretical Analysis of the Shape of Polarization Curves", J. Electrochem. Soc., 104, p. 56, 1957.

5. Barnartt, S. "Two-Point and Three Point Methods for the Investigation of Electrode Reaction Mechanisms," Electrochimica Acta, 15, p. 1313, 1970.

6. Barnartt, S. "Electrochemical Nature of Corrosion," in Electrochemical Techniques for Corrosion, NACE, 1977. p.1.

7. ASTM 65-71, Standard Reference Method in Making Potentiostatic and Potentiodynamic Anodic Polarization Measurements. Part 31, p. 1047, 1971.

8. Levich, V.B. Physicochemical Hydrodynamics Prentice-Hall 1962

9. Schlichting, H. Boundary Layer Theory, 6th Ed. McGraw-Hill 1968

10. Pleskov, Y.V. and Filinovskii, V.Y. The Rotating Disc Electrode Consultants Bureau, Plenum Press 1976.

11. "Laboratory Corrosion Testing of Metals for The Process Industries", NACE Standard TM-01-69 (1976 Revision) National Association of Corrosion Engineers 1976.

12. "Standard Recommended Practice for Preparing, Cleaning, and Evaluating Corrosion Test Specimens", ANSI/ASTM G-1-72 (Reapproved 1974) Amer. Soc. for Testing of Materials, 1979.

13. "Identification of Corrosion Products on Copper and Copper Alloys", NACE Publication 3B159, Nat. Assoc. of Corrosion Engrs., 1962.

SECTION IV

1. D.A. Frank-Kamenetskii, Diffusion and Heat Transfer in Chemical Kinetics, 2nd Ed. Plenum Press, 1969.

2. V.G. Leuich, Physicochemical Hydrodynamics, Prentice-Hall, 1962.

3. Y.V. Pleskov and V.Y. Filinovskii, The Rotating Disc Electrode, Plenum Press (Consultants' Bureau), 1976.

4. Bondart, Michel. Kinetics of Chemical Processes, Prentice-Hall, 1968. Englewood Cliffs, NJ.

5. Kennedy, J.B. and Neville, A.M. Basic Statistical Methods for Engineers and Scientists, 2nd Ed., IEP New York, 1976.

SECTION V

1. Hoyt, Brian P. "SWD Field Corrosion Testing 1972-1973 Data Summary" Seattle Water Department Memorandum June 8, 1977.

2. Hoyt, Brian P. and Chapman, James D. "Corrosion Characteristics of Seattle Water and Evaluation of Treatment by Lime"; Seattle Water Department, Quality Control Division, Nov. 1972, Revised May 1975.

3. Nakhjiri, K.S., Herrera, C.E., and Hilburn, R.D. "Counteractive Effects of Disinfection and Corrosion Control" Seattle Distribution System Corrosion Control Study, Volume V., A report to the Municipal Environmental Research Laboratory Cincinatti, Ohio 1982.

4. Larson, T.E. "Corrosion by Domestic Waters" Illinois State Water Survey, Bulletin 59, 1975.